“Heteroazoarenes as Smart Molecular Switches: From pH sensing to Light-Controlled Wnt Agonism”

(スマート分子スイッチとしてのヘテロアゾアレーン：　pH センシングから光応答性 Wnt 受容体活性化作用まで)

A Thesis

Submitted for the Degree of

Doctor of Life Science

By

Shifa Ahmad

Division of Transdisciplinary Life Science

Graduate School of Life Science

Hokkaido University

Japan, June 2025

Contents

General Introduction

A molecular switch is a system that undergoes reversible transitions between distinct states when subjected to specific external stimuli. These stimuli may include light, pH variation, redox change, thermal change, each inducing a structural or electronic transformation. Molecular switches serve as fundamental components in dynamic functional systems, contributing significantly to different fields such as nanotechnology, photopharmacology, supramolecular chemistry, and materials science.

One of the most extensively studied examples is azobenzene, a photoswitch molecular switch that exhibits reversible cis-trans isomerization upon exposure to ultraviolet (UV) and visible light. The photoisomerization occurs by the selective excitation of π–π* and n–π* electronic transitions, leading to rapid and controllable shifts between the planar *trans* form and the bent *cis* form. This transformation enables applications such as photo responsive drugs. Azobenzene dyes are also extensively investigated for the development of colorimetric pH indicators and some of them are commercially available for practical applications. Apart from azobenzene, many molecular switches such as diarylethenes, spiropyrans offer distinct switching modalities tailored to specific operational environments. The integration of molecular switches into biological, medicinal, and material science frameworks continues to drive innovation, enabling advances in precision therapeutics, adaptive materials, and molecular-level computing.

The defining characteristic of molecular switches lies in their ability to undergo repeated, controlled transitions without structural degradation, ensuring sustained functionality over multiple switching cycles. These transitions occur between energetically stable or metastable states, allowing for predictable and efficient modulation of molecular properties. Such properties include alterations in absorbance spectra, fluorescence intensity, charge distribution,

conductivity, conformation, and mechanical responsiveness, making them highly relevant for applications in controlled drug delivery, biosensing, signal transduction, and molecular electronics.

Molecular switches are of many types such as pH sensitive molecular switches, photo responsive molecular switches, thermo responsive molecular switches etc.

pH sensitive Molecular switches

pH sensitive molecular switches are compounds that change color in response to variations in pH levels. This phenomenon, known as acidochromism, occurs due to change in electronic configuration in the molecules when they interact with protons. These switches are frequently used as pH indicators, with examples including phenolphthalein, methyl orange, Alizarin Yellow R and methyl red.[2-7] Azobenzene dyes are extensively investigated for the development of colorimetric pH indicators and some of them are commercially available for practical applications like methyl orange, which shows red color at lower pH and yellow color at higher pH. Its pK_a is 3.47 in water at 25 °C.

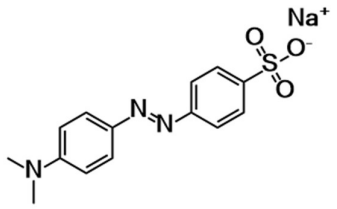

Figure 1. Methyl orange pH indicator

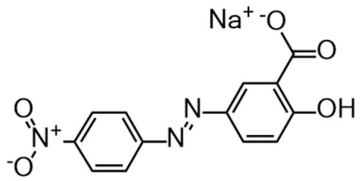

Figure 2. Alizarin Yellow R pH indicator

Photoswitch molecules

Photoswitches undergoes reversible interconversion between two forms upon light irradiation. The two forms differ in their structure, absorption spectra and several other properties. Photoexcitation causes the conversion of the molecule from a stable isomer to a high energy isomer which can revert back to the stable conformation by overcoming an activation barrier. The difference in the properties of the two isomeric forms can be exploited to design smart systems for many applications.

Molecular photoswitches are compounds that can change their structure and properties upon absorbing a photon of light. This change is reversible, allowing the compound to switch back and forth between two states. In the field of photopharmacology, molecular photoswitches are incorporated into the biologically active small molecules to control their activity in a specific location and time. They show reversible structural change between two forms when exposed to light, affecting their effectiveness against biological targets. Although many different types of photoswitches are known, the most common types of photoswitches used for photopharmacology are those based on azobenzenes and dithienylethenes.[8,9,10]

One notable example is azobenzenes, which undergo a significant geometric change when exposed to light, transforming from the trans-isomer to the cis-isomer. The cis-isomer can isomerize to the trans-isomer either by exposure to light of a different wavelength or through thermal isomerization. Typically, the trans-isomer is more thermodynamically stable.

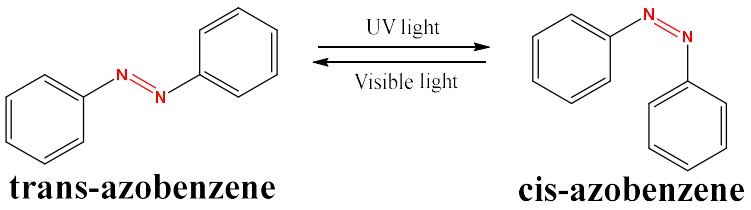

Figure 3. Photoisomerization of azobenzene molecular photoswitch.

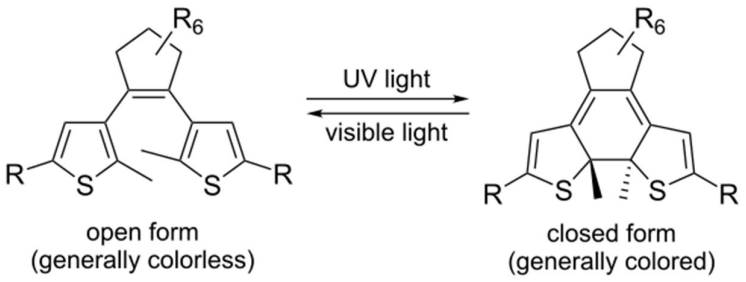

Figure 4. Photoisomerization of dithienylethenes molecular photoswitch.

Using light to control these photoswitches is advantageous because it does not introduce any contaminants or cause toxicity. Light also enables precise control over the activation of photoswitches, which is crucial for applications in biological systems. The behaviour of these compounds can be finely tuned by adjusting the wavelength and intensity of the light used. Molecular photoswitches, such as azobenzenes, provide a powerful tool for controlling biological processes with high spatial and temporal precision, making them valuable in fields like photopharmacology.

Thermoresponsive molecular switches

In thermal molecular switches, conformational or structural change is induced by the temperature.[11] Some molecules show reversible color change when they are heated or cooled respectively. Examples of thermochromic organic molecules include crowded ethenes, spiro compounds and Schiff bases.

Schiff bases are fascinating compounds that exhibit thermochromism, they change color with temperature variations. This property is often due to structural changes in the molecule, such as hydrogen-atom tautomerism between enol and keto forms. These changes can alter the electronic structure, leading to visible color shifts

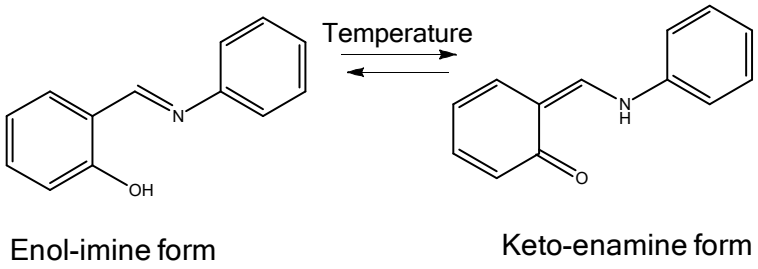

Figure 5. Schiff Base, a thermochromic molecule

Designing new molecular switches are still very demanding in the context of unexplored applications. For instance, well-studied azobenzene molecular switch that can respond to both photon and acid/base stimuli depending on the molecular design, however required harmful UV light and hence is not suitable for many applications as in the case of photopharmacology applications. Heteroazoarenes are novel category of molecular switches that has heteroarene segment either one or both sides of azo bond. They are either based on six-membered heteroarene (pyridine, piperidine, pyrimidine etc) or five-membered heteroarenes (thiazole, pyrazole etc). My PhD research focused on the development of novel heteroazoarenes as smart molecular switches for near-neutral pH sensing application and light-controlled activation of Wnt signaling pathway.

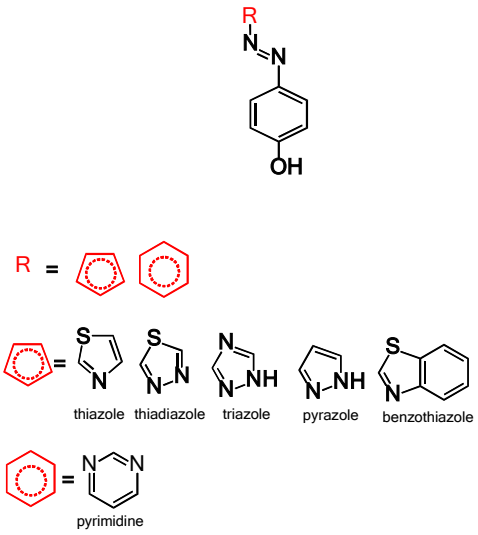

Figure 6. Heteroazoarenes molecular switches having different heterocycles.

References

1. Feringa, B. L., & Browne, W. R. (Eds.). (2011). *Molecular switches*. John Wiley & Sons.
2. A. Pastore, D. Badocco, S. Bogialli, L. Cappellin, P. Pastore*, Microchem. J.,* 2021, 160, 105605.
3. M. A. Cardona, D. Makuc, K. Szaciłowski, J. Plavec, D. C. Magri, *ACS Omega*, 2017, 2, 6159.
4. W. Lv, C. Wang, L. Ji, T. Deng, S. Yang, T. Zhu, S. Liu, Q. Zhao*, J. Mater. Chem. C,* 2024, 12, 8777.
5. B. Shan, Y. Deng, B. Tang, R. Lu, S. Zhang, *Chem. Lett.,* 2016, 45, 472.
6. M. A. Cardona, D. C. Magri, *Tetrahedron Lett.*, 2014, 55, 4559.
7. F. L. Coelho, C. de Ávila Braga, G. M. Zanotto, E. S. Gil, L. F. Campo, P. F. B. Gonçalves, F. S. Rodembusch, F. da S. Santos, Sens. Actuators B 2018, 259, 514.
8. I. M. Welleman, M. W. H. Hoorens, B. L. Feringa, H. H. Boersma and W. Szymański, *Chem. Sci.*, 2020, 11, 11672–11691.
9. Q. Xu, C. Zhang, Z. Xu, L. Wang, Z. Liu, Z. Li, X. Shao. *J. Agric. Food Chem.* 2023, **71**, 11048–11055.
10. Z. Li, Y. Wang, M. Li, H. Zhang, H. Guo, H. Ya, J. Yin. *Org. Biomol. Chem.*, 2018, 16, 6988-6997.
11. M. P. O'Hagan, J. Ramos-Soriano S. Haldar, S. Sheikh, J. C. Morales, A. J. Mulholland, M. C. Galan. *Chem. Commun.*, 2020, 56, 5186-5189.
12. Day, J. H. (1968). Thermochromism of inorganic compounds. *Chemical Reviews*, *68*(6), 649-657.

Chapter 1

Studies of Azoheteroarene Dyes for Near-neutral pH Sensing Application

Introduction

pH monitoring is essential in many fields, including chemical and biological processes, clinical diagnostics, biomedical engineering, and environmental science.[1,2] Considerable research efforts have been focused on measuring the pH and many approaches have been investigated including fluorescent probes and visible ratiometric detection methods[1-6] For instance, allylcalcein is a fluorescent pH sensor that exhibits a noticeable decrease in fluorescence intensity with increasing pH. It demonstrates good reproducibility, stability, and response time.[3] Ratiometric method is also utilized to develop fluorescent-based pH sensor where the pH is measured by comparing the fluorescence intensities of the two dyes. For instance, core/shell zeolite nanoparticles where the core is made of a zeolite-β matrix containing a 3-hydroxyflavone reference dye, while the shell is composed of silica embedded with a pH-sensitive dye.[2]

Another category of pH indicator is based on colorimetry, which has attracted much attention because of the ease of detection by naked eye without any instruments and its cost-effectiveness. Azobenzene dyes are extensively investigated for the development of colorimetric pH indicators and some of them are commercially available for practical applications (Figure 1a).[9-14] However, most of the azobenzene dyes show pH detection either in strong acid or alkaline conditions. For instance, pK_a of commercial methyl yellow is 3.3 which is quite acidic while that of alizarin yellow is 11 which lies in basic range. Colorimetric pH indicators that can show distinct color changes in near neutral pH range are highly advantageous for the detection of pH variation in biological systems. For instance, tissue and cell culture is a common experiment in many biology laboratories. When tissues or cells are incubated for several days, the waste products from dying cells can alter the pH of the culture medium. This change can be detected by monitoring the color shift of an indicator. One such indicator is phenol red (pk_a 7.9, see Figure 1b), which is a non-azo dye. While phenol red is generally considered inert for

biological environment, it is reported to cause side effects in certain culture media.[15] Hence the development of near neutral pH indicators are important for the possible applications in cell biology.

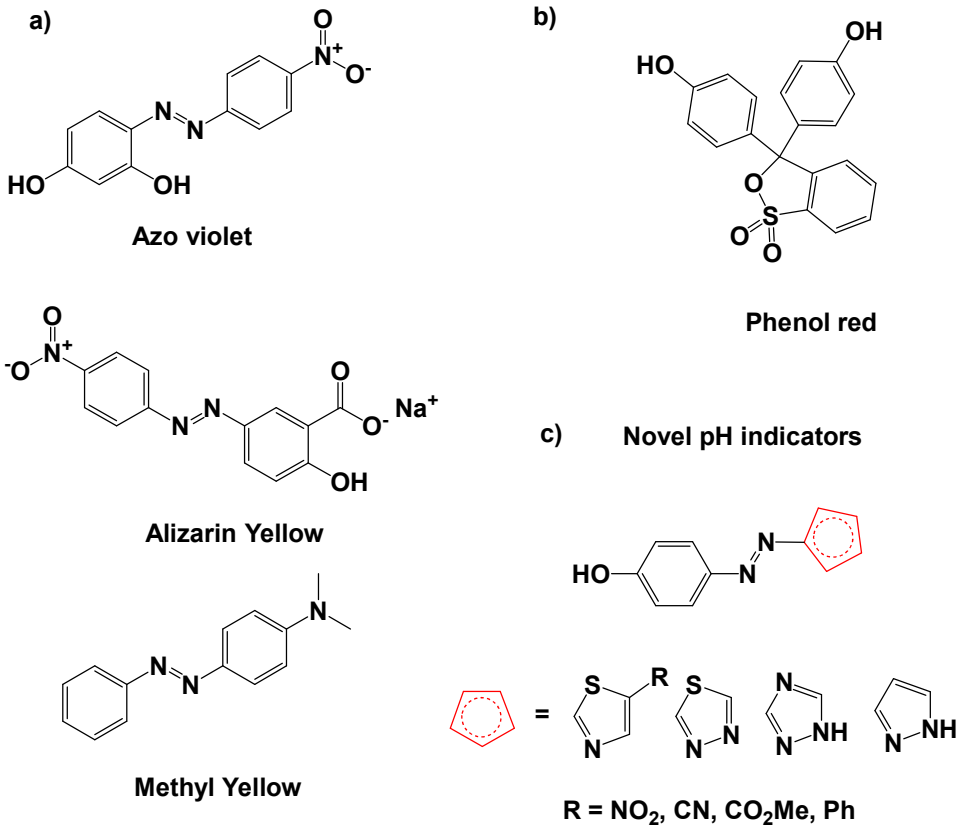

Figure 1. Molecular structures of known and novel pH indicators.

The purpose of this study is to investigate a new series of near neutral pH indicators based on heteroazoarenes dyes. The dyes incorporate various heteroaryl groups, including thiazole, thiadiazole, triazole, pyrazole, and benzothiazole, which are linked to a hydroxyphenyl azo group. Heteroazoarenes with five-membered heteroaryl motifs have gained significant attention as a new category of photoswitches due to their unique photophysical properties.[16-23] However, such motifs are not studied yet as pH indicator. In my Ph.D. study, I investigated heteroazoarenes with five-membered heteroaryl motifs as a new category of pH indicators,

which detects pH variation in aqueous solutions in near-neutral range. As the pH changes, these dyes undergo noticeable color transitions within a narrow pH range, allowing for easy visual detection by naked eye without the need for specialized equipment. I found that the heteroazoarenes dyes can also precisely monitor the pH even in complex environment such as cell culture medium. In this study I have also shown that these heteroazoarenes dyes can be used for detecting pH changes in the culture medium of growing cancer cells, which highlights their future potential for distinguishing cancerous tissues from normal tissues based on their distinct pH environments.

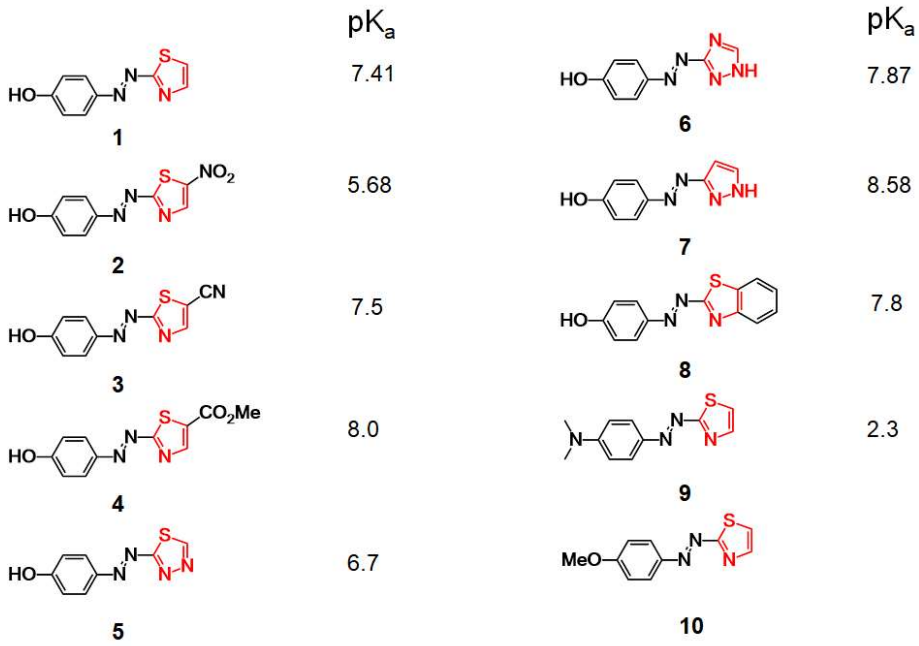

Figure 2. Molecular structures of heteroazoarenes **1-10** containing thiazole, benzothiazole, thiadiazole, pyrazole, and triazole moieties along with their pKa.

Experimental Section

Chemicals and Instruments

All reagents, solvents and culture medium were purchased from commercial sources (FUJIFILM Wako Pure Chemical Corporation, Tokyo Chemical Industry, Merck, Kanto Chemical) and used without further purification. Reactions were monitored by thin-layer

chromatography using TLC silica gel 60 F_{254} (Merck). Column chromatography was performed using silica gel 60 N (spherical, neutral, 63-210 μm, Kanto chemical). NMR spectra (^{1}H, ^{13}C) were measured by a JEOL ECX-400 (400 MHz) spectrometer. A Shimadzu UV spectrophotometer (UV-1800) equipped with a TCC-100 Shimadzu temperature-controlled cell holder was used for UV-vis spectrophotometry.

Method for pH determination

A stock solution of compounds in DMSO (5–10 mM) was diluted in either water or a 0.1 M HEPES buffer (3 mL). The pH was adjusted to a range of 8.0 to 12.0 using a 0.1 M NaOH solution. The solution was then titrated with the minimum volume of 1 M HCl (1–5 μL, added in increments), and the absorbance was measured after each addition of HCl. I used a portable pH meter (LAQUAtwin, HORIBA) to continuously monitor the pH changes throughout the experiments.

Computational calculations

Theoretical calculations were performed using Gaussian 09 (Revision D.01).[24] GaussView 6.0 was used to draw and visualize the molecular structures and to feed the inputs.[25] Density functional theory (DFT) and time dependent density functional theory (TDDFT) were employed to optimize the geometries and to obtain the electronic transition in the ground state, respectively.[25–29] The 6-31+G(d,p) basis set with Becke's three-parameter hybrid exchange and the Lee-Yang-Parr's correlation functional (B3LYP) was used for geometry optimization.[30] The solvent stabilization of different isomers was incorporated by considering integral equation formalism-polarizable continuum model (IEF-PCM) and choosing aqueous medium.

pK_a of a molecule was calculated using the following equations (Eq. S1-S4) considering a deprotonation reaction, $AH \leftrightharpoons A^- + H^+$.[1–3] Thermally corrected Gibb's free energies were calculated for the neutral and anionic species in the presence of an explicit water molecule at the electron-donating group using the same level of computational method at 298.15 K.[1–3] The

free energy of the aqueous phase proton is calculated with Eq. S3.[1,2] The pK$_a$ calculated with and without explicit water are shown in Table S1.

$$pK_a = \frac{\Delta G^*_{aq}}{2.303RT} \quad \text{(Eq. S1)}$$

$$\Delta G^*_{aq} = G^*_{aq}(A^-) + G^*_{aq}(H^+) - G^*_{aq}(AH) \quad \text{(Eq. S2)}$$

$$G^*_{aq}(H^+) = G^0_g(H^+) + \Delta G_{aq,solv}(H^+) - \Delta G^{1atm \rightarrow 1M} \quad \text{(Eq. S3)}$$

$$G^0_g = H^0_g - TS^0_g \quad \text{(Eq. S4)}$$

$\Delta G_{aq,sol}(H^+)$ = -265.9 kcal/mol, H^0_g = 1.48 kcal/mol, S^0_g = 26.05 cal/(mol-K), $\Delta G_{1\ atm \rightarrow 1M}$ = 1.89 kcal/mol

Biological studies

Calculation of pKa in IMDM buffer: A DMSO stock solution of compound **1** was diluted in commercial IMDM (pH 7–7.4) and adjusted the pH upto 8.3 by NaOH solution. For titration experiment, a dilute HCl added portion wise and measured absorbance. Non-linear fitting of the pH dependent absorbance changes gave pKa.

Stability in glutathione containing solution: A DMSO stock solution of compound **1-8** was diluted in aqueous solutions containing glutathione (1 mM) and measured absorbance at λ_{max} nm every 1 or 2 hours for 12 or 24 h.

Cell culture: HeLa cells (5.0×10^4 cells/well) plated onto a 96-well plate with lid were supplied with Dulbecco's minimum essential medium (DMEM, 100 μL) containing 10% fetal bovine serum (FBS). After incubation at 37 °C under 5% CO_2 for 24 h in DMEM containing 10% FBS, the cells were rinsed with Dulbecco's phosphate buffer saline (D-PBS, 200 μL) and supplied with a fresh DMEM containing varying amount of compound **1** followed by the incubation at 37 °C in the presence or absence of 5% CO_2.

Cytotoxicity assay: HeLa cells (5.0×10^3 cells/well) plated onto a 96-well plate with lid were supplied with Dulbecco's minimum essential medium (DMEM, 100 μL) containing 10% fetal bovine serum (FBS). After incubation at 37 °C under 5% CO_2 for 24 h in DMEM containing 10% FBS, the cells were rinsed with Dulbecco's phosphate buffer saline (D-PBS, 200 μL) and supplied with a fresh DMEM containing varying amount of compound **1** followed by the incubation for 48 hours. Then, CCK-8 solution (10 μL) was added to each well, incubated at 37 °C under 5% CO_2 for 3 h followed by the measurement of absorbance at 450 nm.

Results and Discussions

Synthesis of azoheteroarenes

Compounds **2, 3 and 4** were synthesized according to our previously reported procedure [*J. Am. Chem. Soc.* 2023, 145, 9072]. 2-Aminothiazole derivatives (5.4 g, 54 mmol) was dissolved in a solution of deionized water (48 mL) and concentrated HCl (36%, 16 mL). A mixed solution of sodium nitrite (3.9 g, 58 mmol, 1.07 eq.), phenol (5.1 g, 54 mmol, 1.0 eq.), sodium hydroxide (4.5 g, 0.11 mol, 2.0 eq.) and deionized water was added dropwise to the above acidic solution at 0 °C and stirred for 2 h. The precipitate formed was filtered, and the crude product obtained was purified by column chromatography on silica using EtOAc (50%) /hexane eluent to isolate the desired compounds.

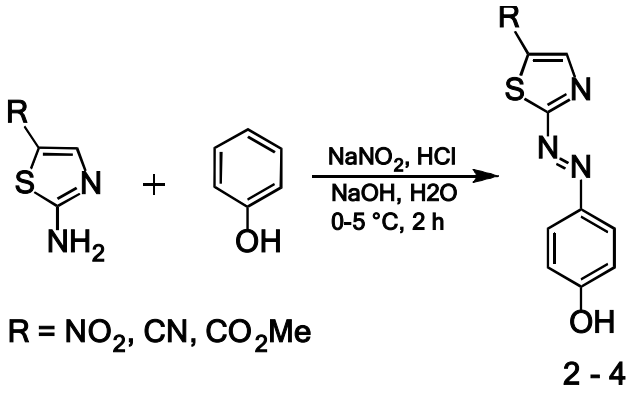

Scheme 1: Synthetic scheme for pH Indicators **2, 3 and 4**.

Synthesis of compounds 5, 6, 7 and 8

2-Amino derivatives (5.4 g, 54 mmol) were dissolved in a solution of deionized water (48 mL) and concentrated HCl (36%, 16 mL). A mixed solution of sodium nitrite (3.9 g, 58 mmol), phenol (5.1 g, 54 mmol), sodium hydroxide (4.5 g, 0.11 mol) and deionized water was added dropwise to the above acidic solution at 0 °C and stirred for 2 h. The precipitate formed was filtered, and the crude product obtained was purified by column chromatography on silica using EtOAc (50%) /hexane eluent to isolate the desired compound.

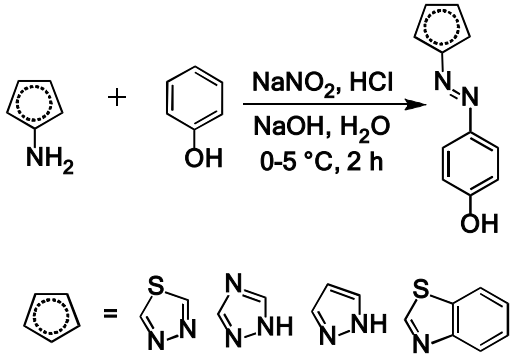

Scheme 2: Synthetic scheme for pH indicators **5, 6, 7 and 8**

NMR spectra of compound 2–8.

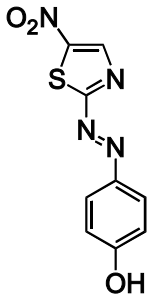

Compound 2 (Yield 54%)

^{1}H NMR (400 MHz, DMSO-d_6) δ 8.99 (s, 1H), 7.99–7.97 (d, 2H), 7.06–7.03 (d, 2H).

^{13}C NMR (600 MHz, DMSO-d_6) δ 179.39, 166.29, 148.54, 145.18, 144.87, 128.88, 117.76.

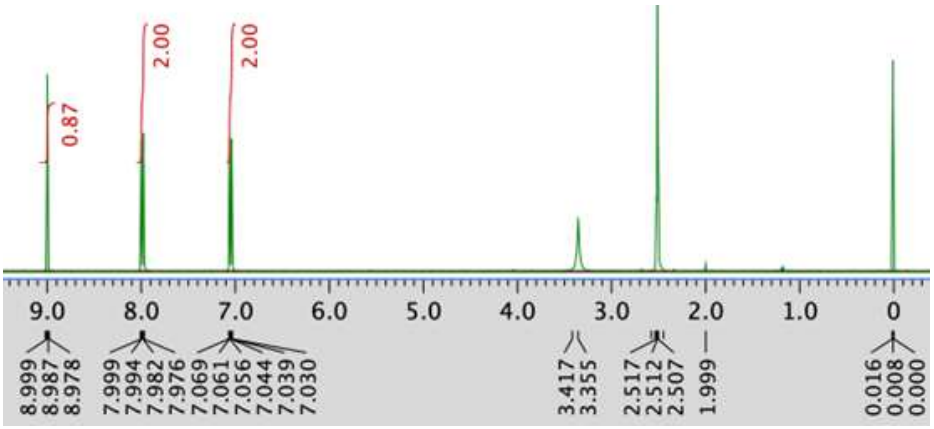

Figure 3: ^{1}H NMR of compound 2 in DMSO-d_6 at 25 °C. Peaks at δ 3.35 (H_2O) is from solvent.

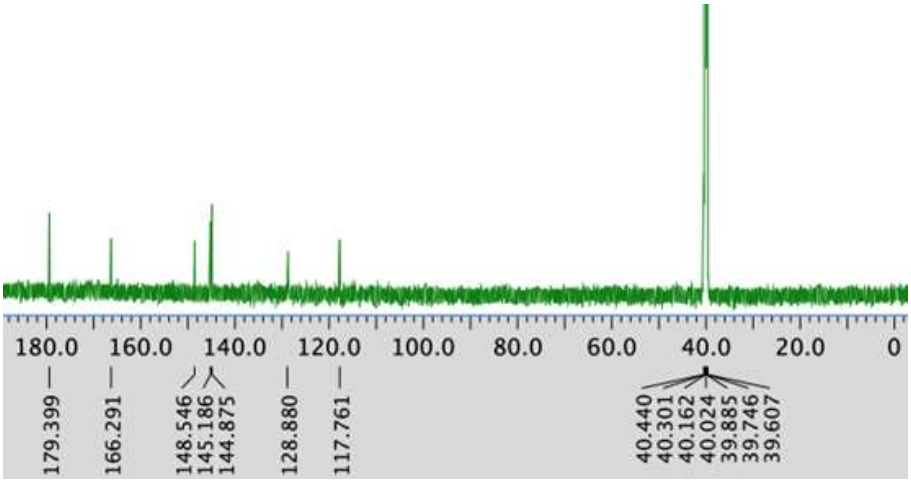

Figure 4: ^{13}C NMR of compound 2 in DMSO-d_6 at 25 °C.

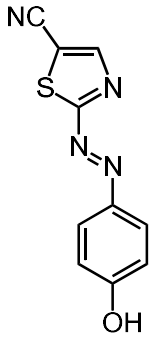

Compound 3 (Yield 2%)

^{1}H NMR (400 MHz, CD_3OD) δ 8.49 (s, 1H), 7.79–7.77 (dd, 1H), 7.47 (td, 1H), 7.01–6.93 (m, 2H).

^{13}C NMR (600 MHz, DMSO-d_6) δ 146.29, 138.10, 130.76, 128.57, 128.12, 126.02. 60.28

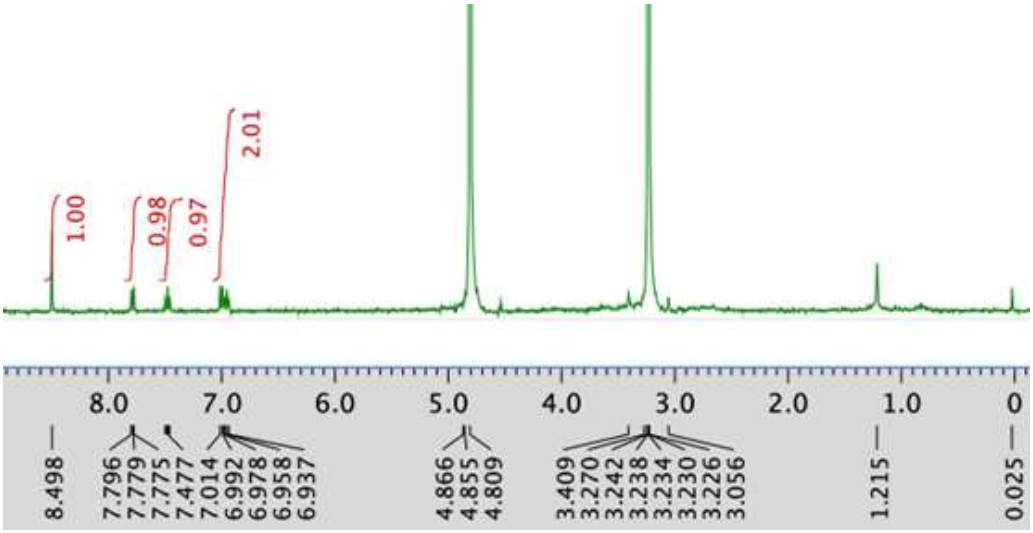

Figure 5: ^{1}H NMR of compound 3 in CD_3OD at 25 °C. Peaks at δ 4.89 (H_2O) is from solvent.

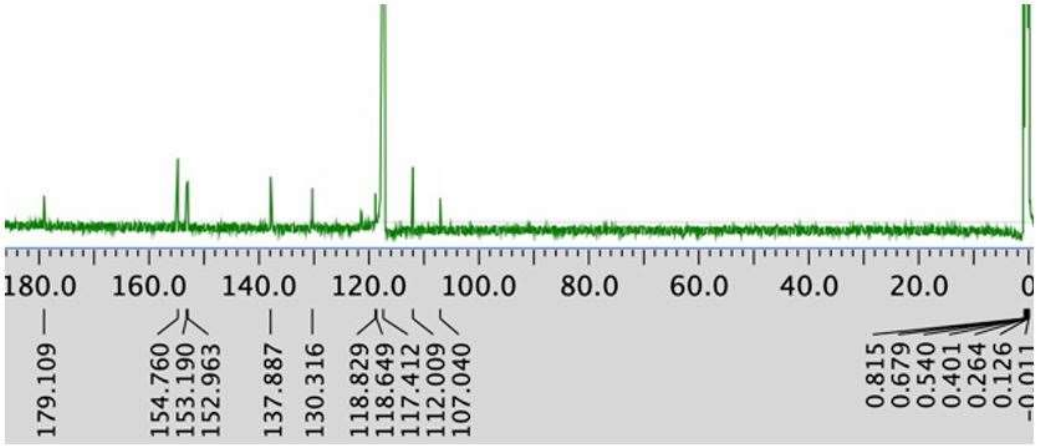

Figure 6: ^{13}C NMR of compound 3 in CD_3CN at 25 °C. Peaks at δ 117.412 and δ 0.815 are from CD_3CN solvent.

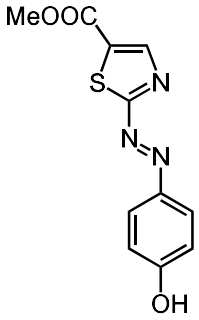

Compound 4 (Yield 2%)

^{1}H NMR (400 MHz, CD_3OD) 8.55 (s, 1H), 7.88 (d, 1H), 7.55 (m, 1H), 7.10–7.06 (m, 2H), 3.95 (s, 3H).

^{13}C NMR (600 MHz, DMSO-d_6) δ 180.17, 161.82, 158.67, 148.96, 139.54, 137.67, 129.42, 118.43, 60.28, 53.42.

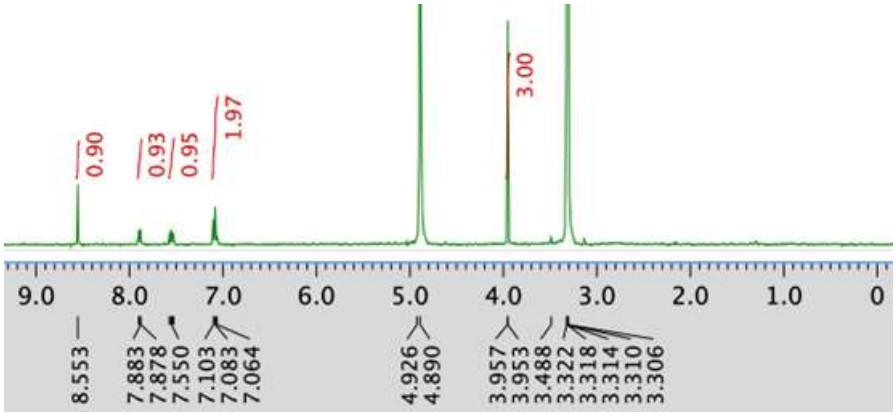

Figure 7: ^{1}H NMR of compound 4 in CD_3OD at 25 °C. Peaks at δ 4.89 (H_2O) is from solvent.

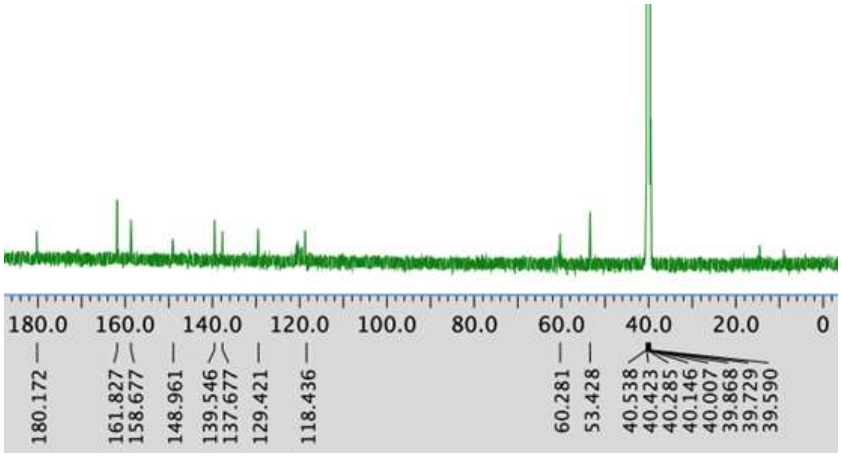

Figure 8: ^{13}C NMR of compound 4 in DMSO-d_6 at 25 °C.

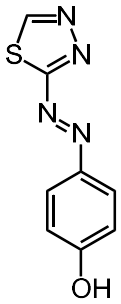

Compound 5 (Yield 6.8%)

^{1}H NMR (400 MHz, CD_3CN) δ 9.23 (s, 1H), 7.97–7.95 (d, 2H), 7.06–7.02 (d, 2H).

^{13}C NMR (600 MHz, DMSO-d_6) δ 180.45, 164.98, 154.77, 144.88, 127.55, 117.03.

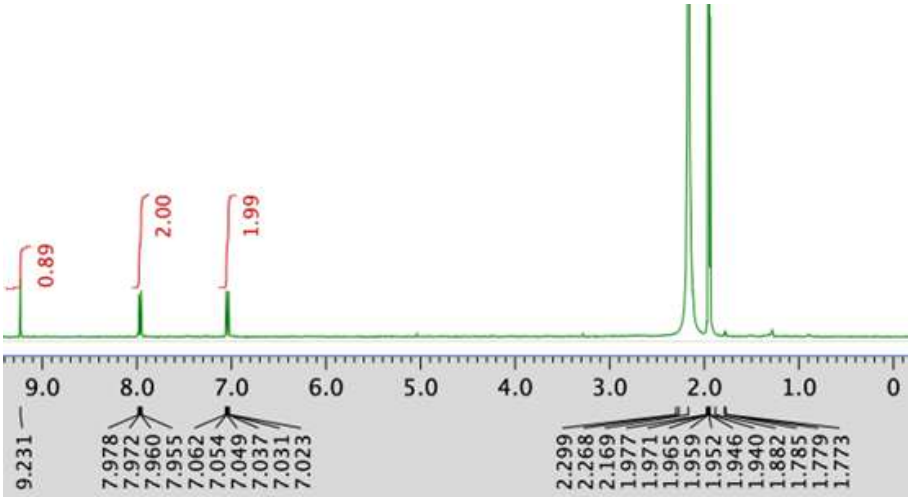

Figure 9: ^{1}H NMR of compound 5 in CD_3CN at 25 °C. Peaks at δ 2.13 (H_2O) is from solvent.

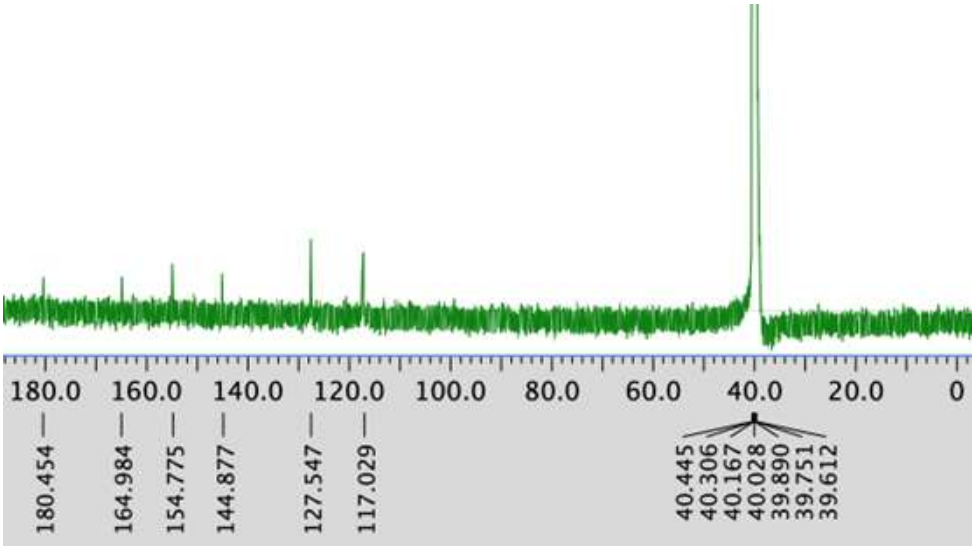

Figure 10: ^{13}C NMR of compound 5 in DMSO-d_6 at 25 °C.

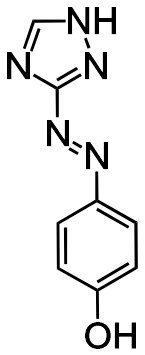

Compound 6 (Yield 79%)

^{1}H NMR (400 MHz, DMSO-d_6) δ 10.59 (s, 1H), 8.68 (s, 1H), 7.85–7.73(d, 2H), 7.03–6.95 (d, 2H).

^{13}C NMR (400 MHz, DMSO-d_6) δ 164.36, 161.13, 145.87, 130.86, 124.98, 116.42, 93.59.

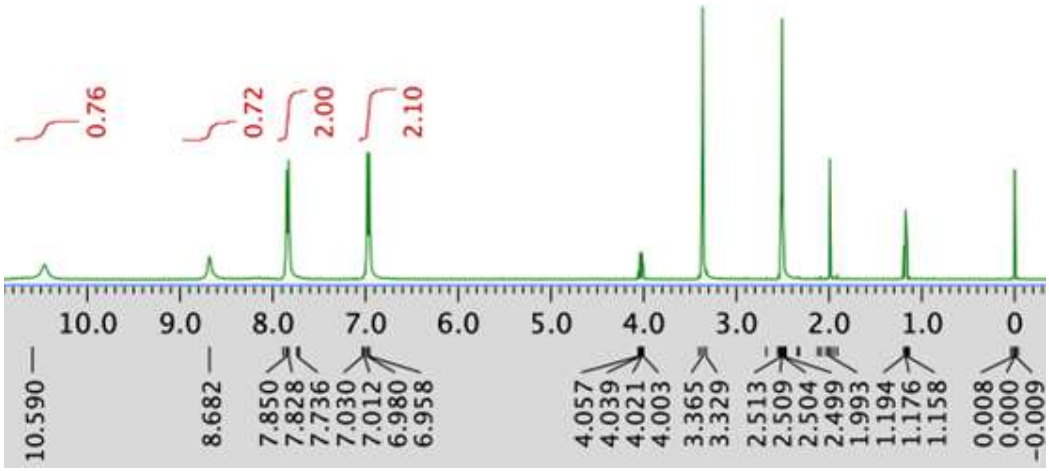

Figure 11: ^{1}H NMR of compound 6 in DMSO-d_6 at 25 °C. Peaks at δ 3.36 (H_2O), 4.05, 1.9 and 1.17 (ethyl acetate) are from solvents.

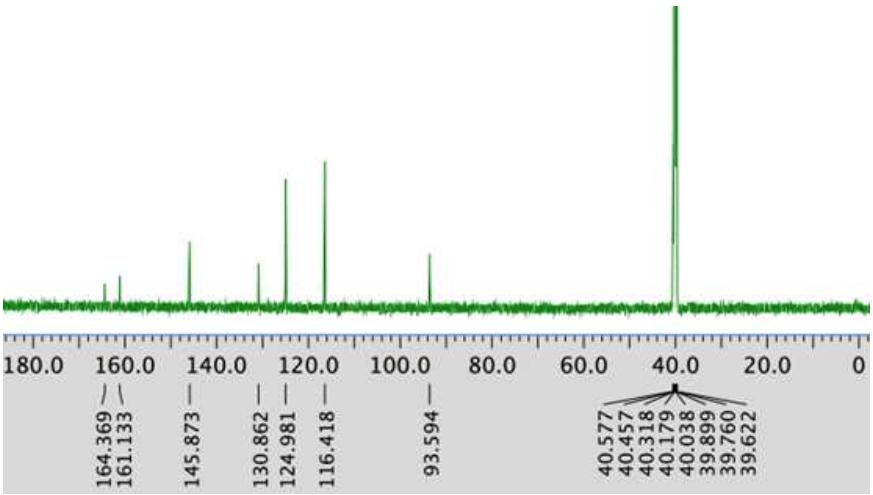

Figure 12: ^{13}C NMR of compound 6 in DMSO-d_6 at 25 °C.

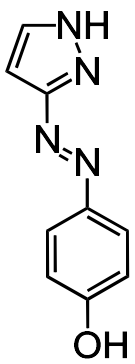

Compound **7** (Yield 21%)
^{1}H NMR (400 MHz, CD_3OD) δ 7.83–7.80 (d, 2H), 7.69 (s, 1H), 6.93–6.89 (d, 2H), 6.60 (s, 1H).

^{13}C NMR (400 MHz, DMSO-d_6) δ 169.62, 162.04, 145.99, 145.24, 125.73, 116.61.

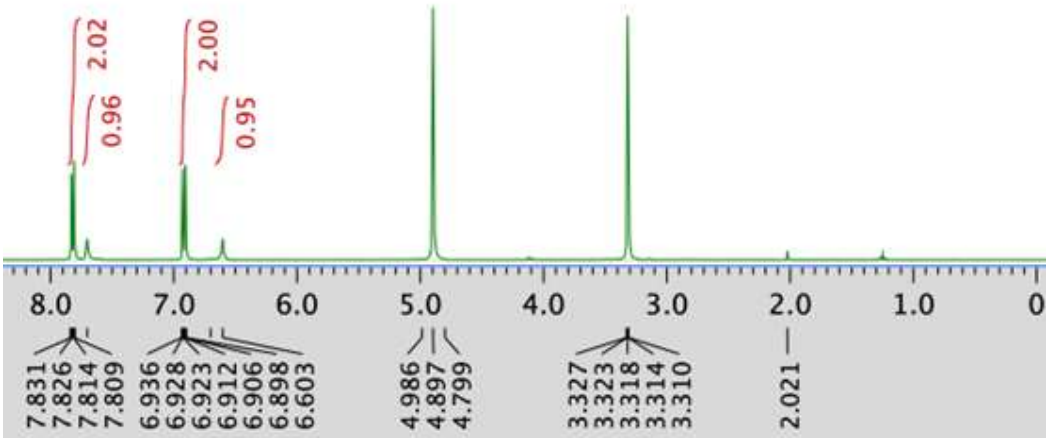

Figure 13: ^{1}H NMR of compound 7 in CD_3OD at 25 °C. Peaks at δ 4.89 (H_2O) is from solvent.

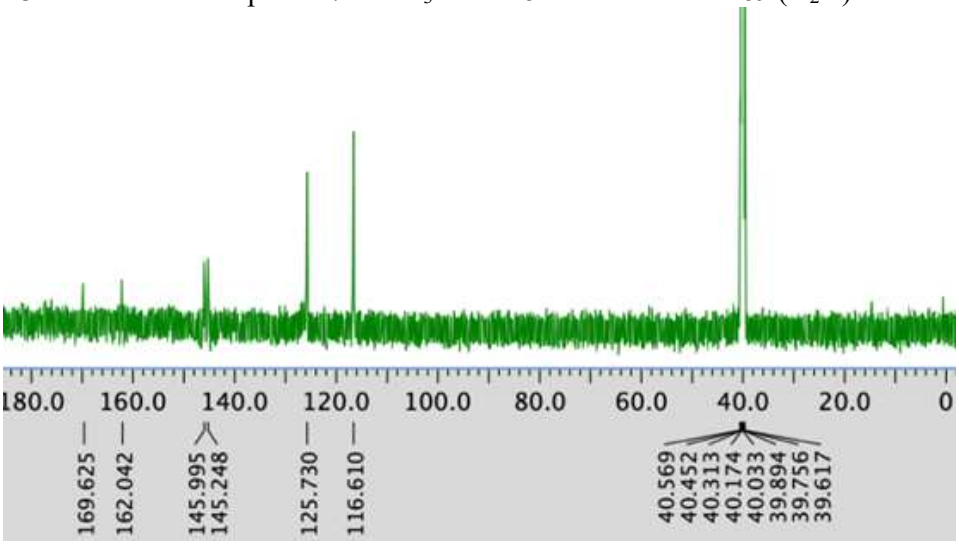

Figure 14: ^{13}C NMR of compound 7 in DMSO-d_6 at 25 °C.

Compound 8 (Yield 4%)

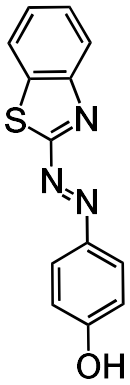

^{1}H NMR (400 MHz, DMSO-d_6) δ 8.09–7.94 (d, 2H), 7.95–7.93 (d, 2H), 7.58–7.53 (m, 2H), 7.03–7.00 (d, 2H).

^{13}C NMR (400 MHz, DMSO-d_6) δ.

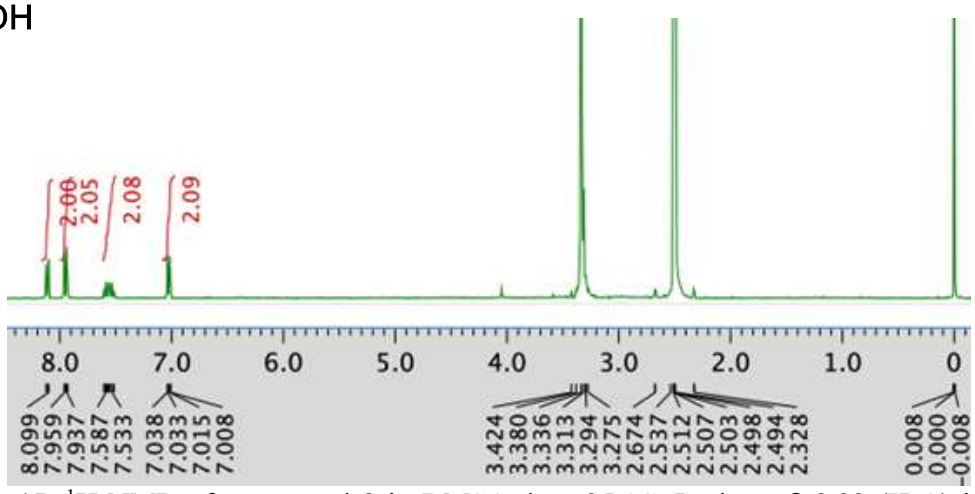

Figure 15: ^{1}H NMR of compound 8 in DMSO-d_6 at 25 °C. Peaks at δ 3.33 (H_2O) is from solvent.

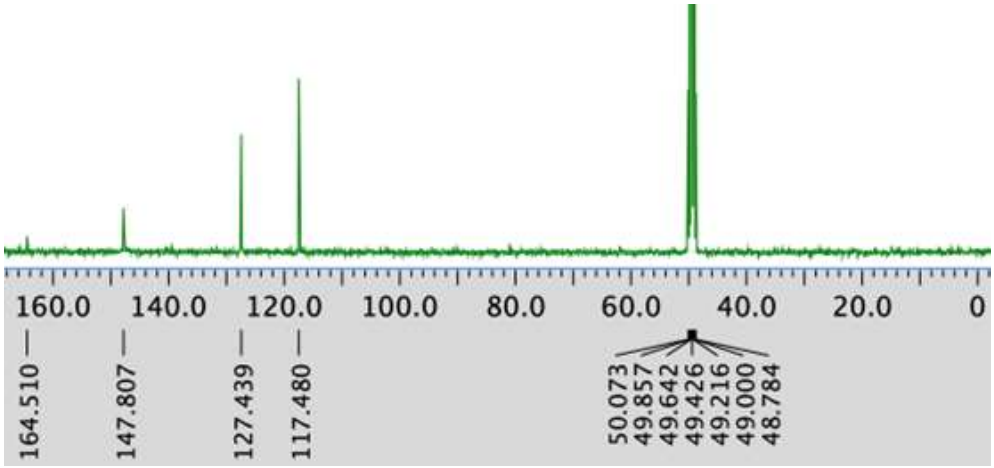

Figure 16: ^{13}C NMR of compound 8 in CD_3OD at 25 °C.

Compound 11 (Yield 56%)

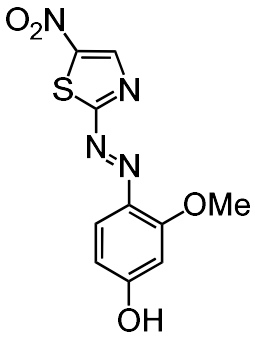

^{1}H NMR (400 MHz, DMSO-d_6) δ 8.92 (s, 1H), 7.78–7.76 (d, 1H), 6.66–6.63 (m, 2H), 3.90 (s, 3H).

^{13}C NMR (400 MHz, DMSO-d_6) δ 180.01, 168.84, 147.49, 143.97, 134.42, 56.32.

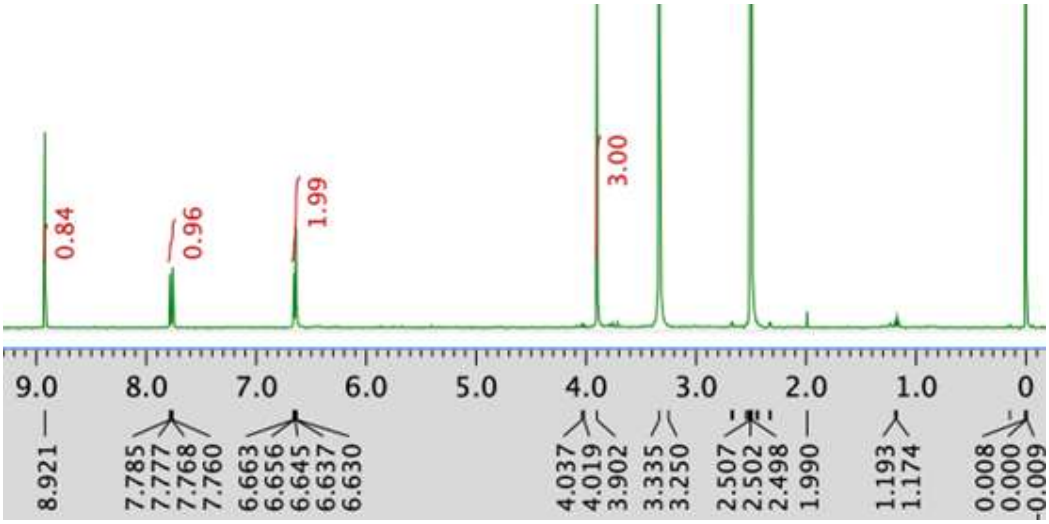

Figure 17: ^{1}H NMR of compound 11 in DMSO-d_6 at 25 °C. Peaks at δ 3.33 (H_2O) and minor peaks at δ 4.03, 1.99, 1.19 (ethyl acetate) are from solvents.

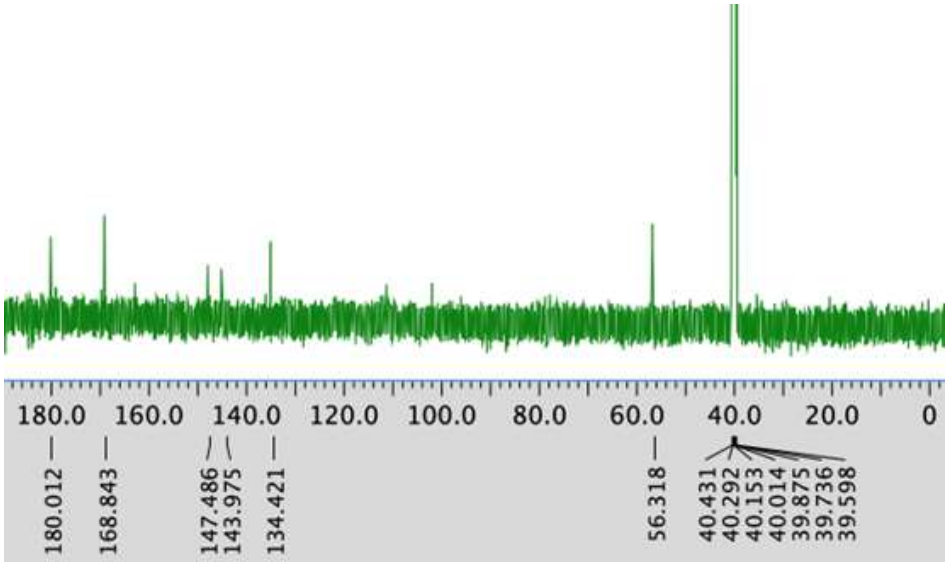

Figure 18: ^{13}C NMR of compound 11 in DMSO-d_6 at 25 °C.

Mass spectra of compounds

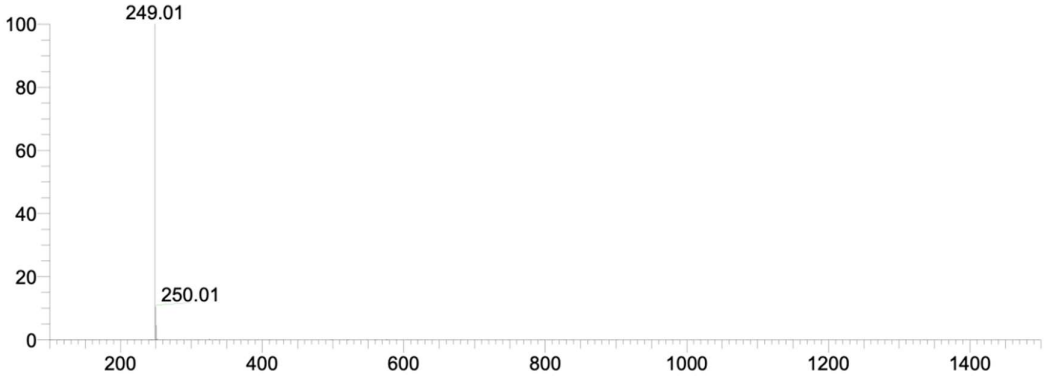

Figure 19: ESI MS spectrum of compound **2**. m/z [M H]$^-$ calcd for $C_9H_6N_4O_3S$: 249.02, found: 249.01.

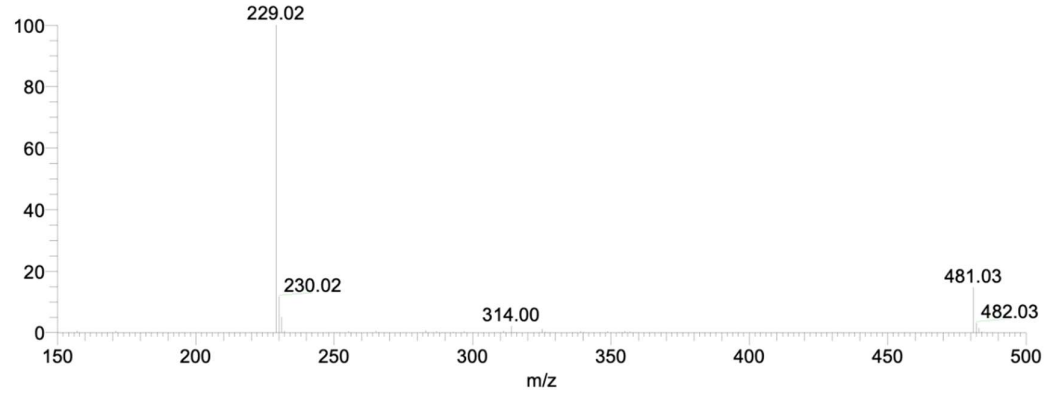

Figure 20: ESI MS spectrum of compound **3**. m/z [M H]$^-$ calcd for $C_{10}H_6N_4OS$: 229.03, found: 229.02.

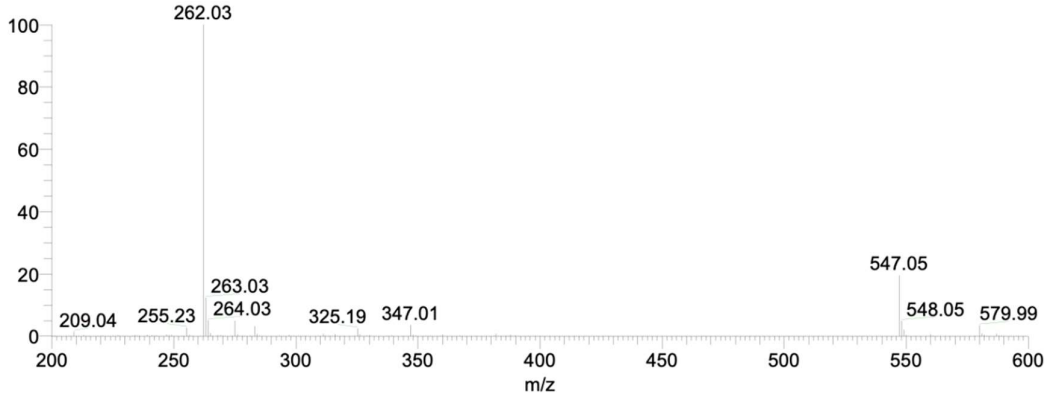

Figure 21: ESI MS spectrum of compound **4**. m/z [M H]$^-$ calcd for $C_{11}H_9N_3O_3S$: 262.04, found: 262.03.

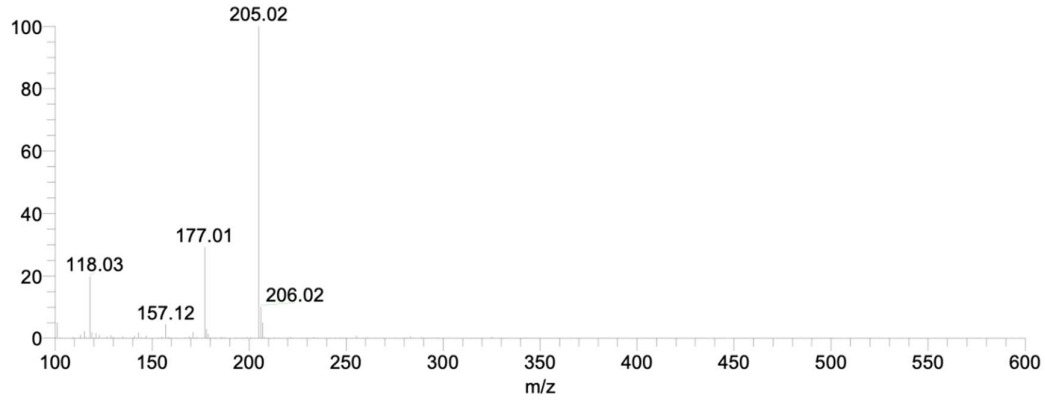

Figure 22: ESI MS spectrum of compound **5**. m/z [M H]$^-$ calcd for $C_8H_6N_4OS$ 205.03, found: 205.02.

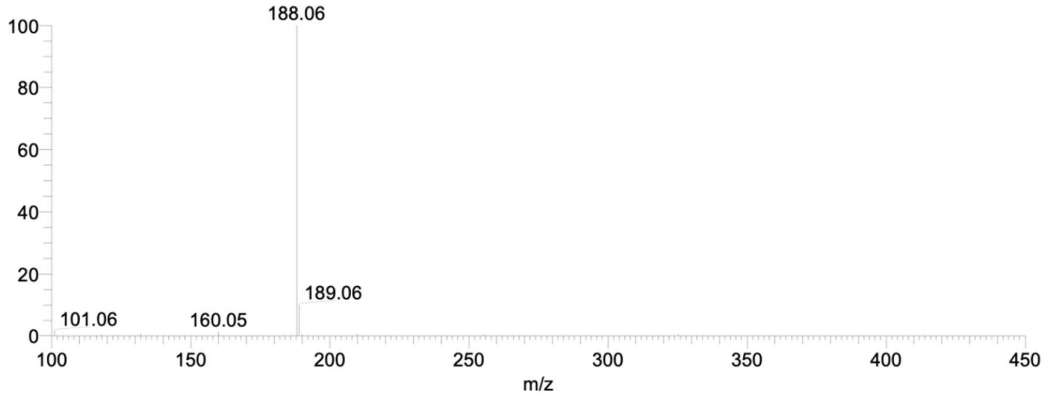

Figure 23: ESI MS spectrum of compound **6**. m/z [M H]$^-$ calcd for $C_8H_7N_5O$ 188.07, found: 188.06.

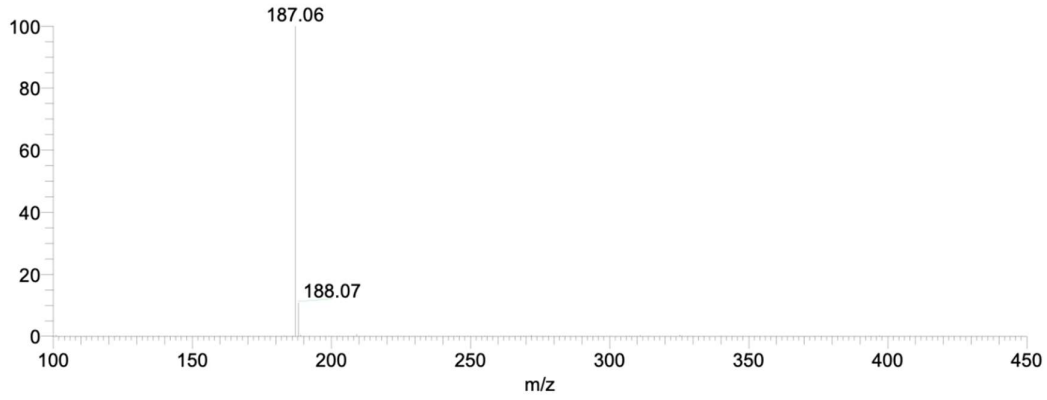

Figure 24: ESI MS spectrum of compound **7**. m/z [M H]$^-$ calcd for $C_9H_8N_4O$ 187.07, found: 187.06

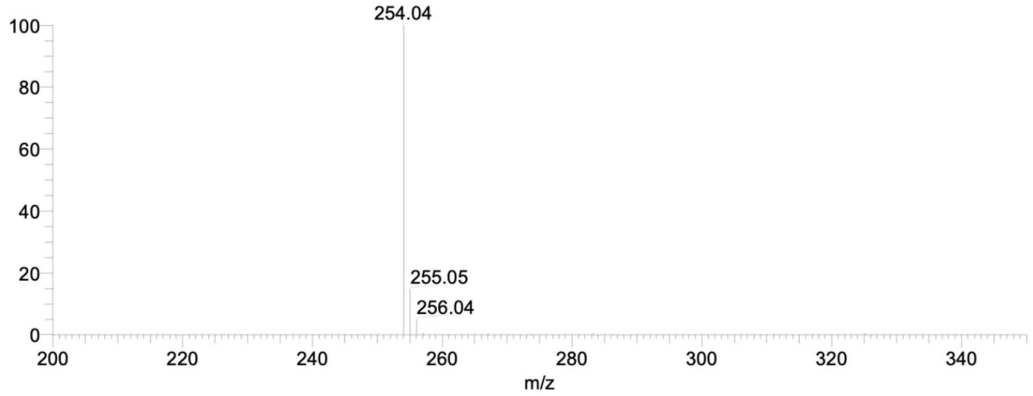

Figure 25: ESI MS spectrum of compound **8**. m/z $[M\ H]^-$ calcd for $C_{13}H_9N_3OS$: 254.05, found: 254.04.

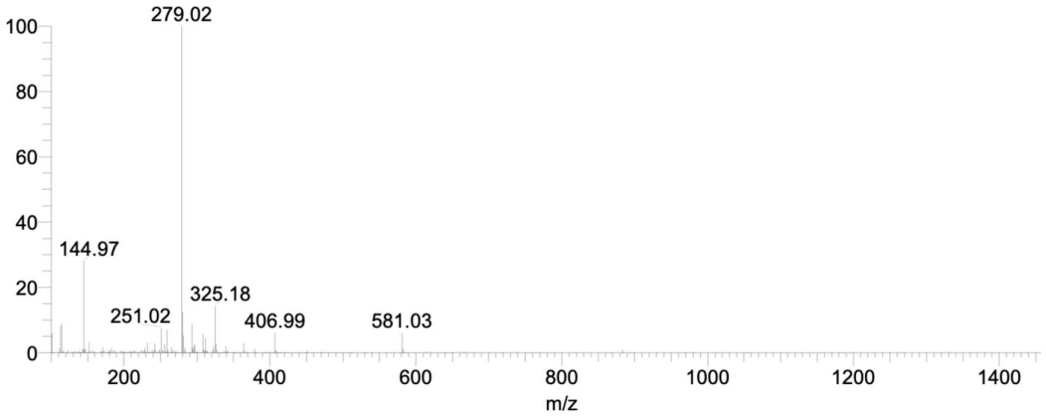

Figure 26: ESI MS spectrum of compound **11**. m/z $[M\ H]^-$ calcd for $C_{10}H_8N_4O_4S$: 279.03, found: 279.02.

Compounds **1**, **9** and **10** were reported in our previous article [*J. Am. Chem. Soc.* 2023, 145, 9072] and hence I have not mentioned the spectral data of them.

Absorption spectral studies

I recorded the absorption spectra of the synthesized compounds **1-10** in organic solvents (CH_3CN or DCM). The compound **1-10** exhibited absorption bands assignable to the $\pi \rightarrow \pi^*$ electronic transition (figure 27). Compound **1- 10** exhibited an absorption band (λ_{max} = 338–

490 nm). In aqueous solvents, the compounds exhibited a significantly red-shifted absorption bands depending on the solution pH (figure 28-38).

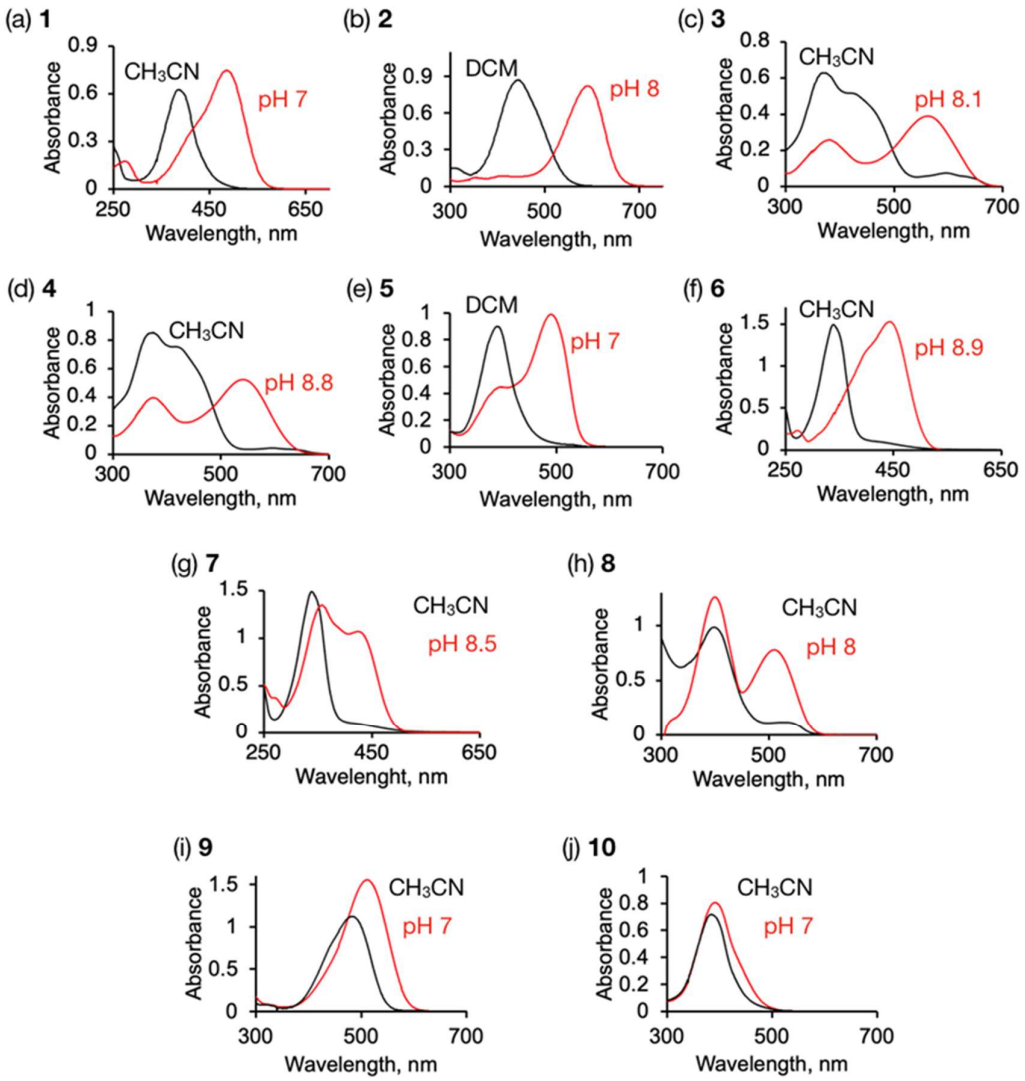

Figure 27: Absorption spectra of compounds **1–10** (a–j) in organic (black curves) and aqueous (red curves) solvents at 25 °C.

UV-vis titration studies

I studied the absorption spectral changes of compound **1-10** in different pH solutions. For compound **1**, 20 µM stock solution was prepared, and the initial pH of the aqueous solution was 10.4. The solution was titrated using a minimal volume of 1M HCl (1–5 µL, added portion-wise). After each addition of HCl, the absorbance was measured. I observed that the absorption

band at 487 nm gradually decreased, while a new absorption band at 391 nm emerged, becoming dominant at pH 7 (figure 28a). The isobestic point at 420 nm indicates the presence of two species in equilibrium as the pH of the solution changes.

The pKa is the pH value at which half of the molecules of a pH indicator are in the deprotonated form. By fitting experimental data from absorption spectra to a sigmoidal curve, the pKa value can be determined at the inflection point of that curve. The resulting sigmoidal curve typically has an S-shape, illustrating the gradual transition between the protonated and deprotonated forms. The pKa value for compound **1** was 7.4 which lies in the neutral range (figure 28b). The pH detection range was 6.1 (yellow) to 7.9 (red) as shown in figure 28c.

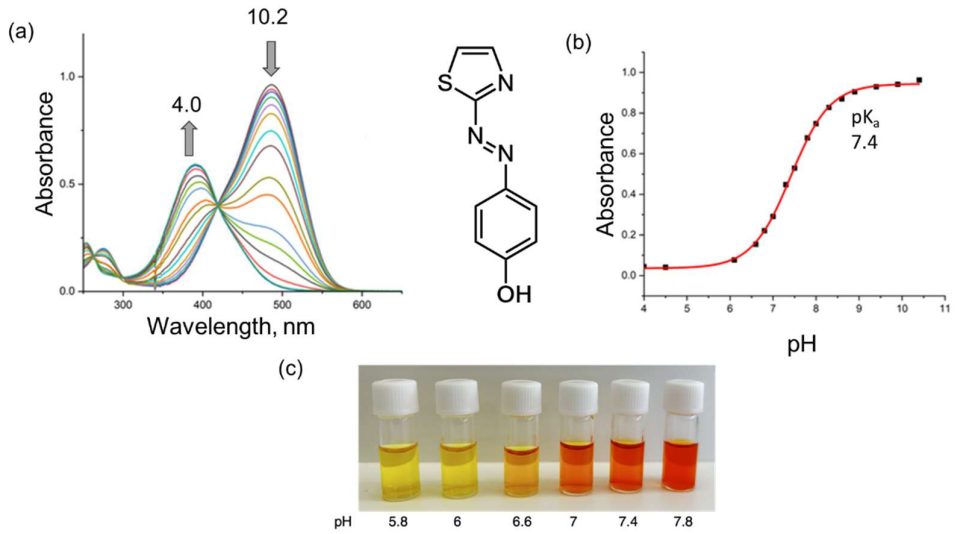

Figure 28. (a)Absorption spectra of compound **1** in aqueous solution in 0.1M HEPES buffer (pH adjusted with 0.1M NaOH) at 25 °C upon titration with 1M HCl between pH ranges mentioned in the graph. (b)Non-linear fitting of pH dependent absorbance changes at λ_{max} along with pK_a value. (c) Image showing pH dependent color changes.

For compound **2**, 20 µM stock solution was prepared, and the initial pH of the aqueous solution was 8. The solution was titrated using a minimal volume of 1M HCl (1–5 µL, added portion-wise). After each addition of HCl, the absorbance was measured. I observed that the absorption band at 590 nm gradually decreased, while a new absorption band at 435 nm emerged, becoming dominant at pH 5 (figure 29a). The isobestic point at 500 nm indicates the presence of two species in equilibrium as the pH of the solution changes. The pKa value for compound

2 was 5.7 (figure 29b) with a pH detection range of 4.2 (yellow) to 5.9 (blue) as shown in figure 29c.

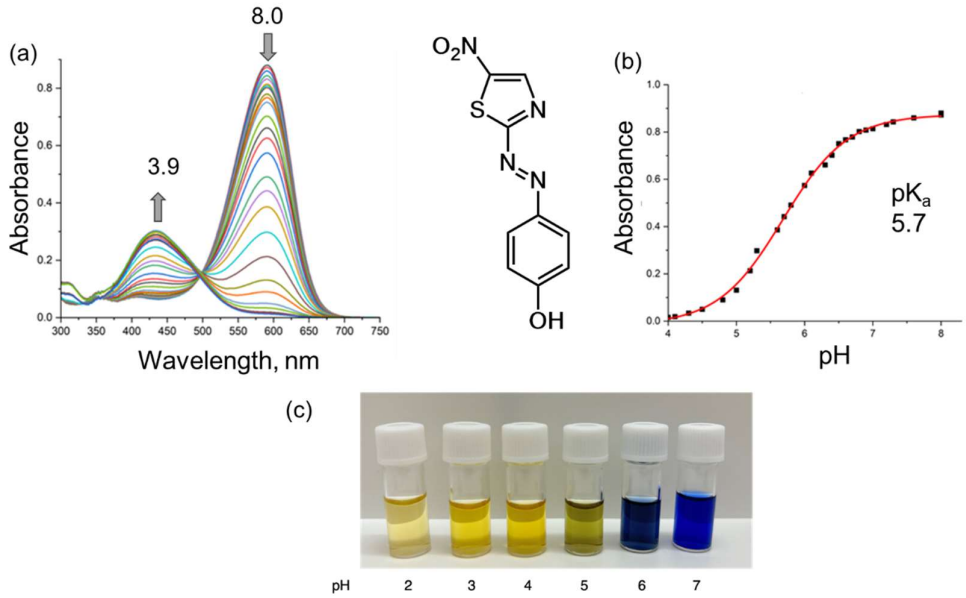

Figure 29. (a)Absorption spectra of compound **2** in aqueous solution in 0.1M HEPES buffer (pH adjusted with 0.1M NaOH) at 25 °C upon titration with 1M HCl between pH ranges mentioned in the graph. (b)Non-linear fitting of pH dependent absorbance changes at λ_{max} along with pK_a value. (c) Image showing pH dependent color changes.

In case of compound **3** the stock solution was 20 uM and the starting pH of aqueous solution was 12.2 then the solution was titrated with using minimum volume of 1M HCl (1–5 μL, portion wise) and the absorbance was measured after each addition of 1M HCl, the absorption band at 562 nm was gradually decreased with the emergence of new absorption band at 378 nm that became dominant over pH 6.6 (figure 30a). The isobestic point at 476 nm indicates the existence of two species in equilibrium as the pH of the solution changes. The pKa value for compound **3** was 7.6 (figure 30b) with a pH detection range of 6.6 (yellow) to 7.8 (violet) as shown in figure 30c.

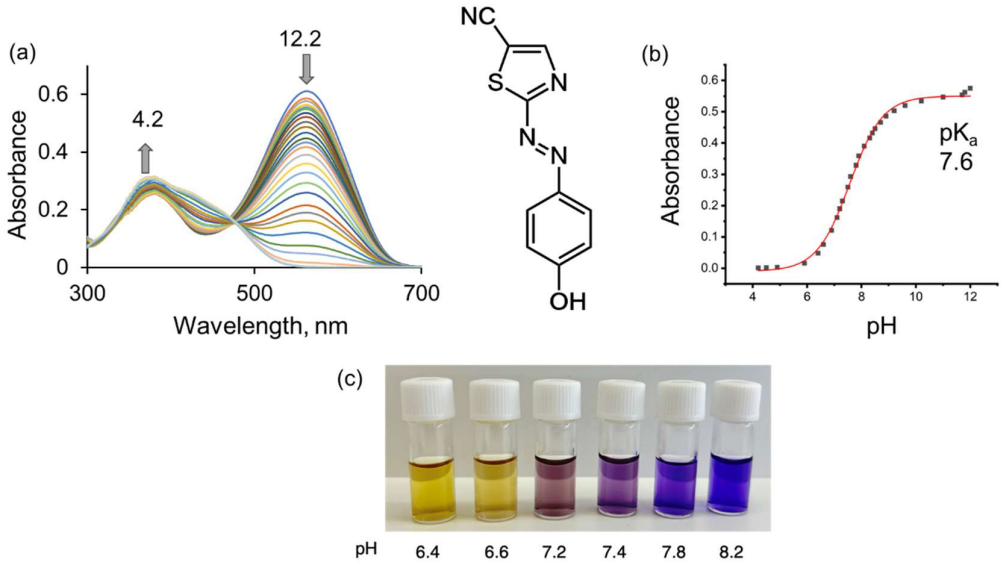

Figure 30. (a)Absorption spectra of compound **3** in aqueous solution in 0.1M HEPES buffer (pH adjusted with 0.1M NaOH) at 25 °C upon titration with 1M HCl between pH ranges mentioned in the graph. (b)Non-linear fitting of pH dependent absorbance changes at λ_{max} along with pK_a value. (c) Image showing pH dependent color changes.

In case of compound **4** the stock solution was 20 uM and the starting pH of aqueous solution was 12.2 then the solution was titrated with using minimum volume of 1M HCl (1–5 μL, portion wise) and the absorbance was measured after each addition of 1M HCl, the absorption band at 542 nm was gradually decreased with the emergence of new absorption band at 382 nm that became dominant over pH 6.6 (figure 31a). The isobestic point at 467 nm indicates the existence of two species in equilibrium as the pH of the solution changes. The pKa value for compound **4** was 8.0 (figure 31b) with a pH detection range of 6.6 (yellow) to 8.2 (violet) as shown in figure 31c.

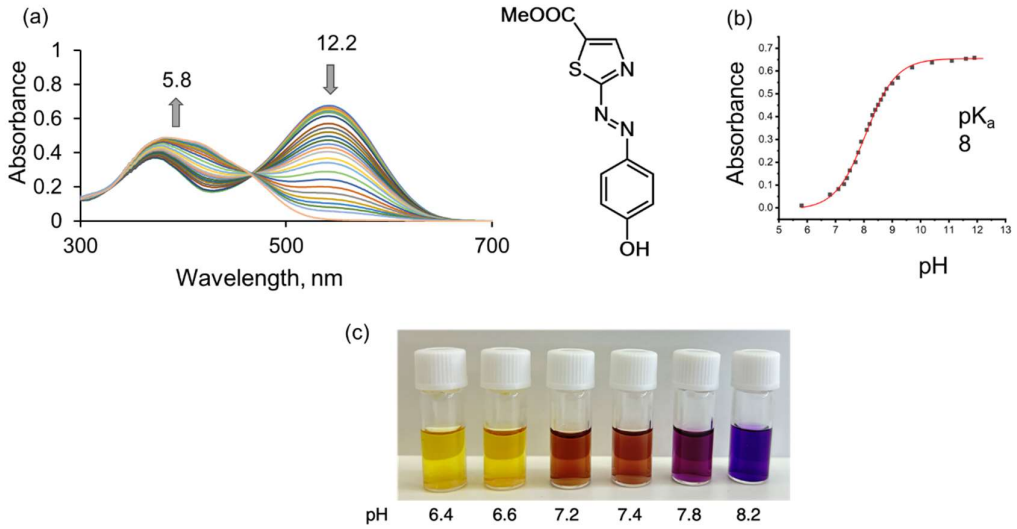

Figure 31. (a)Absorption spectra of compound **4** in aqueous solution in 0.1M HEPES buffer (pH adjusted with 0.1M NaOH) at 25 °C upon titration with 1M HCl between pH ranges mentioned in the graph. (b)Non-linear fitting of pH dependent absorbance changes at λ_{max} along with pK_a value. (c) Image showing pH dependant color changes.

In case of compound **5** the stock solution was 20 uM and the starting pH of aqueous solution was 10.2 then the solution was titrated with using minimum volume of 1M HCl (1–5 μL, portion wise) and the absorbance was measured after each addition of 1M HCl, the absorption band at 491 nm was gradually decreased with the emergence of new absorption band at 385 nm that became dominant over pH 5.2 (figure 32a). The isobestic point at 430 nm indicates the existence of two species in equilibrium as the pH of the solution changes. The pKa value for compound **5** was 6.7 (figure 32b) with a pH detection range of 5.2 (pale yellow) to 7.2 (orange) as shown in figure 32c.

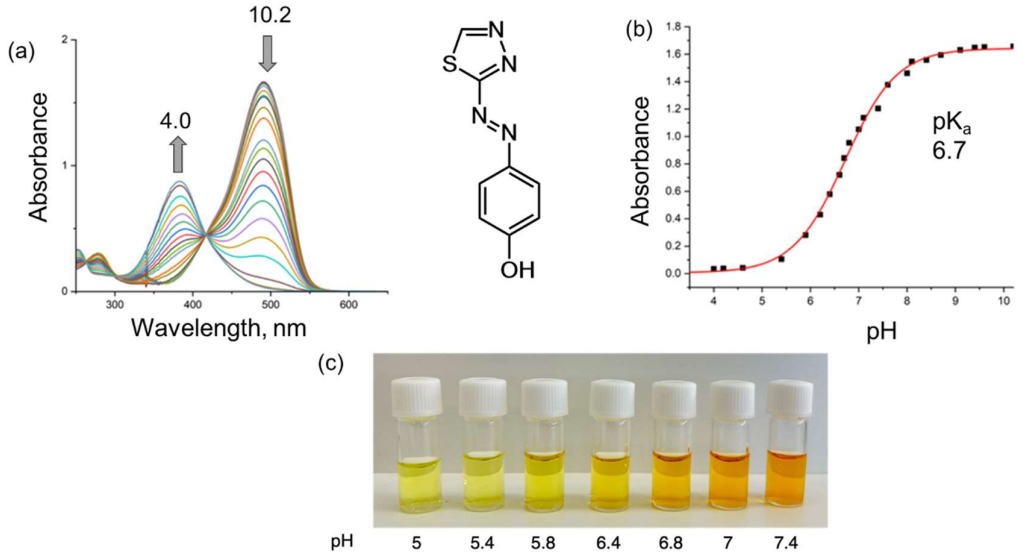

Figure 32. (a)Absorption spectra of compound **5** in aqueous solution in 0.1M HEPES buffer (pH adjusted with 0.1M NaOH) at 25 °C upon titration with 1M HCl between pH ranges mentioned in the graph. (b)Non-linear fitting of pH dependent absorbance changes at λ_{max} along with pK_a value. (c) Image showing pH dependant color changes.

In case of compound **6** the stock solution was 20 uM and the starting pH of aqueous solution was 8.9 then the solution was titrated with using minimum volume of 1M HCl (1–5 μL, portion wise) and the absorbance was measured after each addition of 1M HCl, the absorption band at 442 nm was gradually decreased with the emergence of new absorption band at 356 nm that became dominant over pH 6 (figure 33a). The isobestic point at 378 nm indicates the existence of two species in equilibrium as the pH of the solution changes. The pKa value for compound **2** was 7.8 (figure 33b) with a pH detection range of 6.0 (pale yellow) to 8.2 (yellow) as shown in figure 33c.

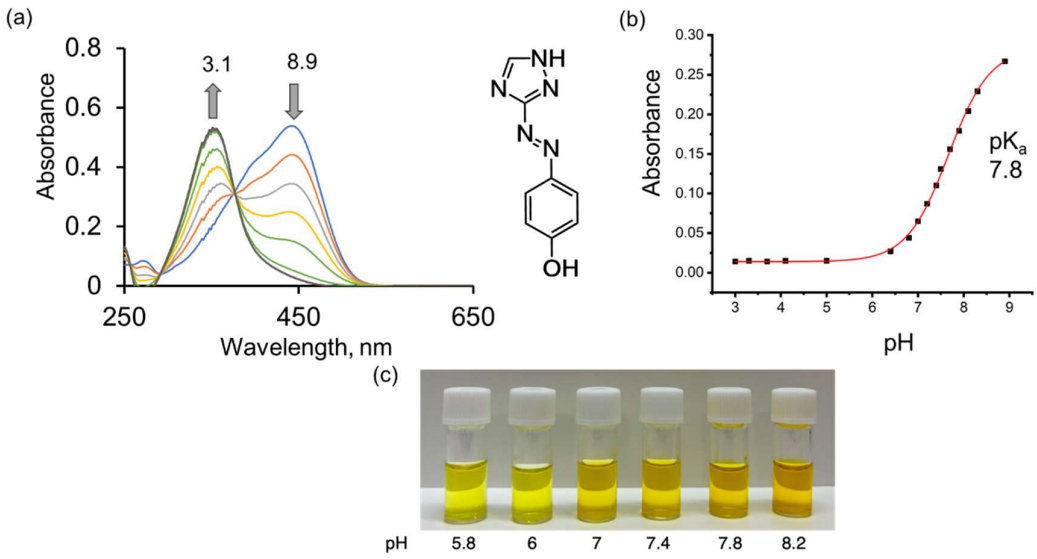

Figure 33. (a)Absorption spectra of compound **6** in aqueous solution in 0.1M HEPES buffer (pH adjusted with 0.1M NaOH) at 25 °C upon titration with 1M HCl between pH ranges mentioned in the graph. (b)Non-linear fitting of pH dependent absorbance changes at λ_{max} along with pK_a value. (c) Image showing pH dependant color changes.

In case of compound **7** the stock solution was 20 uM and the starting pH of aqueous solution was 12.0 then the solution was titrated with using minimum volume of 1M HCl (1–5 μL, portion wise) and the absorbance was measured after each addition of 1M HCl, the absorption band at 430 nm was gradually decreased with the emergence of new absorption band at 347 nm that became dominant over pH 7 (figure 34a). The isobestic point at 369 nm indicates the existence of two species in equilibrium as the pH of the solution changes. The pKa value for compound **7** was 8.6 (figure 34b) with a pH detection range of 7.0 (pale yellow) to 8.8 (yellow) as shown in figure 34c.

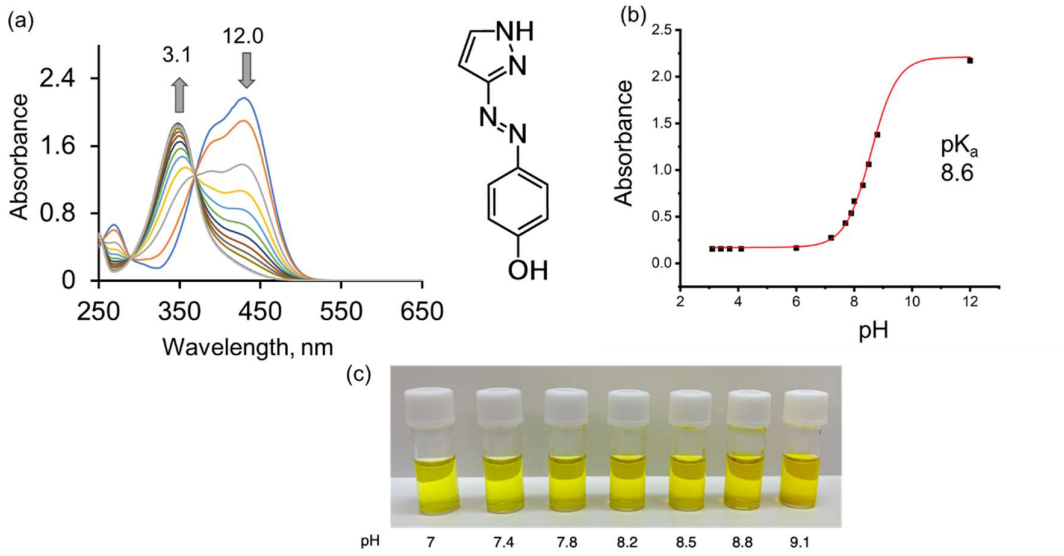

Figure 34. (a)Absorption spectra of compound **7** in aqueous solution in 0.1M HEPES buffer (pH adjusted with 0.1M NaOH) at 25 °C upon titration with 1M HCl between pH ranges mentioned in the graph. (b)Non-linear fitting of pH dependent absorbance changes at λ_{max} along with pK_a value. (c) Image showing pH dependant color changes.

In case of compound **8** the stock solution was 20 uM and the starting pH of aqueous solution was 10.5 then the solution was titrated with using minimum volume of 1M HCl (1–5 μL, portion wise) and the absorbance was measured after each addition of 1M HCl, the absorption band at 512 nm was gradually decreased with the emergence of new absorption band at 401 nm that became dominant over pH 6.6 (figure 35a). The isobestic point at 348 nm indicates the existence of two species in equilibrium as the pH of the solution changes. The pKa value for compound **8** was 7.8 (figure 35b) with a pH detection range of 6.6 (yellow) to 8.2 (red) as shown in figure 35c.

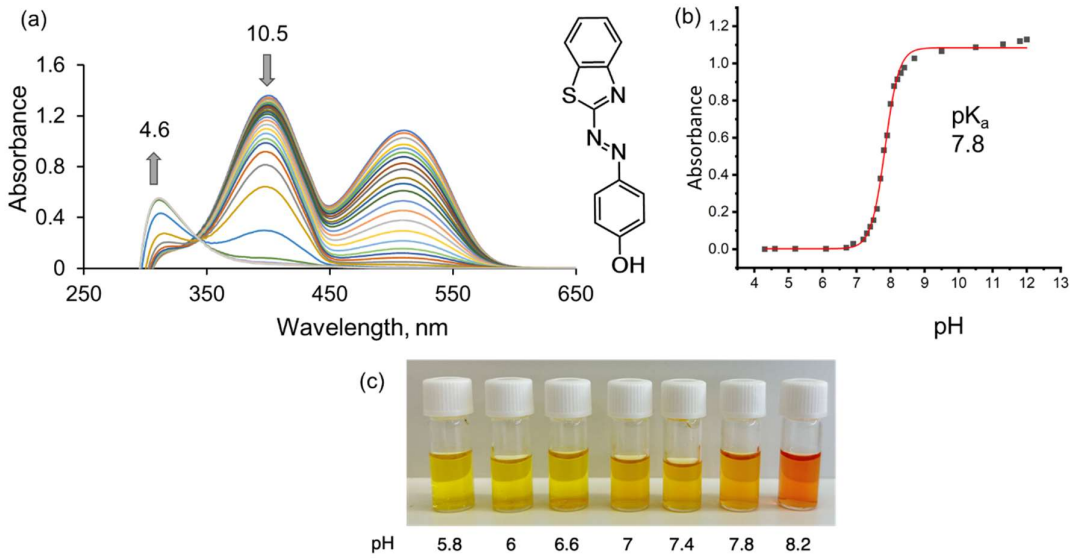

Figure 35. (a)Absorption spectra of compound **8** in aqueous solution in 0.1M HEPES buffer (pH adjusted with 0.1M NaOH) at 25 °C upon titration with 1M HCl between pH ranges mentioned in the graph. (b)Non-linear fitting of pH dependent absorbance changes at λ_{max} along with pK_a value. (c) Image showing pH dependant color changes.

In case of compound **9** the stock solution was 20 uM and the starting pH of aqueous solution was 4.9 then the solution was titrated with using minimum volume of 1M HCl (1–5 μL, portion wise) and the absorbance was measured after each addition of 1M HCl, the absorption band at 516 nm was gradually decreased with the emergence of new absorption band at 583 nm that became dominant over pH 1.5 (figure 36a). The pKa value for compound **9** was 2.3 with a pH detection range of 1.5 (figure 36b) (violet/pink) to 3.0 as shown in figure 36c.

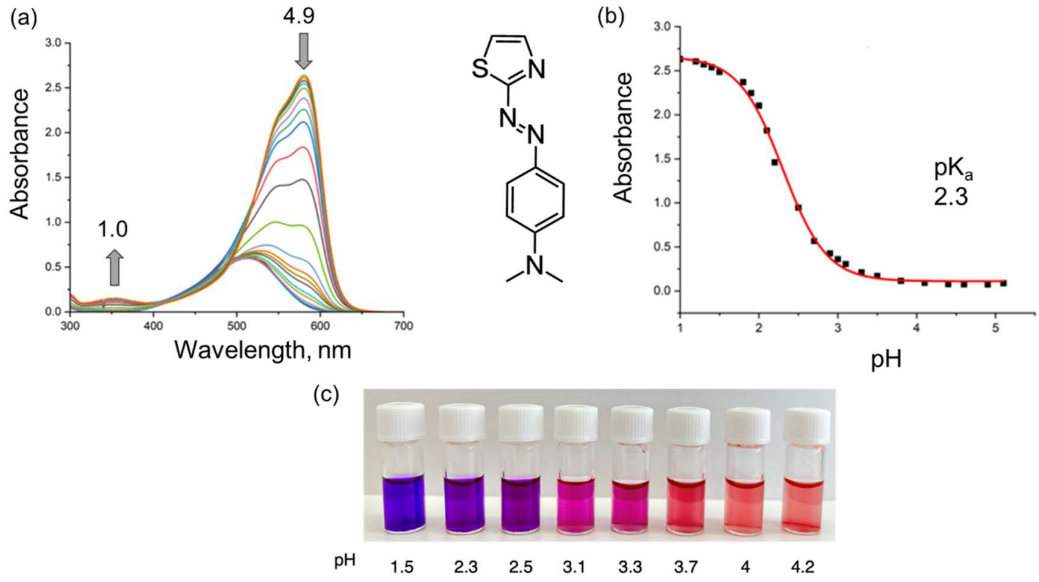

Figure 36. (a)Absorption spectra of compound **9** in aqueous solution in 0.1M HEPES buffer (pH adjusted with 0.1M NaOH) at 25 °C upon titration with 1M HCl between pH ranges mentioned in the graph. (b)Non-linear fitting of pH dependent absorbance changes at λ_{max} along with pK_a value. (c) Image showing pH dependant color changes.

In case of compound **10** the stock solution was 20 uM and the starting pH of aqueous solution was 10.5 then the solution was titrated with using minimum volume of 1M HCl (1–5 μL, portion wise) and the absorbance was measured after each addition of 1M HCl, the absorption band at 399 nm was gradually decreased with the emergence of new absorption band at 393 nm that became dominant over pH 7 (figure 37). Compound **10** did not show any spectral changes for different pH solutions. This indicates the importance of OH group at the para position on the phenyl ring together with heteroaryl segments for showing near-neutral pH detection.

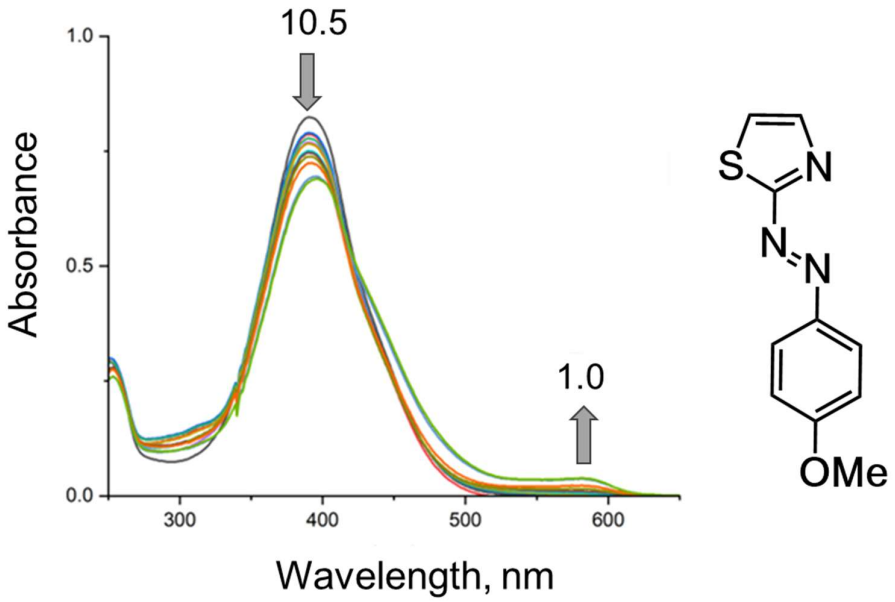

Figure 37. Absorption spectra of compound **10** in aqueous solution in 0.1M HEPES buffer (pH adjusted with 0.1M NaOH) at 25 °C upon titration with 1M HCl between pH ranges mentioned in the graph.

In case of compound **2**, having an electron withdrawing NO_2 substituent on the thiazole ring, showed red shift in the absorption bands as compared to compound **1** i.e., 435 nm in low pH (less than 4) and at 590 nm in high pH (more than 6) aqueous solutions as shown in figure. So, its pK_a value was 5.7 which is not in neutral range, so I thought to further adjust the pH detection range to near-neutral range by introducing an electron donating methoxy group at the phenyl segment.

The stock solution compound **11** was 20 uM and the starting pH of aqueous solution was 9.1 then the solution was titrated with using minimum volume of 1M HCl (1–5 μL, portion wise) and the absorbance was measured after each addition of 1M HCl, the absorption band at 601 and was gradually decreased with the emergence of new absorption band at 448 nm that became dominant over pH 6 (figure 38a). Below pH 6, I observed precipitation and accordingly the constant decrease of absorbance from the compound. The pKa value for compound **11** was 6.3 as shown in figure 36b.

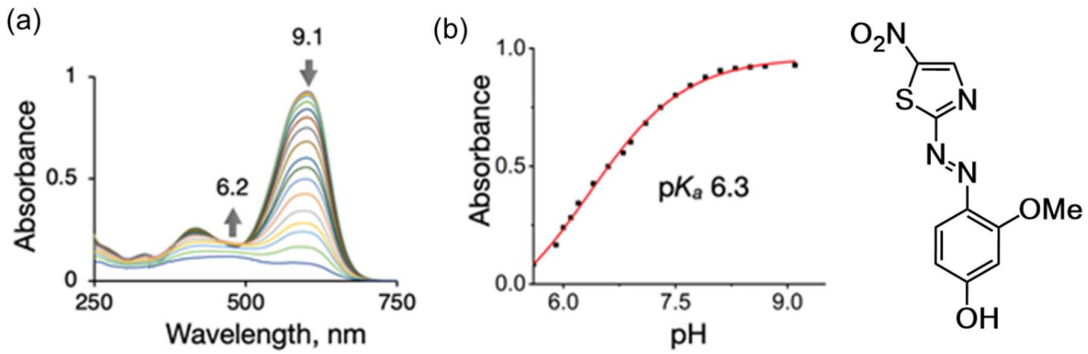

Figure 38. Absorption spectra of compound **11** in aqueous solution in 0.1M HEPES buffer (pH adjusted with 0.1M NaOH) at 25 °C upon titration with 1M HCl between pH ranges mentioned in the graph. (b)Non-linear fitting of pH dependent absorbance changes at λ_{max} along with pK_a value.

To conclude, in organic solvents, the compound **1-10** exhibited absorption bands (λ_{max} = 338–490 nm) assignable to the $\pi \rightarrow \pi^*$ electronic transition (Figure 27a, figure 39). In aqueous solvents, the compounds exhibited a significantly red-shifted absorption bands depending on the solution pH (Figure 39). For instance, compound **1**, exhibited an absorption band (λ_{max} = 479 nm, pH 10.2, water) that seemingly contain both $\pi \rightarrow \pi^*$ and $n \rightarrow \pi^*$ electronic transitions (Figure 28a). I then performed UV-vis titration of the compounds for a range of pH. Figure 28a shows the absorption spectra of compound **1** (20 μM, pH 10.2 to 4) in aqueous solution where the absorption band at 487 nm (λ_{max}) gradually decreased with the emergence of new absorption band at 391 nm (λ_{max}) that became dominant over the pH 7. The isosbestic point at ~420 nm indicated the existence of two species in equilibrium as the pH changed. The pK_a value calculated from the absorbance changes at 487 nm was 7.4 (figure 28b). Accordingly, the color of the aqueous solution at pH 6 and 7.8 observable to the naked eye was yellow and red,

respectively (Figure 28c). The presence of substituent at the thiazole segment, as in the case of **2**–**4**, significantly affected their light absorption properties and colors in aqueous solution. For instance, the compound **2**, having an electron withdrawing NO_2 substituent on the thiazole ring, showed absorption bands (λ_{max}) at 435 nm in low pH (<4) and at 590 nm in high pH (>6) aqueous solutions (Figure 29a) with yellow and deep blue colors, respectively (Figure 29c). The pK_a value was 5.7 at 25 °C (figure 29b) with a pH detection range of 4.2–5.9. The compounds **3** and **4**, having CN and CO_2Me substituents, respectively, showed nearly identical spectral characteristics in acid and base solutions with pK_a values 7.5 (**3**) and 8.0 (**4**) (Figure 30, 31). I then studied the absorption spectral changes in different solution pH for the compounds **5**–**8** that has thiadiazole, triazole, pyrazole or benzothiazole "heteroaryls" connected to the *para* hydroxy phenyl azo segment. Both the λ_{max} and pK_a altered significantly depending on the type of "heteroaryls" present in the compound (Figure 39). The compound **5** having thiadiazole heteroaryl showed near-neutral pK_a value 6.71 (figure 32b) with distinct solution colors of pale yellow (pH <5.2) and orange (>7.2) (Figure 32c). However, in the case of compounds **6** (pK_a 7.87) and **7** (pK_a 8.58) having triazole and pyrazole heteroaryls, respectively, we observed only a marginal change in the solutions colors from pale yellow to yellow in different solution pH (Figure 33c, 34c). The compound **8** having benzothiazole heteroaryl showed identical spectral changes to that of compound **1** with pK_a 7.8 (figure 35b) and distinct solution colors of yellow (pH <6.6) and red (>8.2) (Figure 35c).

I also studied the effect of substituent at *para* position on the phenyl ring by replacing the electron donating OH group with NMe_2 (compound **9**) or OMe (compound **10**) group. Compound **9** showed spectral changes and color only in a highly acidic solution (pH 1.5–3.0; pK_a 2.3) (Figure 36). On the other hand, compound **10** with OMe substituent did not show any spectral changes for different solution pH in our experimental conditions (Figure 37). These

results indicate the importance of OH group at the *para* position on the phenyl ring together with heteroaryl segments for showing the near-neutral pH detection.

	$\pi-\pi^*$ (*acid*) λ_{max}, nm	$\pi-\pi^*$ (*base*) λ_{max}, nm	$\pi-\pi^*$ (*organic*)* λ_{max}, nm	pK_a (25 °C)	pH range	Color *(acid)*	Color *(base)*
1	391	487	397	7.41	6.1–7.9	Yellow	Red
2	435	590	448**	5.68	4.2–5.9	Yellow	Blue
3	378	562	374	7.5	6.6–7.8	Yellow	Violet
4	382	542	374	8.0	6.6–8.2	Yellow	Violet
5	385	491	393**	6.71	5.2–7.2	Pale yellow	Orange
6	356	442	345	7.87	6.0–8.2	Pale yellow	Yellow
7	347	430	338	8.58	7.0–8.8	Pale yellow	Yellow
8	401	512	399	7.8	6.6–8.2	Yellow	Red
9	583	516	490	2.30	1.5–3.0	Violet/ Pink	–
10	393	399	388	–	–	Orange	Orange

* CH_3CN, ** DCM

Figure 39. Overall spectral parameters and changes in solution colors of compounds **1**-**10**.

Repeatability of pH indicators

Reliable pH indicators should consistently show specific color changes at designated pH levels, ensuring that measurements are repeatable and dependable. High reproducibility indicates that the indicator will yield the same pH reading under the same conditions, which is essential for accurate measurements. Additionally, pH indicators should retain their properties over time and under various storage conditions to guarantee long-term reliability. All compounds showed good reversibility on repeated switching of aqueous solutions of different pH.

In case of compound **1**, 3 cycles were performed at two different pH i.e., 7.8 and 6. Compound **1** gave red at pH 7.8 and yellow at pH 6 on repeated switching of pH solutions without any deterioration and hence indicates excellent reproducibility (Figure 41). Similar results were obtained for compound **2**, **5**, and **7** (Figure 41, 42, 43).

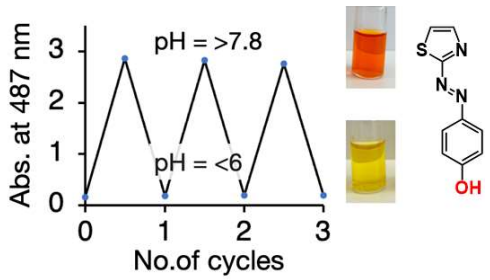

Figure 40: Reversibility of the absorption spectral changes of **1** for pH variation >7.8 and <6; Images showing the changes in solution color of **1** (7.8 [red]), pH 6 [yellow])

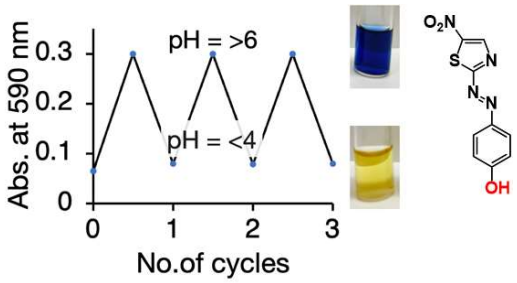

Figure 41: Reversibility of the absorption spectral changes of **2** for pH variation >6 and <4; Images showing the changes in solution color of **2** (6 [blue], pH 4 [yellow])

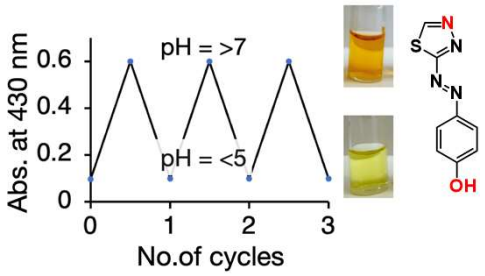

Figure 42: Reversibility of the absorption spectral changes of **5** for pH variation >7 and <5; Images showing the changes in solution color of **5** (7 [orange], pH 5 [pale yellow])

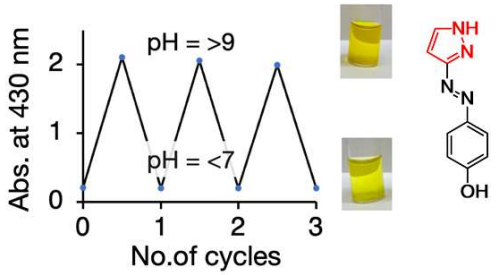

Figure 43: Reversibility of the absorption spectral changes of **7** for pH variation >9 and <7; Images showing the changes in solution color of **7** (9.1 [yellow], pH 7 [pale yellow])

Computational calculations

Density Functional Theory (DFT) calculations were performed to investigate the effect of charge transfer on the pKa values of two compounds compound **1** and compound **2**. Using the 6-31+G(d,p) basis set and Becke's three-parameter hybrid exchange along with the Lee-Yang-Parr correlation functional, including Grimme dispersion corrections in an aqueous medium, the electronic properties and behavior of these compounds were examined. The energy-optimized structures of both compounds are found to be planar in their ground state. This planarity influences their electronic properties and interactions. In both compounds, the electron density in the highest occupied molecular orbital (HOMO) is localized on the hydroxyphenyl portion, while the electron density in the lowest unoccupied molecular orbital (LUMO) shifts to the N=N bond or thiazole ring. This shift indicates significant changes in electronic distribution upon excitation. The calculated absorption spectra show a maximum absorption wavelength (λ_{max}) of 416 nm for compound **1** and 480 nm for compound **2**. This difference reflects the distinct electronic environments and transitions within each compound. For compound **2**, the DFT calculations indicate a significant charge transfer from the donor (hydroxyphenyl moiety) to the acceptor (nitrothiazole moiety) in the excited state, resulting in absorption at a longer wavelength. Additionally, the absorption spectra of the anionic forms of both compounds display even more pronounced red-shifts, with λ_{max} at 462 nm for compound **1** and 539 nm for compound **2**. This suggests that the charge transfer from donor to acceptor is

stronger in the anionic forms compared to the neutral forms. The theoretically calculated pK_a values are 8.4 for compound **1** and 3.4 for compound **2**. Experimentally, similar trends are observed, with pKa values of 7.41 for compound **1** and 5.68 for compound **2**, which support the theoretical predictions.

At low pH, Compound **1** appears yellow. As the pH increases, it loses a proton, resulting in a negative charge (**1**$^-$) that becomes delocalized throughout the molecule. This delocalization leads to a red-shifted absorption spectrum, causing the solution to turn red. In the case of Compound **2**, an increase in pH also results in the loss of a proton, which produces a negative charge (**2**$^-$) that delocalizes throughout the nitrothiazole moiety. This delocalization causes the solution to exhibit a deep blue color.

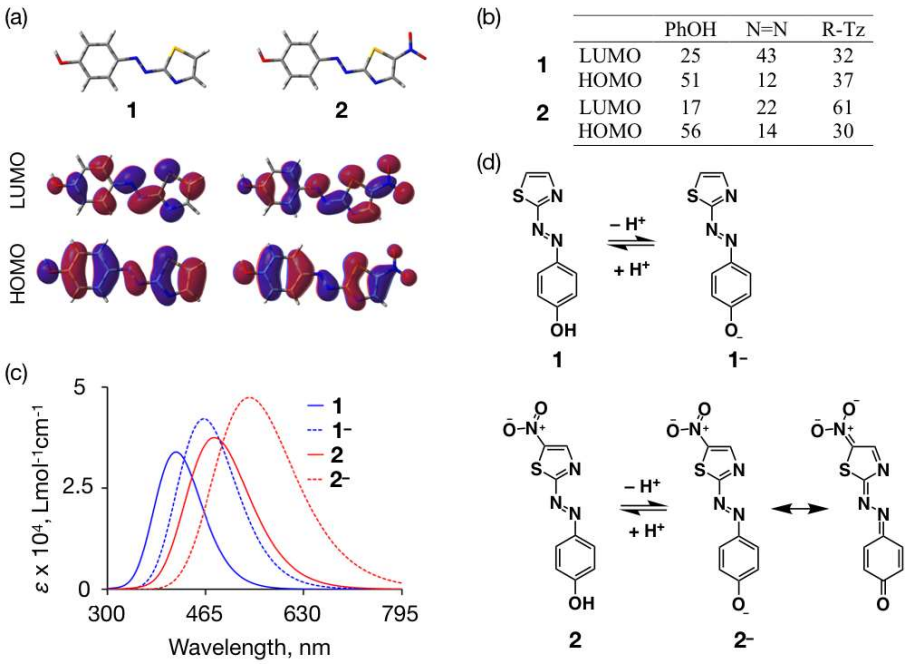

Figure 44: (a) The geometry optimized structures and the frontier molecular orbitals (HOMO and LUMO) of **1** and **2** in the ground state. (b) Table showing HOMO and LUMO electron distribution (%) in different moieties (hydroxy phenyl [PhOH], azo bond [N=N], and thiazole [R-Tz]; R = H/NO_2) of **1** and **2**. (c) Theoretically calculated absorption spectra of **1** (blue curve) and **2** (red curve) in the neutral (solid curve) and anion (dotted curve) forms in aqueous medium. (d) Plausible changes in the chemical structures of **1** and **2** in acid ($+H^+$) or base ($-H^+$) solutions.

Calculated pK_a of **1** and **2** in the presence and absence of explicit water.

Molecule	No. of explicit water	pK_a
1	0	9.0
	1	8.4
2	0	3.2
	1	3.4

Biological studies

Stability in glutathione containing solution

A key requirement before performing biological studies is to check stability in a reductive environment. Compounds **1**–**8** exhibited stability in the presence of reductants, as no decrease in absorbance was observed when they were incubated in a glutathione-containing aqueous solution. A DMSO stock solution of compound **1** was diluted in aqueous solution (pH 7.8–8.0) containing glutathione (1 mM) and measured absorbance at 490 nm every 2 hours for 24 h (figure 45). Similarly, all the compounds showed stability in presence of 1mM glutathione (Figure 46-52).

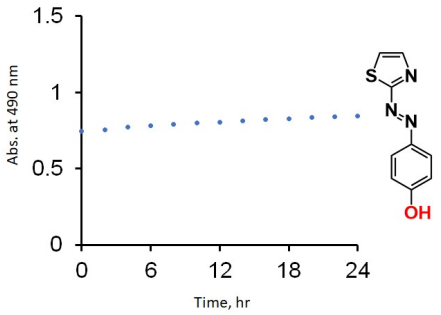

Figure 45: Absorbance changes of compounds **1** over time after incubation for 24 hours at 37 °C in aqueous solution containing glutathione (1 mM) reductant.

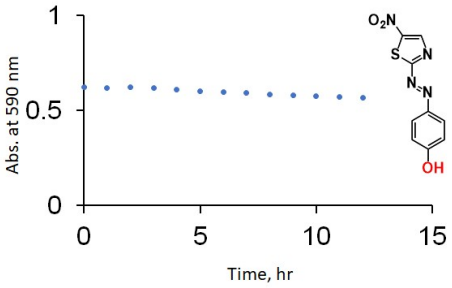

Figure 46: Absorbance changes of compounds **2** over time after incubation for 12 hours at 37 °C in aqueous solution containing glutathione (1 mM) reductant.

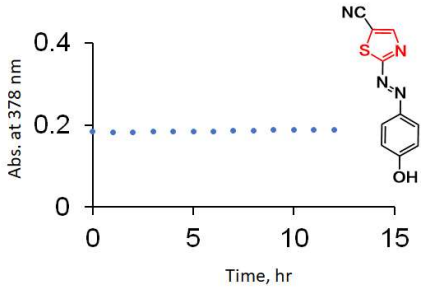

Figure 47: Absorbance changes of compounds **3** over time after incubation for 12 hours at 37 °C in aqueous solution containing glutathione (1 mM) reductant.

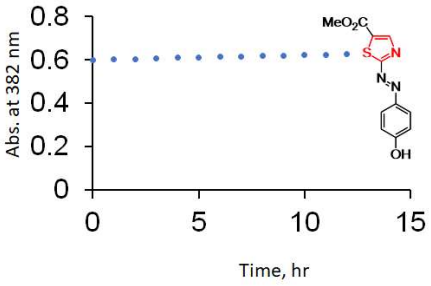

Figure 48: Absorbance changes of compounds **4** over time after incubation for 12 hours at 37 °C in aqueous solution containing glutathione (1 mM) reductant.

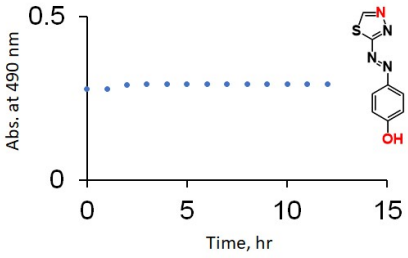

Figure 49: Absorbance changes of compounds **5** over time after incubation for 12 hours at 37 °C in aqueous solution containing glutathione (1 mM) reductant.

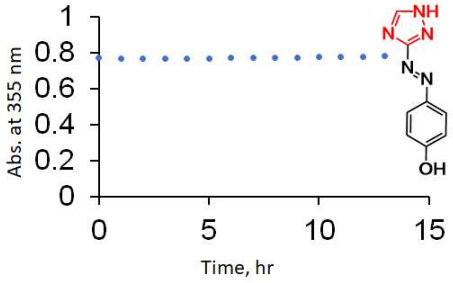

Figure 50: Absorbance changes of compounds **6** over time after incubation for 12 hours at 37 °C in aqueous solution containing glutathione (1 mM) reductant.

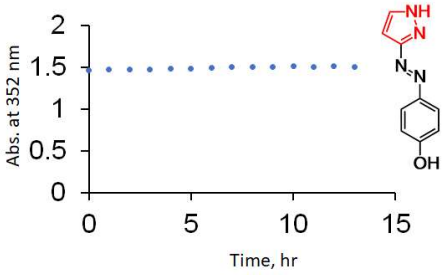

Figure 51: Absorbance changes of compounds **7** over time after incubation for 12 hours at 37 °C in aqueous solution containing glutathione (1 mM) reductant.

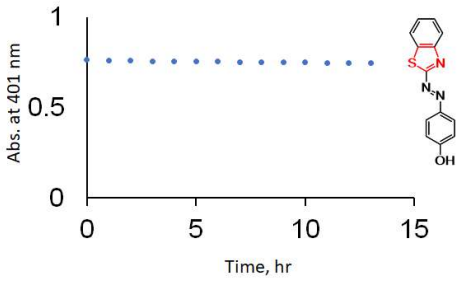

Figure 52: Absorbance changes of compounds **8** over time after incubation for 12 hours at 37 °C in aqueous solution containing glutathione (1 mM) reductant.

Additionally for the biological experiments, the compounds should show distinct color changes within a narrow near neutral pH range. While compounds **1** and **3**–**5** met these criteria, I selected compound **1** to demonstrate the pH-sensing ability of the novel heteroarenes.

Calculation of pKa in IMDM buffer

For compound **1** UV-vis titration studies was also done in DMEM cell culture medium at 25° C. I first confirmed that **1** can detect the pH variation in cell-free culture medium (IMDM) containing serum protein (10%) with pK_a 7.5, which was identical to the pK_a observed in aqueous solution. A DMSO stock solution of compound **1** was diluted in commercial IMDM (pH 7–7.4) and adjusted the pH upto 8.3 by NaOH solution. For titration experiment, a dilute HCl added portion wise and measured absorbance. Non-linear fitting of the pH dependent absorbance changes gave p*K*a 7.5 similar as that in aqueous solutions (Figure 53).

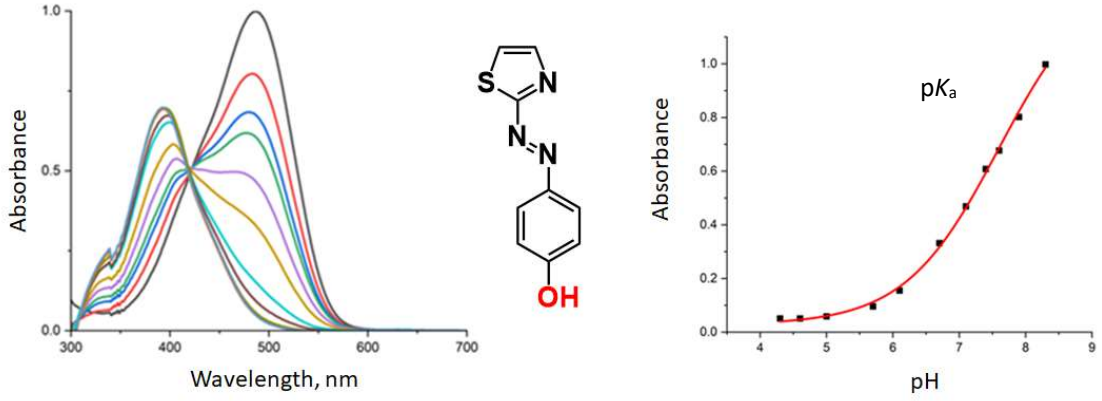

Figure 53. Absorption spectra of compound **1** in cell culture medium, Graph showing the non-linear fitting of the pH dependent absorbance changes of **1** at λ_{max} in IMDM culture medium (pK_a 7.5).

Cell culture and detection of pH variation in culture media containing HeLa cells

To investigate the detection of pH variation in growing cancer cells, HeLa cells were seeded in a 96-well plate with cell density of 15 x 10^4 cells per well and incubated for 24 hours at 37 °C with 5% CO_2. After this period, the medium was replaced with fresh medium containing compound **1** at concentrations ranging from 6.25 to 50 μM, and the cells were further incubated for 53 hours in the absence of CO_2. Absorbance measurements were taken directly from the culture plate. For comparison, separate culture plates containing only DMEM medium without HeLa cells were prepared under identical experimental conditions. Remarkably, the color of the medium in wells containing the HeLa cells changed from red to orange, indicating a decrease in pH (Figure 54). This color change was noticeable to the naked eye, even at relatively low concentrations (12.5 μM), corresponding to a change in pH from 7.7 (red) to 6.7 (orange) (Figure 55). Conversely, the wells with only DMEM medium showed no color change. These results suggest that the proliferation of HeLa cells leads to a pH variation in the culture medium, detected by compound **1** as a color change from red to orange, indicating a pH of less than 7.

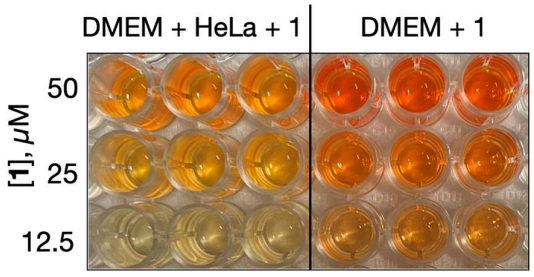

Figure 54. Image showing a part of the culture plate containing DMEM medium after incubation of **1 (**12.5–50 μM) in the presence (left) and absence (right) of HeLa cells.

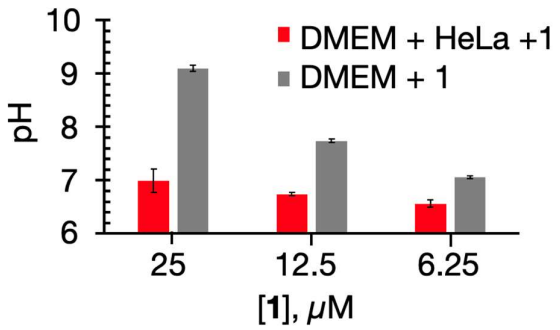

Figure 55. Bar graph showing the change in pH of DMEM medium after incubation of **1 (**6.25–25 μM) in the presence (red bar) and absence (gray bar) of HeLa cells (n = 3 independent experimental sets).

Cytotoxicity assay

HeLa cells (5.0×10^3 cells per well) were plated onto a 96-well plate with a lid and supplied with 100 mL of Dulbecco's Minimal Essential Medium (DMEM) containing 10% fetal bovine serum (FBS). After incubating at 37 °C under 5% CO_2 for 24 hours in DMEM with 10% FBS, the cells were rinsed with 200 mL of Dulbecco's phosphate-buffered saline (D-PBS) and then treated with fresh DMEM containing different concentration of compound **1**. The cells were incubated for an additional 48 hours. After this, 10 mL of CCK-8 solution was added to each well and the plate was incubated at 37 °C under 5% CO_2 for 3 hours. Absorbance was then measured at 450 nm. As indicated in the figure 56, no cytotoxicity was observed within the concentration range used in the experiments.

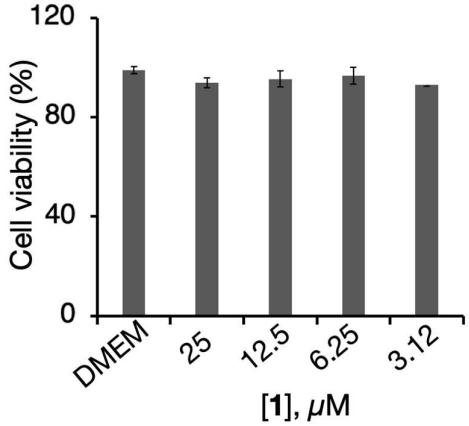

Figure 56: Bar graph showing the cell viability of HeLa cells after incubation of **1 (**3.12–25 μM) in DMEM medium for 48 hours (n = 3 wells).

Conclusion

In this study, we have developed a novel series of azoheteroarene dyes that incorporate various heteroaromatic structures, including thiazole, thiadiazole, triazole, pyrazole, and benzothiazole. These dyes demonstrate an impressive ability to detect pH changes in aqueous solutions by utilizing their unique light absorption properties and exhibiting noticeable color changes over a narrow pH range, which are visible to the naked eye. The dyes display distinct absorption spectra in aqueous solutions that vary with changes in pH. This optical property enables direct pH monitoring without the need for complex instrumentation. Among these compounds, those containing thiazole or thiadiazole heteroarenes are particularly effective at detecting pH variations in near-neutral aqueous solutions. These compounds are responsive to minor pH shifts, making them suitable for applications requiring precise pH monitoring. Experimental tests confirmed that the dyes exhibit visible color shifts in response to pH changes. This was effectively demonstrated in various aqueous environments, showcasing the practical utility of these compounds. Density Functional Theory (DFT) calculations were performed to comprehend the charge transfer mechanisms that underlie the pH sensitivity. The calculations revealed significant changes in electron density distribution upon protonation or deprotonation, which leads to observable color changes. I specifically demonstrated the effectiveness of compound **1**, for monitoring pH levels in culture media containing cancer cells. The dye responded to the acidic environment typically associated with cancer cells (pH 6.4–7.0), distinguishing it from the near-neutral pH of normal cells (pH 7.2–7.5). The ability of these dyes to exhibit distinct color changes in response to pH makes them promising tools for distinguishing between cancerous and normal tissues. This application is particularly valuable in medical diagnostics and research, providing a non-invasive and visual method for identifying cancerous tissues based on their acidic microenvironment. The novel azoheteroarene dyes

represent a significant advancement in the field of pH detection. Further research can find their potential, particularly in the context of cancer diagnostics and other biomedical applications.

References

1. Y.-A. Son, S.-H. Kim, *Dyes Pigm.* **2005**, *64*, 153.
2. T. Doussineau, M. Smaïhi, G. J. Mohr, *Adv. Funct. Mater.* **2009**, *19*, 117.
3. P. Qin, D. Huang, *Chem. Lett.* **2013**, *42*, 1344.
4. H. Chen, X. Wang, X. Song, T. Zhou, Y. Jiang, X. Chen, *Sens. Actuators, B* **2010**, *146*, 278.
5. S. Charier, O. Ruel, J.-B. Baudin, D. Alcor, J.-F. Allemand, A. Meglio, L. Jullien, *Angew. Chem., Int. Ed.* **2004**, *43*, 4785.
6. R. Badugu, J. R. Lakowicz, C. D. Geddes, *Talanta* **2005**, *66*, 569.
7. S. Yao, K. J. Schafer-Hales, K. D. Belfield, *Org. Lett.* **2007**, *9*, 5645.
8. R. Badugu, J. R. Lakowicz, C. D. Geddes, *Dyes Pigm.* **2004**, *61*, 227.
9. A. Pastore, D. Badocco, S. Bogialli, L. Cappellin, P. Pastore. *Microchem. J.* **2021**, *160*, 105605.
10. M. A. Cardona, D. Makuc, K. Szaciłowski, J. Plavec, D.C. Magri, *ACS Omega* **2017**, *2*, 6159.
11. W. Lv, C. Wang, L. Ji, T. Deng, S. Yang, T. Zhu, S. Liu, Q. Zhao. *J. Mat. Chem. C.* **2024**, *12*, 8777.
12. B. Shan, Y. Deng, B. Tang, R. Lu, S. Zhang, *Chem. Lett.*, **2016**, *45*, 472.
13. M. A. Cardona, D. C. Magri, *Tetrahedron Lett.* **2014***, 55,* 4559.
14. F. L. Coelho, C. de Ávila Braga, G. M. Zanotto, E. S. Gil, L. F. Campo, P. F. B. Gonçalves, F. S. Rodembusch, F. da S. Santos, *Sens Actuators B Chem,* **2018***, 259,* 514.
15. Y. Berthois, J.A. Katzenellenbogen, B.S. Katzenellenbogen, *Proc. Natl. Acad. Sci. U. S. A.* **1986**, *83*, 2946.
16. C. E. Weston, R. D. Richardson, P. R. Haycock, A. J. White, M. J. Fuchter, *J. Am. Chem. Soc.* **2014***, 136*, 11878.

17. A. K. Gaur, H. Kumar, D. Gupta, I. P. Tom, D. N. Nampoothiry, S.K. Thakur, A. Mahadevan, S. Singh, S. Venkataramani *J. Org. Chem.* **2022**, *87*, 6541.

18. R. Lin, P. K. Hashim, S. Sahu, A. S. Amrutha, N. M. Cheruthu, S. Thazhathethil, K. Takahashi, T. Nakamura, T. Kikukawa, N. Tamaoki, *J. Am. Chem. Soc.* **2023**, *145*, 9072.

19. P. K. Hashim, S. Sahu, K. Takahashi, S. Thazhathethil, T. Nakamura, N. Tamaoki, *Chem. Eur. J.* **2024**, *30*, e202400047.

20. T. Dang, Z. Zhang and T. Li. *J. Am. Chem. Soc.,* **2024***, 146,* 19609.

21. S. Crespi, N. A. Simeth, B. König, *Nat. Chem. Rev.* **2019**, **3**, 133.

22. Z.-Y. Zhang, D. Dong, T. Bösking, T. Dang, C. Liu, W. Sun, M. Xie, S. Hecht, T. Li, *Angew. Chem. Int. Ed.* **2024**, 63, e202404528

23. F. Höglsperger, F. A. Larik, C. Bai, M. D. Seyfried, C. Daniliuc, H. Klaasen, P. Thordarson, J. E. Beves, B. J. Ravoo, *Chem. Eur. J.* **2023**, 29, e202302069.

24. a) G. M. Sheldrick, *Acta. Cryst*., **2015**, A71, 3–8. b) G. M. Sheldrick, *Acta. Cryst*., **2015**, C71, 3–8. c) O. V. Dolomanov, L. J. Bourhis, R. J. Gildea, J. A. K. Howard, H. Puschmann, *J. Appl. Cryst*., **2009**, 42, 339–341.

25. P. R. Spackman, M. J. Turner, J. J. McKinnon, S. K. Wolff, D. J. Grimwood, D. Jayatilaka, M. A. Spackman, **2021**, J. *Appl. Cryst.* 54, 3, 1006–1011.

26. M. J. Frisch, G. W. Trucks, H. B. Schlegel, G. E. S.; M. A. Robb, J. R. Cheeseman, G. Scalmani, V. Barone, B. M.; G. A. Petersson, H. Nakatsuji, M. Caricato, X. Li, H. P. H.; A. F. Izmaylov, J. Bloino, G. Zheng, J. L. Sonnenberg, M. H.; M. Ehara, K. Toyota, R. Fukuda, J. Hasegawa, M. Ishida, T. N.; Y. Honda, O. Kitao, H. Nakai, T. Vreven, J. A. Montgomery, J.; J. E. Peralta, F. Ogliaro, M. Bearpark, J. J. Heyd, E. B.; K. N. Kudin, V. N. Staroverov, T. Keith, R. Kobayashi, J. N.; K. Raghavachari, A. Rendell, J. C. Burant, S. S. Iyengar, J. T.; M. Cossi, N. Rega, J. M. Millam, M. Klene, J. E. Knox, J. B. C.; V.

Bakken, C. Adamo, J. Jaramillo, R. Gomperts, R. E. S.; O. Yazyev, A. J. Austin, R. Cammi, C. Pomelli, J. W. O.; R. L. Martin, K. Morokuma, V. G. Zakrzewski, G. A. V.; P. Salvador, J. J. Dannenberg, S. Dapprich, A. D. D.; O. Farkas, J. B. Foresman, J. V. Ortiz, J. C.; Fox., and D. J. Gaussian 09, Revision D.01. Gaussian, Inc., Wallingford CT **2013**.

27. Roy Dennington, Todd A. Keith, and J. M. M. GaussView, Version 6.1. Semichem Inc., Shawnee Mission, KS **2016**.

28. Hohenberg, P.; Kohn, W. Inhomogeneous Electron Gas. *Phys. Rev.* **1964**, *136* .

29. Gross, E. K. U.; Dobson, J. F.; Petersilka, M. Density Functional Theory of Time-Dependent Phenomena. *Density Funct. Theory II* **1996**, 81–172.

30. Kohn, W.; Sham, L. J. Self-Consistent Equations Including Exchange and Correlation Effects. *Phys. Rev.* **1965**, *140* (4A), A1133.

31. Lee, C.; Yang, W.; Parr, R. G. Development of the Colle-Salvetti Correlation-Energy Formula into a Functional of the Electron Density. *Phys. Rev. B* **1988**, *37* (2), 785.

32. Miertuš, S.; Scrocco, E.; Tomasi, J. Electrostatic Interaction of a Solute with a Continuum. A Direct Utilizaion of AB Initio Molecular Potentials for the Prevision of Solvent Effects. *Chem. Phys.* **1981**, *55* (1), 117–129.

33. Klicić, J. J.; Friesner, R. A.; Liu, S. Y.; Guida, W. C. Accurate Prediction of Acidity Constants in Aqueous Solution via Density Functional Theory and Self-Consistent Reaction Field Methods. *J. Phys. Chem. A* **2002**, *106* (7), 1327–1335.

34. Thapa, B.; Schlegel, H. B. Improved PKa Prediction of Substituted Alcohols, Phenols, and Hydroperoxides in Aqueous Medium Using Density Functional Theory and a Cluster-Continuum Solvation Model. *J. Phys. Chem. A* **2017**, *121* (24), 4698–4706.

35. Thapa, B.; Schlegel, H. B. Density Functional Theory Calculation of PKa's of Thiols in Aqueous Solution Using Explicit Water Molecules and the Polarizable Continuum Model. *J. Phys. Chem. A* **2016**, *120* (28), 5726–5735.

XYZ Coordinate of DFT

Table S2. XYZ coordinate of **1**.

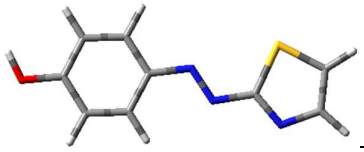

	X	Y	Z
S	-2.9509	1.176615	-0.00026
N	-0.15442	0.328968	0.000063
N	-0.88164	-0.70893	0.000138
N	-3.1217	-1.4267	0.000053
C	1.228788	0.121802	0.000084
C	1.859429	-1.14398	0.000191
H	1.254845	-2.04339	0.000262
C	-2.24374	-0.45059	-9E-06
C	2.018005	1.286626	-6E-06
H	1.524036	2.253038	-8.7E-05
C	-4.401	-0.9329	-0.0001
H	-5.23709	-1.62144	-7.4E-05
C	4.019724	-0.05589	0.000118
C	3.240231	-1.22977	0.000208
C	3.405994	1.205637	0.000012
H	4.010429	2.10817	-5.6E-05
C	-4.51534	0.433887	-0.00028
H	3.742127	-2.19169	0.000291
O	5.368578	-0.2196	0.000142
H	5.822607	0.636096	0.000076
H	-5.41939	1.027782	-0.00042

Table S3. XYZ coordinate of **1**$^{-}$.

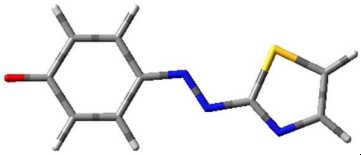

	X	Y	Z
S	-2.84314	1.176238	-0.00022
N	-0.09274	0.276226	-4.1E-05
N	-0.84489	-0.7764	0.000039
N	-3.11159	-1.42649	0.000035
C	1.256094	0.098913	0.000028
C	1.929661	-1.16555	0.000175
H	1.334479	-2.073	0.000237
C	-2.1868	-0.48921	-2.4E-05
C	2.051734	1.284204	-5.5E-05
H	1.533571	2.240261	-0.00017
C	-4.37389	-0.87737	-5.4E-05
H	-5.23432	-1.53672	-1.6E-05
C	4.132076	-0.03489	0.000151
C	3.297887	-1.2299	0.000233
C	3.42367	1.230653	0.000002
H	4.018502	2.140029	-6.3E-05
C	-4.44469	0.487559	-0.00019
H	3.809557	-2.18913	0.000342
O	5.398271	-0.10663	0.000203
H	-5.3278	1.111953	-0.00027

Table S4. XYZ coordinate of **2**.

	X	Y	Z
S	-1.92718	-0.75867	0.000553
N	0.865392	-0.11952	0.00025
N	0.233159	0.986972	0.000152
N	-1.94511	1.873273	0.00025
C	2.247468	-0.05704	0.000075
C	3.008692	1.140362	-0.00018
H	2.500523	2.097313	-0.00025
C	-1.1367	0.826357	0.000124
C	2.910325	-1.3038	0.000162
H	2.314628	-2.21069	0.000352
C	-3.24251	1.481019	0.000187
H	-4.04271	2.209557	0.000071
C	5.037232	-0.17489	-0.00023
C	4.386771	1.079366	-0.00033
C	4.294716	-1.36851	0.000013
H	4.803887	-2.32716	0.00008
C	-3.43216	0.115199	-1.2E-05
H	4.990514	1.980469	-0.00052
O	6.388072	-0.15458	-0.0004
H	6.754211	-1.05228	-0.00032
N	-4.69027	-0.54648	-0.00032
O	-4.69311	-1.78813	-0.00031
O	-5.7164	0.14938	-0.00048

Table S5. XYZ coordinate of **2**$^{-}$.

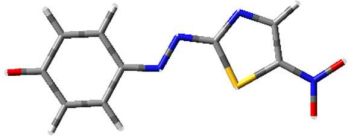

	X	Y	Z
S	1.844549	-0.7534	-0.00033
N	-0.92968	-0.11528	-0.00015
N	-0.27102	1.030173	-0.00018
N	1.910791	1.899072	-0.00012
C	-2.26405	-0.0651	-2.8E-05
C	-3.05796	1.143154	0.000152
H	-2.54439	2.09804	0.000195
C	1.057258	0.85998	-0.00034
C	-2.9479	-1.33374	-0.0001
H	-2.33548	-2.23129	-0.00025
C	3.185495	1.480395	-8.2E-05
H	3.99979	2.194828	0.000078
C	-5.13181	-0.20266	0.000208
C	-4.41665	1.077863	0.00026
C	-4.30819	-1.40816	0.000015
H	-4.82356	-2.36381	-0.00003
C	3.375185	0.104918	-0.0001
H	-5.02418	1.978468	0.000392
O	-6.38537	-0.25188	0.000305
N	4.604708	-0.55015	0.000052
O	4.610753	-1.80468	0.000223
O	5.657518	0.130504	0.000453

Chapter 2

Studies of Photoswitchable agonists for visible-light activation of the Wnt-signaling pathway

Introduction

Pharmacotherapy provides the opportunity to cure diseases and relieve symptoms through the use of medications. It enhances the quality of life and has significantly shaped our world today. However, there are numerous drug-related issues that raise major concerns in society. Pharmacotherapy often faces significant challenges due to poor drug selectivity which can lead to severe side-effects, drug resistance and environmental toxicity. This lack of selectivity arises from the difficulty in controlling the drugs activity in time and space. For example, cytotoxic, anti-neoplastic agents like vinca alkaloids and taxanes are widely used in cancer treatment but are notorious for their severe side effects.[1] These anti-cancer drugs primarily work by disrupting mitosis,[1] which also affects healthy, rapidly dividing cells, leading to adverse events such as hair loss, [2] mucositis,[3] and anemia.[4] Significant efforts have been made to develop targeted therapies[5,6] to mitigate these side effects, yet selectivity remains a significant challenge.[7,8] These negative effects diminish the effectiveness of pharmacotherapy and limit its applicability. To enhance the impact of pharmacotherapy, there is a need to explore and establish new molecular paradigms that improve drug selectivity in real time. Photopharmacology can be a possible solution to such issues. In photopharmacology, photoswitchable groups are incorporated into the molecular structure of bioactive compounds. Light interacts minimally with biochemical systems, i.e., it does not interfere with or cause contamination. [9,10] Photons are either non-toxic or have very low toxicity, making them safer for biological applications. Light can be precisely directed to specific locations (spatial precision) and applied at exact times (temporal precision), which is crucial for accurately controlling the effects of bioactive compounds on biological systems. Additionally, light can be finely tuned in terms of quality (wavelength) and quantity (intensity). By adjusting these parameters, we can control the effects of light on biological processes both qualitatively and

quantitatively. In brief, light provides a highly controlled, non-invasive method for regulating biological activities with minimal side effects.

The concept of photopharmacology involves integrating a photoswitchable unit into the structure of a bioactive compound. This unit can change its configuration when exposed to light, thereby altering the compound's activity. The photoswitchable unit functions like a molecular switch, allowing the drug's activity to be turned on or off in response to specific wavelengths of light. This capability enables dynamic control over the drug's effects, allowing for precise activation or deactivation at desired times and locations within the body. While traditional pharmacotherapy involves administering drugs to treat diseases, photopharmacology adds an extra layer of precision by using light to regulate a drug's function. This approach has significant potential for medical applications since it allows for targeted and timely drug activity. For instance, a photoswitchable drug could be activated only at a tumor site, minimizing damage to healthy tissues. Another key advantage of photopharmacology is its specificity to the selected target. Overall, photopharmacology represents a significant advancement in drug design. It provides dynamic control over drug activity through the use of light, improving the specificity and selectivity of treatments and opening up new possibilities for precise, non-invasive medical applications.

The photoswitchable moiety is a component that changes its structure in response to specific wavelengths of light.[11] This structural change can affect the drug's affinity for its target, allowing the drug to exist in either a high-affinity or low-affinity state based on its design. When in a low-affinity state, the drug is less active, which can help reduce side effects when it is not needed at the target site. Once the drug reaches its target and is exposed to the appropriate light, it switches to a high-affinity state, becoming more active and effective. This external regulation through light allows for precise control over when and where the drug is active.

Criteria for designing of photo-pharmacological drugs

Biological tuning

When incorporating a photoswitchable moiety into the structure of a pharmaceutically active compound, it is essential to retain biological activity in at least one of the photoisomeric states. The design of drugs is often highly optimized to achieve maximum potency and efficacy. [12] However, introducing a photoswitch into such an optimized structure can result in decreased activity. This represents a potential limitation of this method. Therefore, further optimization of the drug's structure is necessary after successfully introducing a photoswitch to regain high potency and efficacy.

Wavelength tuning

Ultraviolet (UV) light can damage biological tissues. Prolonged or intense exposure to UV light may result in DNA damage, cell death, and other harmful effects. [13-16] By adjusting the wavelength to less harmful regions of the spectrum, such as visible or near-infrared light, we can minimize the risk of tissue damage, making them safer for therapeutic applications. Different wavelengths of light penetrate tissues to varying depths. For instance, longer wavelengths, like near-infrared light, penetrate deeper into tissues compared to shorter wavelengths, such as UV light. [17] By tuning the wavelength, we can precisely control how deeply the light penetrates, which is essential for targeting specific tissues or cells.

Effective change in concentration

The change in the concentration of the more active isomer upon irradiation must be significant enough to create a significant difference in the biological response. This means that light exposure should result in a noticeable increase in the active form of the drug, which can effectively interact with its target.

Half-life of *cis*-isomer

Thermal relaxation is when a photoswitchable molecule returns back to its original state after light activation. Controlling this process allows us to regulate drug activity over time. By adjusting the rate of thermal relaxation, we can extend or shorten the duration of drug activity as needed, enabling more precise timing of therapeutic action. However, photoswitches show solvent-dependant changes in half-life and usually shorter in aqueous solvent than in organic solvent. In the case of compounds where the less stable photoisomer is biologically active, one should optimize the light irradiation conditions that allows the compound to exist as photoisomer as the short half-life of photoisomer can directly affect the intended pharmacological action.

Stability in cellular environment

Azobenzenes can undergo degradation in presence of glutathione which is present in cells up to a concentration of 10 mM to respective hydrazines thereby losing its photoswitching ability. [18, 19] Generally, azobenzene-based photopharmaceuticals are stable in reducing cellular environments, at least on the time scale relevant for therapeutic applications, and their stability can be tuned by varying the substitution pattern.

Water Solubility

Photoswitches often show different solubility with their photoisomers. Importantly, many photoswitchable molecules are not soluble in water, however, suitable substitution such as sulfonic acid motif makes them water soluble. From the view point of photopharmacology, the photoswitchable drug must be water-soluble in both its active and inactive isomeric states.

Toxicity

The photoswitchable drug and its photoisomer should not show any toxicity.

Significant progress has been made in understanding the individual factors that determine the requirements for photoswitchable drugs. However, integrating all these factors into a single molecule remains a complex challenge. Each requirement such as effective isomerization, deep tissue penetration, appropriate thermal relaxation, water solubility, metabolic stability, and non-toxicity—must be balanced to create a functional and safe photoswitchable drug. Continued research is essential to unravel the principles underlying these factors. Although photopharmacology is still a relatively new field, it holds immense potential due to the versatility provided by molecular design. The ability to control drug activity with light offers unprecedented precision in therapeutic interventions.

In the past our group and others have achieved photocontrol over various biological systems by incorporating molecular photoswitches into the biologically active small molecules.[20, 21, 22] For instance, photoswitchable substrates and inhibitors of ion channels, in these works researchers have developed light-controlled synthetic ion channels. [23] These channels use a photoisomerizable azobenzene molecule that alters its configuration based on light wavelength. Long-wavelength light enables ion flow by switching the molecule to trans form, while short-wavelength light blocks ion flow by converting it to cis form. Expressed in rat hippocampal neurons, this technology offers a non-invasive way to control neuronal activity which could aid in studying neural circuits and developing neurological treatments. Researchers have also developed an approach called opto-chemical engineering to control G protein-coupled receptors (GPCRs), specifically metabotropic glutamate receptors (mGluRs). [24] This method created light-agonized and light-antagonized mGluRs, which can be activated or inhibited by

specific wavelengths of light. The system was tested in rodent brain slices and zebrafish in vivo, demonstrating its potential for studying synaptic plasticity, memory, and disease.

Our group has developed three non-nucleoside triphosphates, one featuring an azobenzene moiety.[25] This component allows for reversible control of kinesin's motile properties through cis-trans photoisomerization. The triphosphates drive the kinesin-microtubule system with significant activity, achieving nearly half the velocity of ATP. This approach enables precise speed control of kinesin-driven transport, useful for studying intracellular mechanisms and developing targeted therapies. We also developed an azobenzene-based inhibitor that targets CENP-E, a kinesin vital for chromosome transport.[26] This inhibitor allows reversible switching of CENP-E activity using UV and visible light cycles, demonstrating the potential of photochemical techniques for studying cellular processes and developing targeted cancer therapies. Our group have developed a ROCK inhibitor based on a phenylazothiazole scaffold that can be controlled by visible light via reversible trans-cis isomerization. [27] This method allows precise regulation of ROCK activity, which is essential for processes like cytoskeletal formation, cell migration, and apoptosis. Recently our group, developed a system that uses light to control the degradation of target proteins. [28] This system is based on the auxin-inducible degron (AID) technology, which allows for conditional protein degradation. The system enables spatiotemporal control of protein degradation. This technology has potential applications in studying protein function, investigating disease mechanisms, and developing targeted therapies.

Photocontrol of cellular signalling is relatively less investigated. In one previous study, Trauner and coworkers have created photoswitchable fatty acid analogues (FAAzos) that incorporate an azobenzene photoswitch. [29] By modifying these FAAzos to mimic capsaicin, they developed photolipids targeting TRPV1, a channel involved in pain sensation. The FAAzos are inactive in the dark but become active under ultraviolet light and can be deactivated by blue light. This

allows for precise control of TRPV1 activity, aiding in the study of pain pathways and the development of new pain treatments. Recently, our group has developed photocontrol of TGF-β signaling pathway, the dysregulation of which is linked to several human diseases, including cancer by using caging bioactive triarylimidazole-based drug molecules.[30] This method adds a dialkylamino group to the carbon atom of the imidazole ring, transforming its structure from planar imidazole to tetrahedral 2H-imidazole, allowing for selective uncaging upon exposure to visible light.

In this chapter, I report photocontrol of new signaling target, Wnt signaling pathway, an important pathway in many biological processes such as gene regulation, embryonic development, and progression of cancer. [31-33]

The name "Wnt" comes from a combination of "Wingless" (Wg), identified in Drosophila, and "Int-1," found in mice, reflecting the discovery of the pathway in these two organisms. [2] Because of the similarities in the functions of the Wingless and Int-1 genes, researchers combined their names to form "Wnt," which stands for Wingless-related integration site. This name reflects the pathway's dual roles in development and cancer. The Wnt/β-catenin pathway is highly conserved across various species, meaning it performs similar functions in many different organisms.[3] Dysregulation of the Wnt/β-catenin pathway has been implicated in several diseases, including cancer, type II diabetes, and other developmental disorders.[4]

In the canonical Wnt signaling pathway, the binding of Wnt ligands to Frizzled receptors on the cell surface leads to the stabilization and accumulation of β-catenin in the cytoplasm. This β-catenin then moves to the nucleus, where it interacts with T-cell factor (TCF) transcription factors to regulate the expression of Wnt target genes. Small molecule agonists or antagonists can also regulate the pathway.[5-6] For instance, BML-284, a 2-amino-4,6-disubstituted pyrimidine, is a cell permeable Wnt signaling agonist that functioned both in cell culture and

Xenopus model.[5] It is a small molecule that can activate Wnt signaling pathway in a dose-dependent manner. In experiments with Xenopus tadpoles, treatment with this molecule leads to significant head defects, indicating its potent effect on Wnt signaling.[5]

In signal transduction, the location and duration of protein phosphorylation within the cell are crucial for effective signaling. Different cellular compartments contain unique proteins and signaling molecules, leading to distinct downstream responses. For example, phosphorylation at the cell membrane triggers different pathways than phosphorylation in the nucleus. The duration of phosphorylation matters as well, prolonged phosphorylation results in sustained signaling, while transient phosphorylation leads to short-lived responses. This timing affects the strength and nature of cellular outcomes. Phosphorylation can activate or deactivate proteins, modulating their functions and interactions. This regulation ensures accurate signal propagation, allowing cells to fine-tune their reactions to stimuli and maintain proper cellular function.[7] So, spatiotemporal regulation of such signaling pathways is very important. Optical control of signal transduction is one way to achieve high spatiotemporal resolution. Previously, the optical control of the Wnt signaling pathway that involves light-inducible protein-protein interactions has been reported. [13,14] Controlling the Wnt signaling pathway using an optogenetic approach can be more complex than utilizing a small molecule-based method, which does not require genetic modifications. I aimed to develop a small molecule-based photoswitchable agonist for the optical control of Wnt signaling pathway based on a well-known Wnt agonist BML-284. For photocontrolling of the Wnt signaling pathway I developed photoswitchable azo derivatives that act as the Wnt agonist in one (cis) of the photoisomers and remains inactive in the other photoisomer (trans). The results showed that cis-**2** functioned as relatively good agonist for the Wnt signaling pathway. The biologically active form of BML-284 was found to be a bent structure with the 1,2 methylenedioxybenzene motif nearly perpendicular to the plane of aminopyrimidine motif in the host protein T2R-TTL. Due to this bent structure expected

only in the respective cis forms of compounds **1** and **2**, these cis forms and not the trans ones were considered to likely be active as Wnt agonists. Our results showed cis-2 functioning as a relatively good agonist for the Wnt signaling pathway.

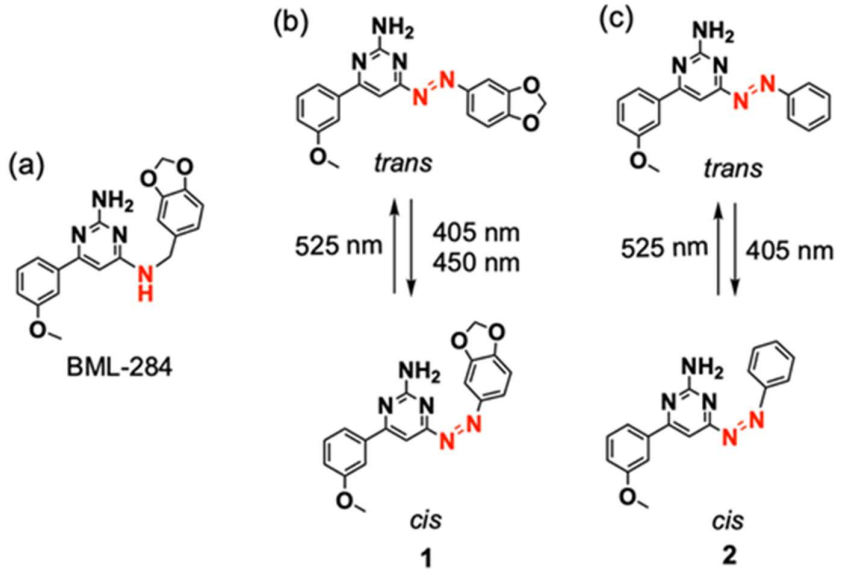

Figure 1. Molecular structures of a non-photoswitchable Wnt agonist **BML-284** and photoswitchable Wnt agonists **1** and **2** along with their reversible *trans* – *cis* isomerization by visible lights (405 nm, 450 nm, or 525 nm).

Experimental Section

Experimental and instrumentation methods

All reagents and solvents were purchased from commercial sources (FUJIFILM Wako Pure Chemical Corporation, Tokyo Chemical Industry, Merck, Kanto Chemical) and used without further purification. Reactions were monitored by thin-layer chromatography using TLC silica gel 60 F_{254} (Merck). Column chromatography was performed using silica gel 60 N (spherical, neutral, 63-210 μm, Kanto chemical). NMR spectra (^{1}H, ^{13}C) were measured by a JEOL ECX-400 (400 MHz) spectrometer. A Shimadzu UV spectrophotometer (UV-1800) equipped with a TCC-100 Shimadzu temperature-controlled cell holder was used for UV-vis

spectrophotometry. Photoisomerization studies were carried out using a LED light source (Asahi Spectra, CL-1503) with LED heads emitting at 405 nm, 450 nm, 525 nm. For biological studies, 450 nm light of intensity 7.94 mW/cm^2 (compound 1) and 405 nm light of intensity 0.05 mW/cm^2 (compound 2) were used. The stability in presence of glutathione for compound **1** and **2** and photodegradation studies of compound **1** were acquired using an Agilent 8453 spectrophotometer under continuous irradiation at specific wavelengths.

Cell culture

HEK293T cells were obtained from American Type Culture Collection and maintained in DMEM supplemented with 10% FBS, 2 mM glutamine, and antibiotics (100 U/ml of Penicillin-Streptomycin). Transfection of plasmids was performed with PEI Max transfection reagent (Polysciences) according to the manufacturer's protocol. For the measurement of beta-catenin/TCF transcriptional activity, 293T cells were transfected with the Wnt reporter (TOPFlash) and the control reporter (pRL-TK) (Promega) plasmids, and cultured for 24 hours. 24 hours after transfection, cells were treated with test compounds or DMSO and cultured for another 24 hours with or without irradiation of the indicated wavelength of light. Luciferase and Renilla luciferase activity in cell lysates was measured by using the Dual-Glo luciferase assay system in the GloMax Explorer system (Promega). We normalized the relative luciferase activity expressed from the Wnt reporter plasmid to the activity of Renilla luciferase expressed from the pRL-TK plasmid.

Results and Discussion

Synthesis and NMR Spectra

Scheme S1. Synthetic scheme

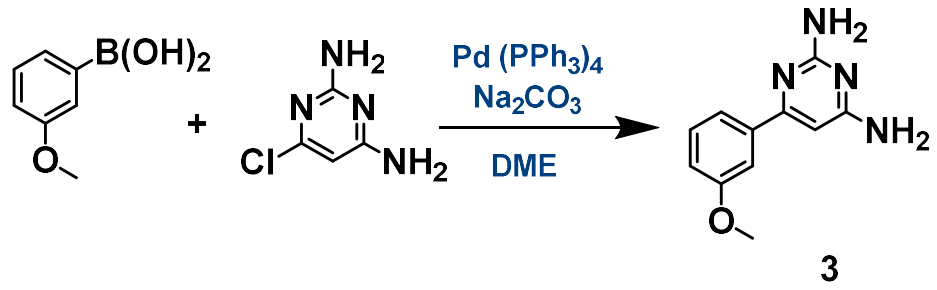

Synthetic scheme for compound **3**.

A 1,2-dimethoxyethane solution (30 mL) of 6-chloropyrimidine-2,4-diamine (1.95 g, 0.0134 mol), tetrakis(triphenylphosphine)palladium (0.44 g, 0.0038 mol) was prepared, and then 3-methoxyphenylboronic acid (2.77 g, 0.0201 mol) was added immediately, followed by the addition of a 2M Na_2CO_3 solution (14 mL). The reaction mixture was flushed with N_2 gas for 5 minutes and then maintained at 95 °C under inert conditions for 48 hours. The precipitate was washed with THF and sonicated for 10 minutes. The solvent was removed by vacuum evaporation, and the compound was extracted with ethyl acetate, dried with $MgSO_4$, and then subjected to vacuum evaporation again. The product was purified by column chromatography on silica using an eluent of 90% EtOAc and hexane, yielding pure compound 67% yield.

^{1}H NMR (400 MHz, DMSO-d_6) δ 7.45-7.42 (m, 2H), 7.34 (t, 1H), 7.00-6.97 (m, 1H), 6.33 (s, 2H), 6.19 (s, 1H), 5.94 (s, 2H), 3.79 (s, 3H)

^{13}C NMR (600 MHz, DMSO-d_6) δ 165.71, 164.15, 162.50, 159.88, 140.453, 129.94, 119.0, 115.71, 111.97, 91.27, 55.6,

ESI MS. m/z $[M+H]^+$ calculated for $C_{11}H_{12}N_4O$: 216.10111, found 217.10815 (**Figure S6**).

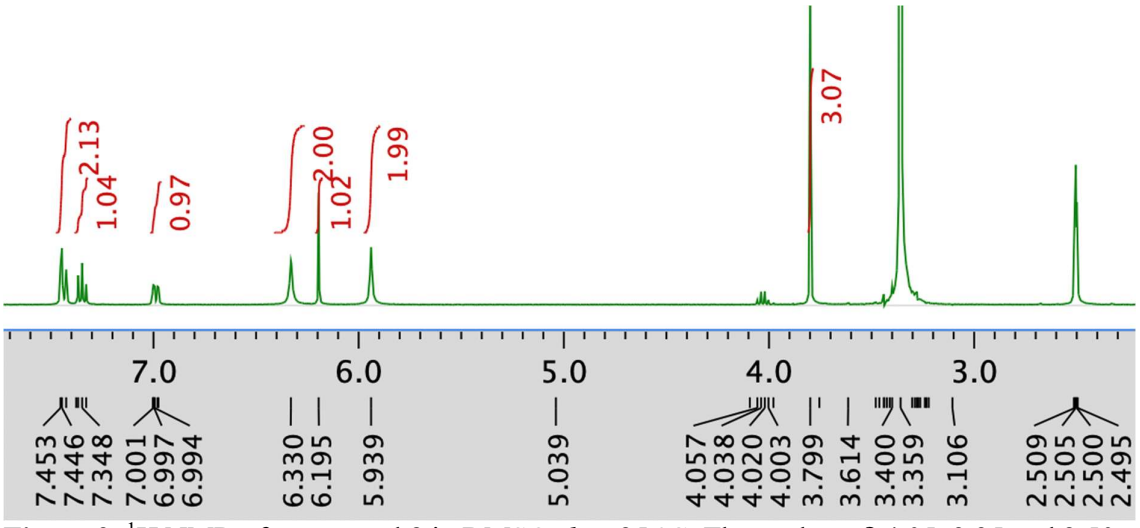

Figure 2. ^{1}H NMR of compound **3** in DMSO-d_6 at 25 °C. The peaks at δ 4.05, 3.35 and 2.50 are from solvents.

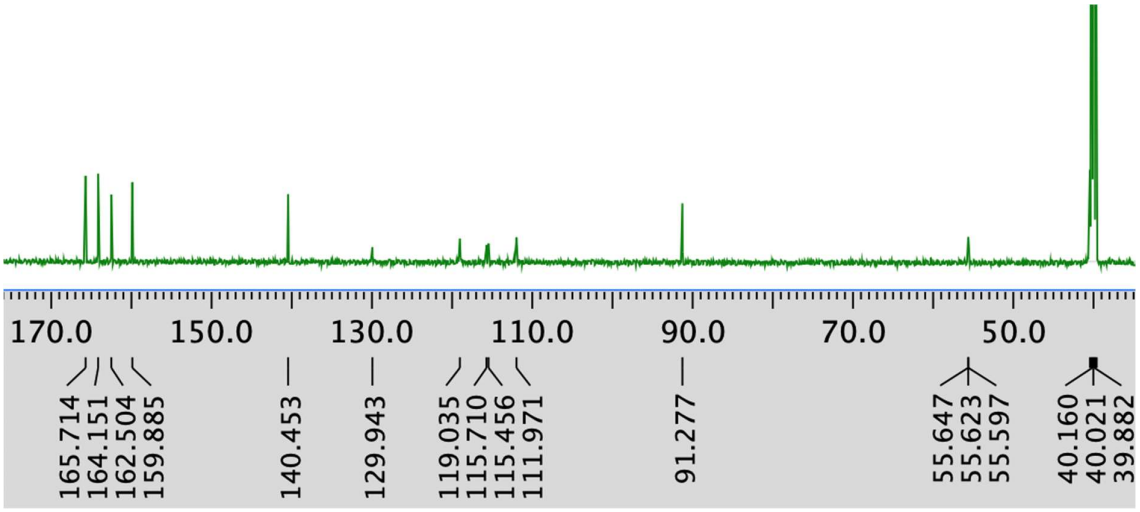

Figure 3. ^{13}C NMR of compound **3** in DMSO-d_6 at 25 °C. The peaks at δ 40.02 is from the solvents.

Synthetic scheme of Compound **4**

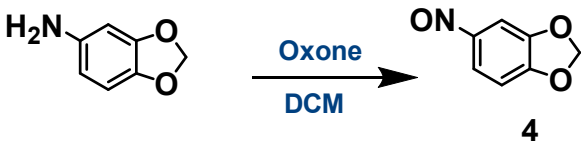

4

To a solution of 3,4 methylenedioxyphenyl amine (5.0 g, 0.0364 mol) in DCM (250 mL) under vigorous stirring, an aqueous solution (250 mL) of oxone (44.75 g, 0.072 mol) was added dropwise at room temperature and stirred vigorously for 1 hour. The compound was extracted with ethyl acetate, dried with $MgSO_4$, solvent removed by vacuum evaporation, and subjected to column chromatography on silica using the EtOAc (30%)/Hexane eluent to isolate pure compound (6% yield).

^{1}H NMR (400 MHz, CH_3OH-d_4) δ 8.60 (d,1H), 7.25 (d,1H), δ 6.39 (s, 1H), 6.15 (s, 2H)

^{13}C NMR (600 MHz, acetonitrile-d_3) δ 165.41, 154.87, 149.78, 108.24, 103.64.

ESI MS. m/z $[M+H]^+$ calculated for $C_7H_5NO_3$: 152.02694, found 152.03423. (**Figure S7**)

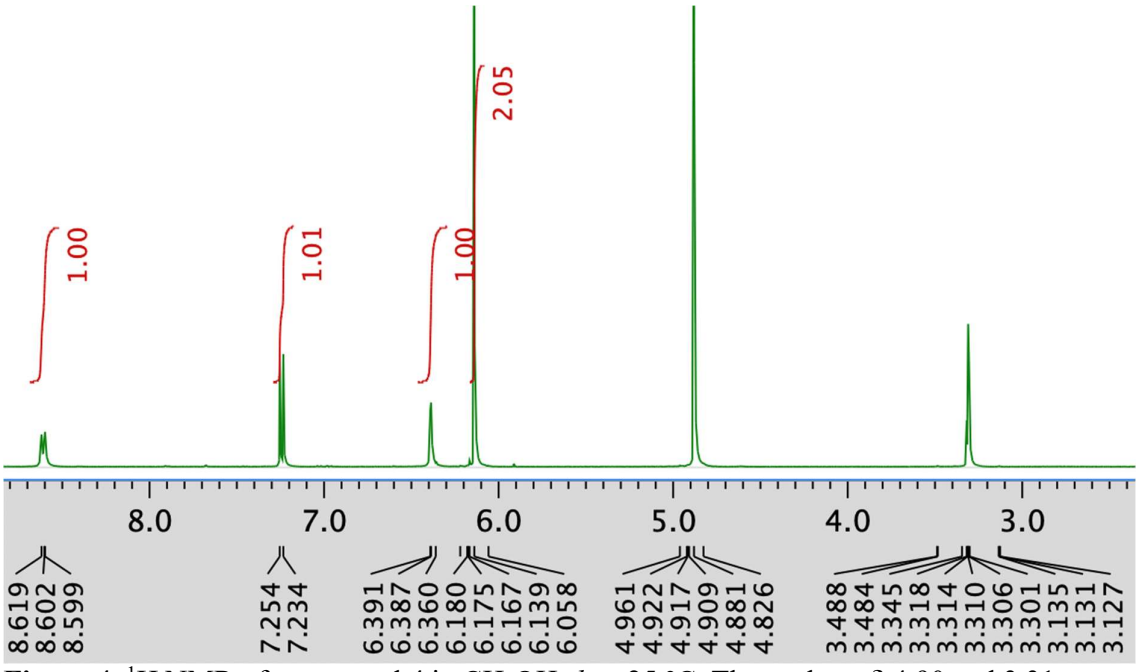

Figure 4. ^{1}H NMR of compound **4** in CH_3OH-d_4 at 25 °C. The peaks at δ 4.90 and 3.31 are from the solvents.

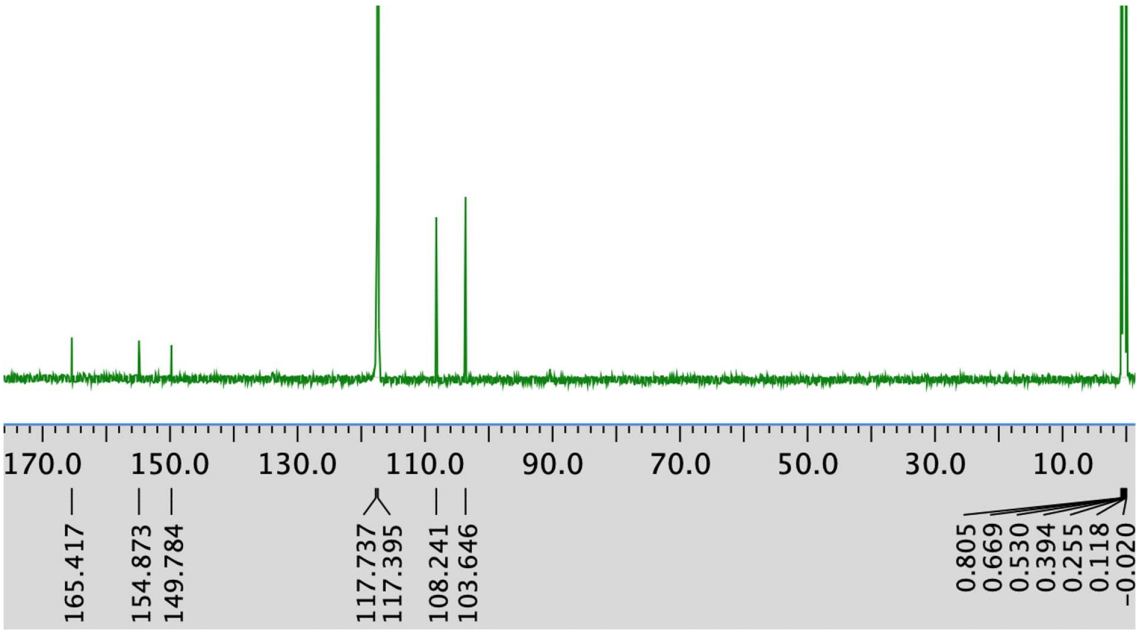

Figure 5. ^{13}C NMR of compound **4** in acetonitrile-d_3 at 25 °C. The peaks at δ 117.39 and 0.25 are from the solvents.

Scheme S3. Synthetic scheme for compound **1**.

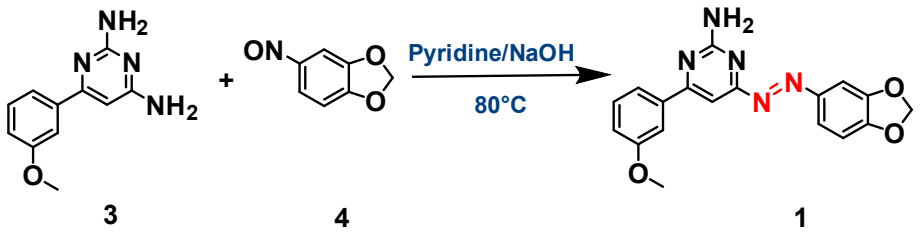

To a mixture of diamino methoxyphenyl pyrimidine (0.4 g, 1.1 eq.) and pyridine (2.4 mL) kept at 80 °C, a nitroso derivative (0.4 g, 1.0 eq.) was added. Then, 40% NaOH (100 μL) was added and stirred at 80 °C for 1 hour. Then, the solvent was removed by vacuum evaporation, and subjected to column chromatography on silica using the EtOAc (30%)/Hexane eluent to isolate pure compound (3% yield).

^{1}H NMR (400 MHz, CD_3OD-d_4) δ 7.80-7.78 (dd, 1H), 7.72-7.67 (m, 2H), 7.47 (d,1H), 7.44-7.40 (t, 1H), 7.35 (s, 1H), 7.11-7.07 (m, 2H), 6.14 (s, 2H), 3.89 (s, 3H).

^{13}C NMR (600 MHz, $CDCl_3$) δ 168.14, 163.85, 160.02, 152.38, 149.14, 148.32, 138.75, 129.87, 127.05, 119.69, 116.93, 112.33, 108.21, 102.41, 98.82, 97.63, 55.54.

ESI MS. m/z $[M+H]^+$ calculated for $C_{18}H_{15}N_5O_3$: 350.11749, found 350.12398. (**Figure S11**)

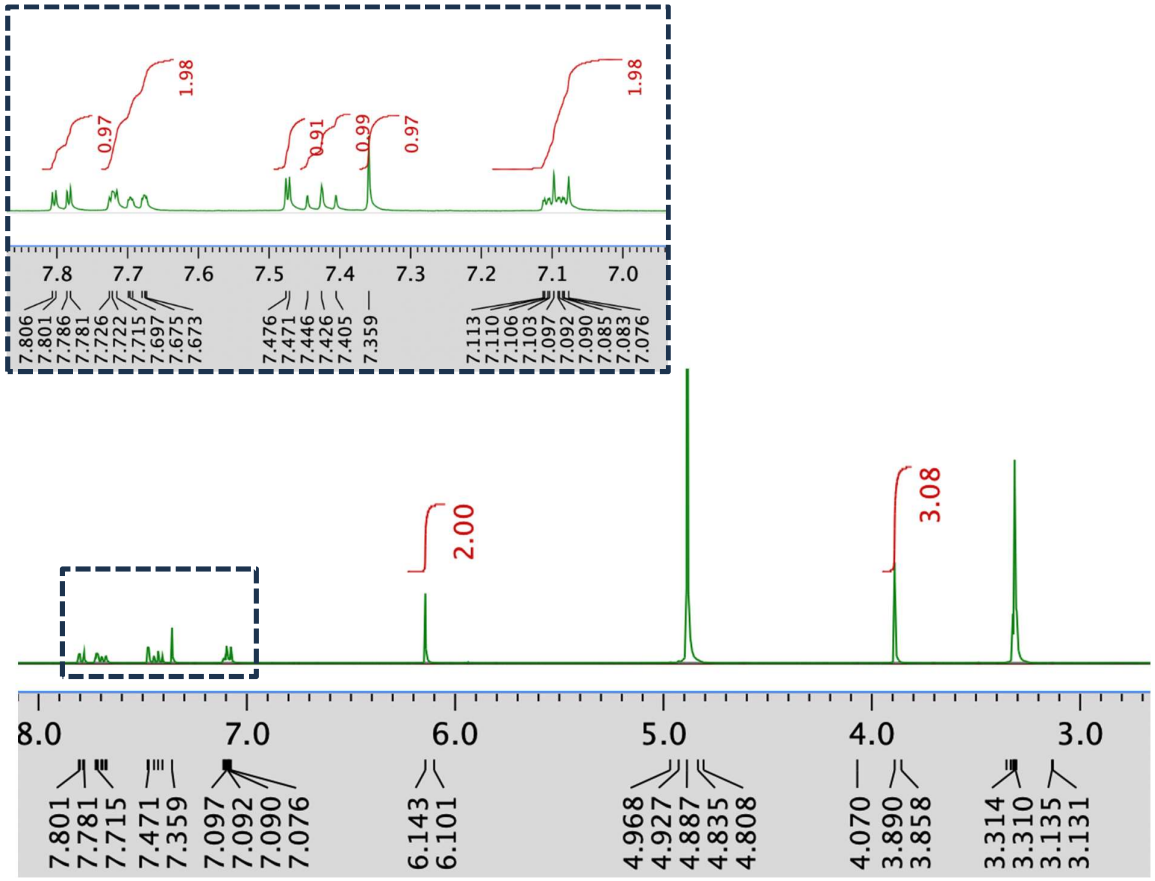

Figure 6a. ^{1}H NMR of compound **1 in** CD_3OD-d_4 (top) at 25 °C. The peaks at δ 4.87 and 3.31 are from the solvents.

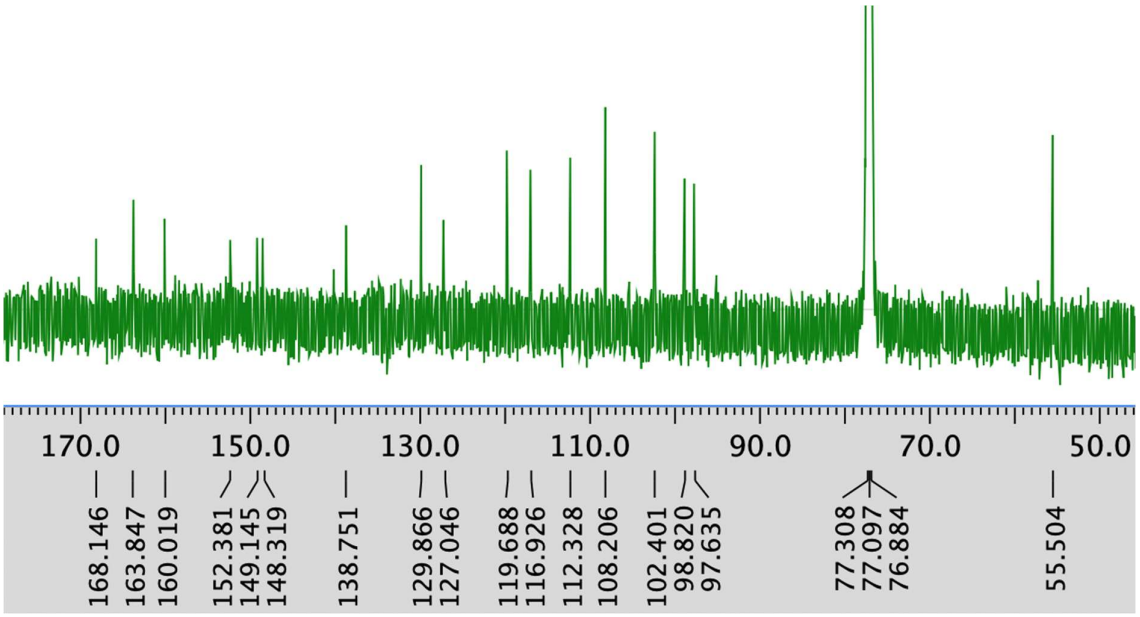

Figure 6b. ^{13}C NMR of compound **1 in** $CDCl_3$ at 25 °C. The peak at δ 77.10 is from the solvents.

Scheme S4. Synthetic scheme for compound **2**.

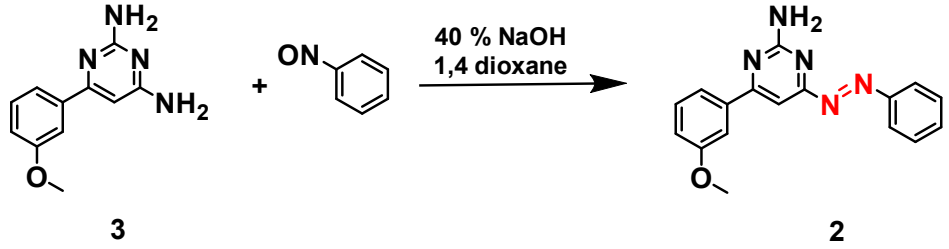

To a mixture of diamino methoxyphenyl pyrimidine (0.67 g, 1.1 eq.) and 1,4-dioxane (1 mL), nitrosobenzene (0.3 g, 1.0 eq.) was added. Then, 40% NaOH (5 mL) was added and stirred at room temperature for 30 minutes. The solvent was removed by vacuum evaporation, added water, extracted with ethyl acetate, dried with $MgSO_4$. The solvent was again removed by vacuum evaporation, and subjected to column chromatography on silica using the EtOAc (30%)/Hexane eluent to isolate pure compound (8% yield).

^{1}H NMR (400 MHz, CH_3CN-d_3) δ7.99-7.97 (d, 1H), δ7.97-7.95 (m, 1H), δ7.71-7.69 (m, 1H), δ7.69-7.68 (m, 1H), δ7.63-7.61 (m, 1H), δ7.61-7.58 (m, 1H), δ7.44-7.39 (t, 1H), δ7.31 (s, 1H), δ7.09- 7.05 (dd, 1H) δ5.75 (s, 2H), δ3.85 (s, 3H)

^{13}C NMR (600 MHz, acetonitrile-d_3) δ 171.25, 167.41, 164.30, 160.19, 152.31, 138.62, 133.09, 129.96, 129.65, 123.39, 119.42, 116.64, 112.27, 95.60, 55.14

ESI MS. m/z $[M+H]^+$ calculated for $C_{17}H_{15}N_5O$: 306.12766, found 306.13426. (**Figure S12**)

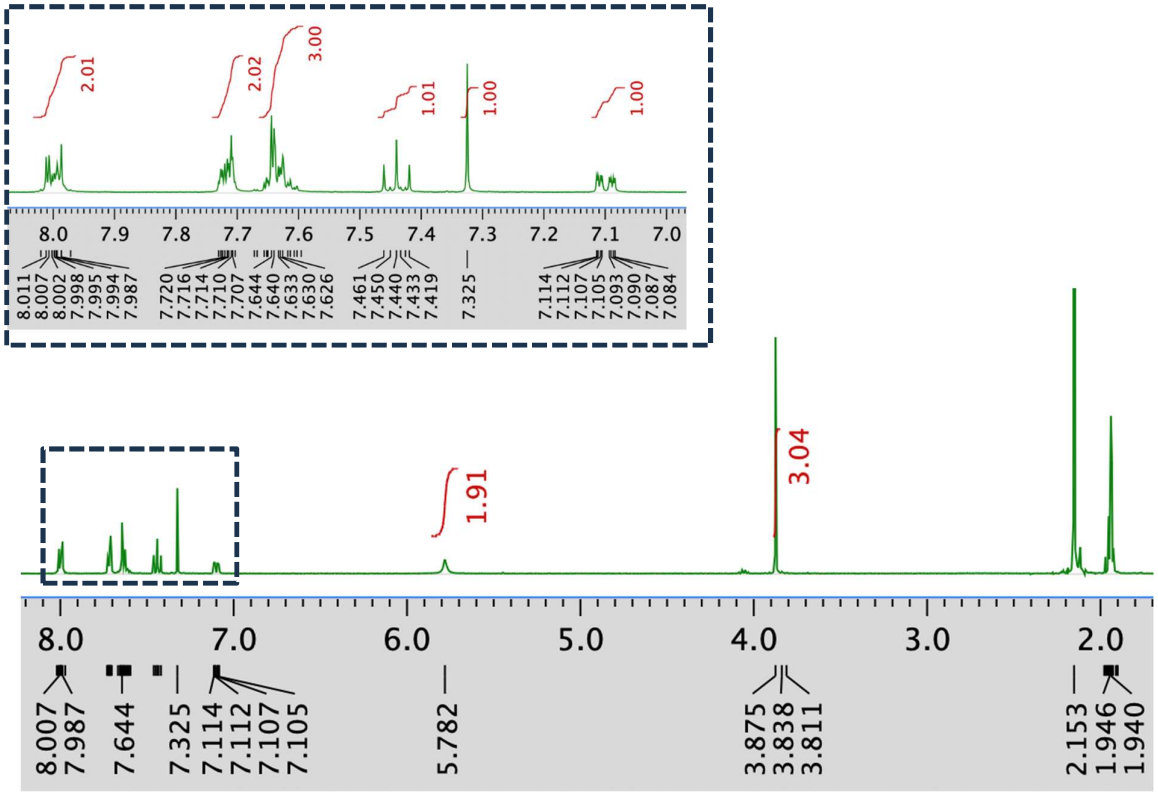

Figure 7a. ^{1}H NMR in CD_3CN-d_3 (top) (solvent peak at δ 1.97) and ^{13}C NMR (bottom) in CD_3CN-d_3 (solvent peak at δ 117.40) of **2** at 25 °C.

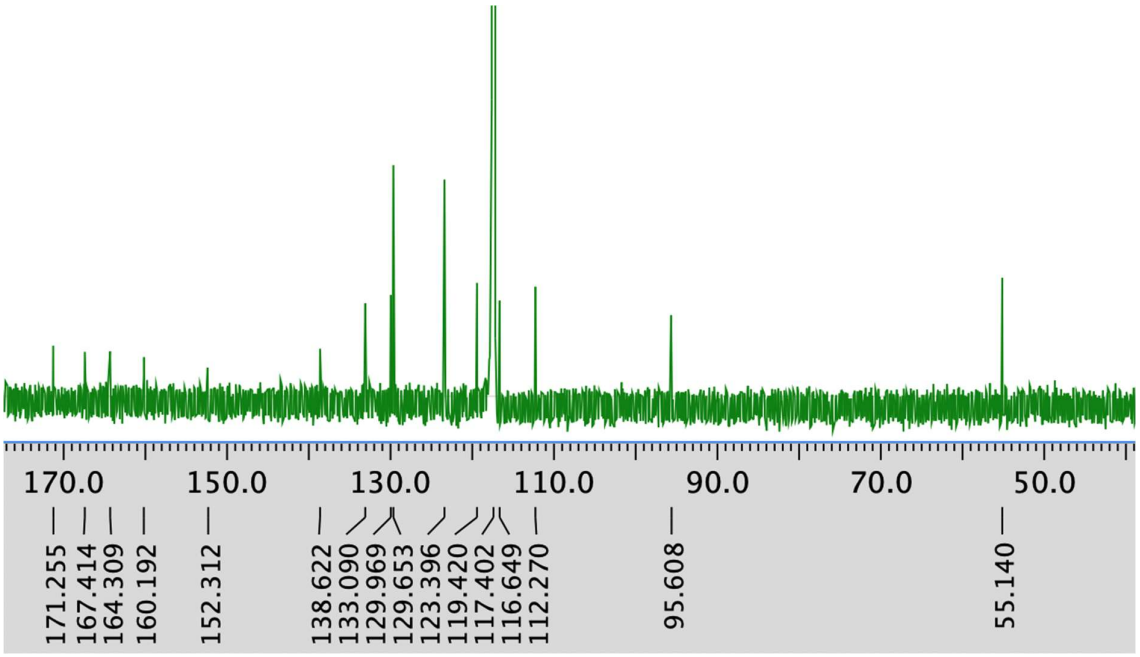

Figure 7b. ^{13}C NMR of compound **2** in CD_3CN-d_3 (solvent peak at δ 117.40) at 25 °C.

Measurement of isomer conversion for compound 2

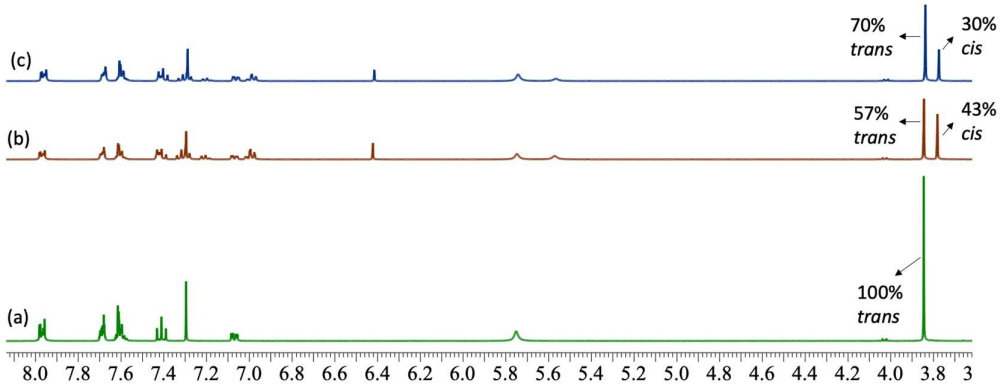

Figure 8a. ^{1}H NMR of compound **2** (a) before irradiation (b) after 405 nm irradiation at PSS_{405} (c) after 525 nm irradiation PSS_{525}. Before irradiation, the NMR spectra did not show any peaks from the cis isomer.

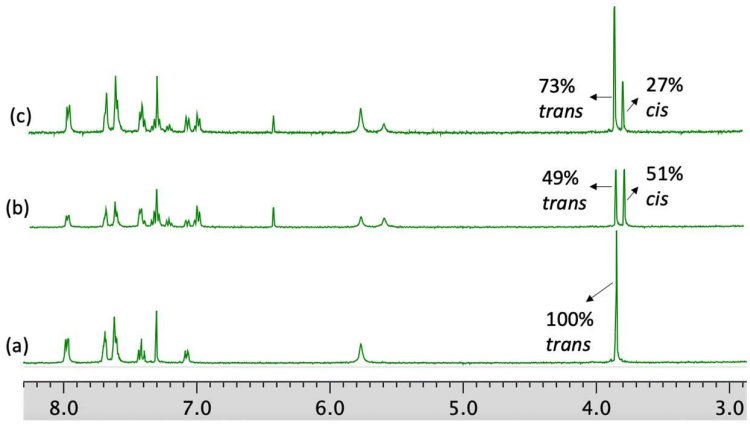

Figure 8b. ^{1}H NMR of compound 2 (a) before irradiation (b) after 365 nm irradiation at PSS_{365} (c) after 525 nm irradiation PSS_{525}. Before irradiation, the NMR spectra did not show any peaks from the cis isomer.

Mass spectra of Compounds

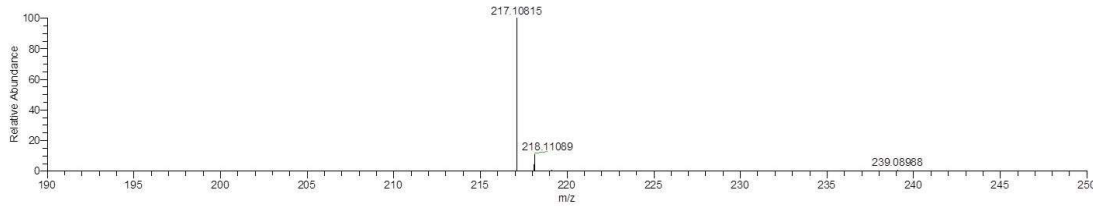

Figure 9. ESI MS spectrum of compound **3**. m/z $[M+H]^+$ calculated for $C_{11}H_{12}N_4O$: 217.10111, found 217.10815.

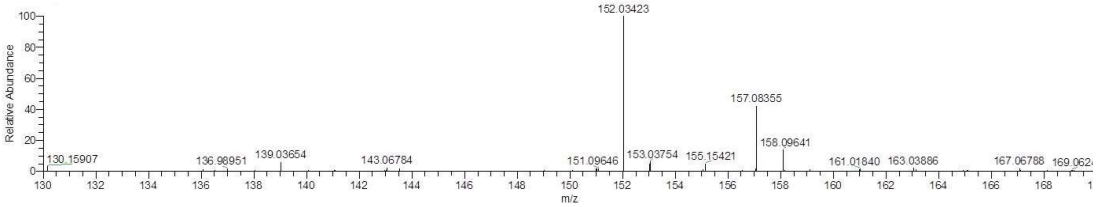

Figure 10. ESI MS spectrum of compound **4**. m/z $[M+H]^+$ calculated for $C_7H_5NO_3$: 152.02694, found 152.03423.

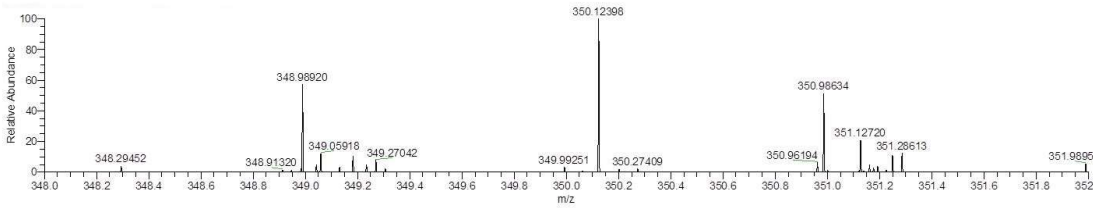

Figure 11. ESI MS spectrum of compound **1**. m/z $[M+H]^+$ calculated for $C_{18}H_{15}N_5O_3$: 350.11749, found 350.12398.

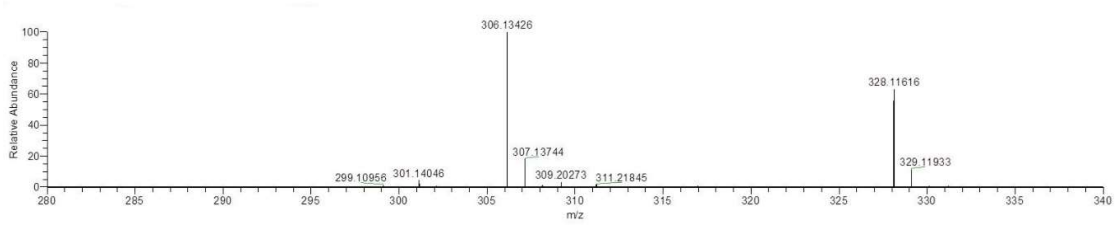

Figure 12. ESI MS spectrum of compound **2**. m/z $[M+H]^+$ calculated for $C_{17}H_{15}N_5O$: 306.12766, found 306.13426.

Measurement of isomer conversion for compound 1

Due to short half-life of compound **1** (6.4 min at 25 °C), the isomer ratios at PSS obtained by NMR analysis were inaccurate and hence used the absorption spectroscopy for isomer ratios calculation at PSS. When the extinction coefficient of Z isomer of compound **1** (εZ) at λ_{max} (380 nm) was zero, then the isomer ratios at PSS was calculated using the equation:

$$X_E = \frac{A0}{\text{Abs at PSS}}$$

X_E = E isomer ratio at PSS

A_0 = Absorbance at initial state at λ_{max}

Abs at PSS = Absorbance at PSS at λ_{max}

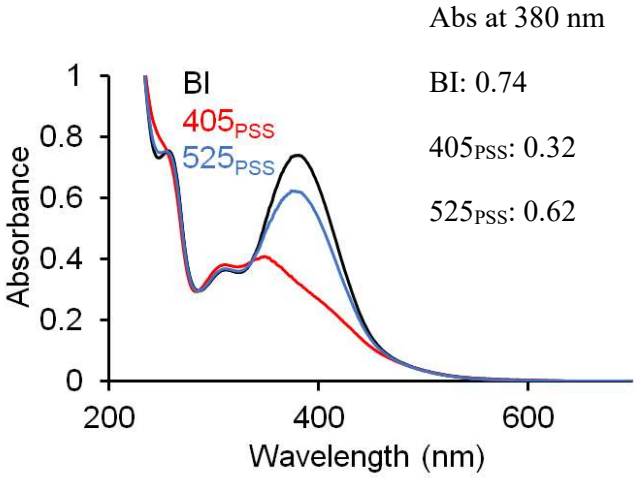

Figure 13. Absorption spectra of **1** in CH_3CN before (BI) and after irradiations at PSS of 405 nm (405_{PSS}) and 525 nm (525_{PSS}) at 25 °C. Calculated isomer ratios were 43:57 (E: Z) at 405_{PSS} and 84:16 (E: Z) at 525_{PSS}

Photophysical studies

The photophysical properties of compounds **1** and **2** were examined using UV-vis absorption spectroscopy in both organic and aqueous solutions. The absorption spectra of **1** and **2** displayed significant changes, as illustrated in the figures. The absorption spectrum of 1 (100 % trans isomer) without light irradiation exhibited π - π* transition band around 380 nm, which was red-shifted by 45 nm compared with azobenzene (Figure 15, black curve). The red-shifted absorption allowed us to use visible light for its isomerisation to cis form. Upon light illumination at 405 nm, it reached a photostationary state ($PSS_{405\ nm}$), where the cis isomer was predominantly formed (Figure 14, red curve). Irradiation with 525 nm light, it reached a photostationary state ($PSS_{525\ nm}$), where the trans isomer was predominantly formed (Figure 14, blue curve).

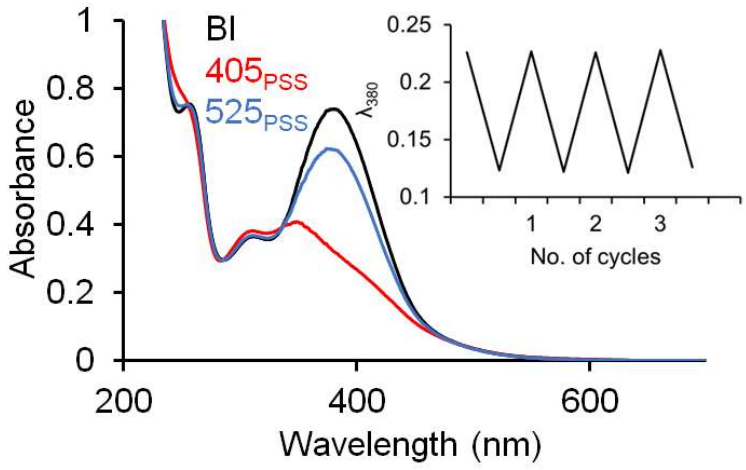

Figure 14. Absorption spectra of **1** in acetonitrile at 25°C before irradiation (BI, black lines) and the PSS of 405 nm irradiation (405_{PSS}, red lines) and the PSS of 525 nm (525_{PSS}, blue lines) (absorbance changes for repeated 405_{PSS} and 525_{PSS} are shown in insets)

Similarly, compound **2** isomerized by 405 nm light irradiation to form cis (Figure 15 red curve) and back isomerized by 525 nm light irradiation to form trans isomer (Figure 15 blue curve).

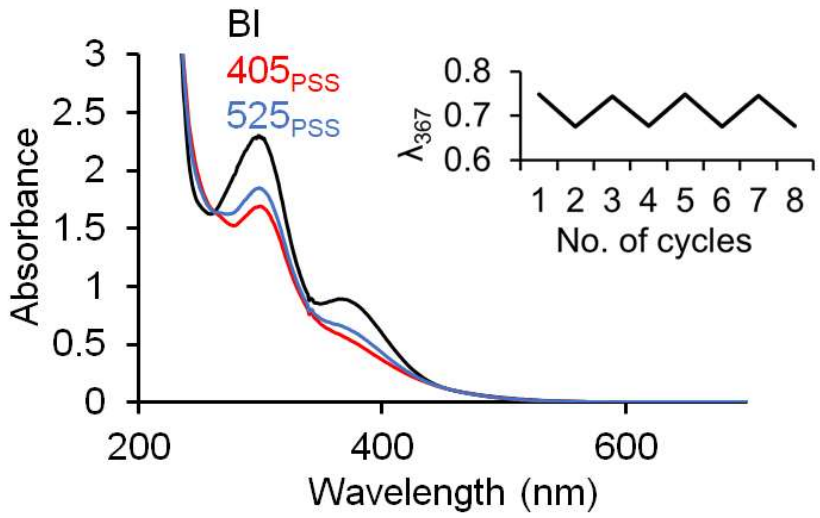

Figure 15. Absorption spectra of **2** in acetonitrile at 25°C before irradiation (BI, black lines) and the PSS of 405 nm irradiation (405_{PSS}, red lines) and the PSS of 525 nm (525_{PSS}, blue lines) (absorbance changes for repeated 405_{PSS} and 525_{PSS} are shown in insets)

Photoisomerization and thermal back isomerization

The absorption spectra of the *cis* and *trans* isomers of **1** and **2** were recorded with a diluted solution of compounds in acetonitrile (in micromolar concentration). The *cis* isomers were obtained with 405 nm and 450 nm LED light irradiation. The *cis*→ *trans* back isomerization was performed with a 525 nm LED light irradiation. The *trans*→ *cis* and *cis*→ *trans* photoisomerization was repeated for several cycle by using 405 nm and 525 nm light irradiation.

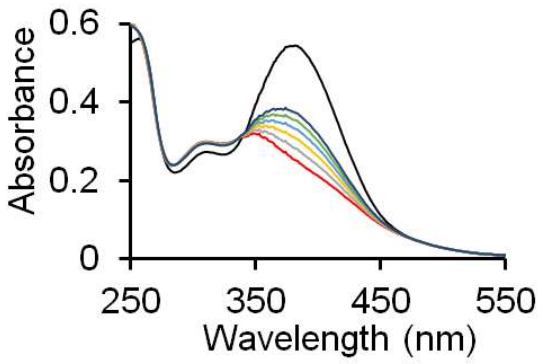

Figure 16. Thermal back isomerization of **1** in acetonitrile at 25 °C before irradiation (BI, black lines) and absorbance at 405 nm irradiation (405_{PSS}, red lines) and absorbance at 405 nm irradiation at time interval of 60 sec after keeping in dark (other lines).

Half -life of cis isomer of 1 and 2

A freshly prepared solution was irradiated at 405_{PSS} and immediately kept for thermal back Z–E isomerization in dark at temperatures. For compound **1** and **2**, spectra at fixed time intervals were recorded in dark condition to minimize the effect of light beam on thermal back isomerization. Then, a first order rate constant (k) for the thermal back Z–E isomerization reaction was obtained using the equation:

$$ln\frac{At}{Ao} = ln\frac{Abs(BI)-Ab\ (time)}{Abs(BI)-Abs(PSS)} = -kt$$

Abs(BI) = absorbance at initial state at λ_{max}.

Abs(PSS) = absorbance at photostationary state at λ_{max}.

Abs(time) = absorbance at λ_{max} at different time interval for thermal back isomerization from 405_{PSS}.

For a first order reaction, half-life ($t_{1/2}$) can be calculated using the equation:

$$t1/2 = \frac{0.693}{k}$$

The lifetime of cis isomer of **1** in acetonitrile at 25°C was found to be 6.4 minutes (figure 17).

In aqueous medium at 37°C the lifetime was 3 seconds (figure 22).

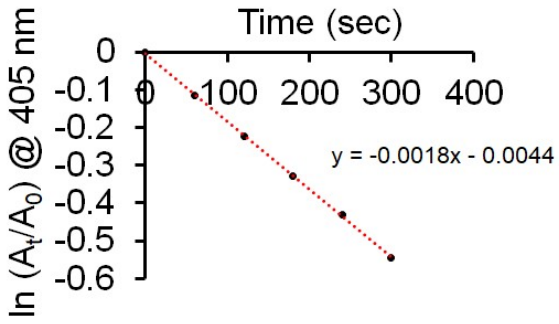

Figure 17. Thermal half-life of **1** in acetonitrile at 25 °C; $t_{1/2}$ = 6.4 min.

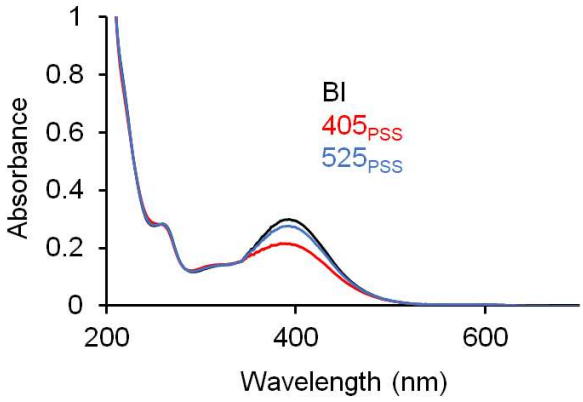

Figure 18. Absorption spectra of **1** in water at 25 °C before irradiation (BI, black lines) and the PSS of 405 nm irradiation (405_{PSS}, red lines) and the PSS of 525 nm irradiation (525_{PSS}, blue lines).

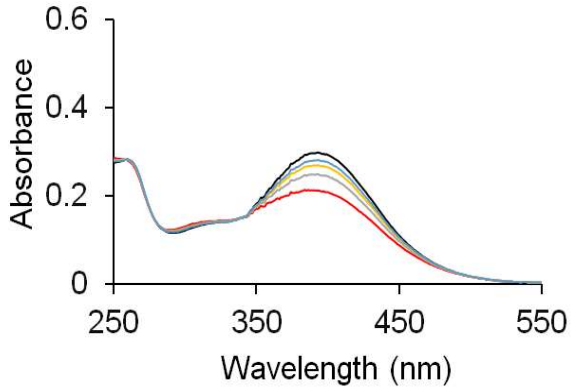

Figure 19. Thermal back isomerization of **1** in water at 25 °C before irradiation (BI, black lines) and absorbance at 405 nm irradiation (405_{PSS}, red lines) and absorbance at 405 nm irradiation at time interval of 30 sec after keeping in dark (other lines).

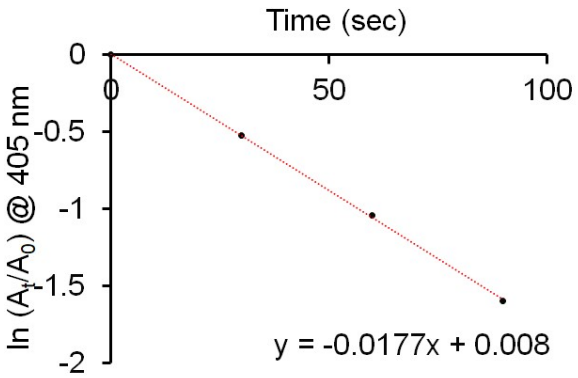

Figure 20. Thermal half-life of **1** in water at 25 °C; $t_{1/2}$ = 39 seconds.

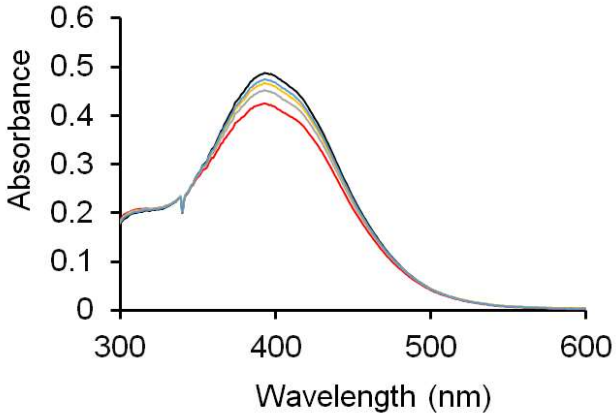

Figure 21. Thermal back isomerization of **1** in aqueous culture medium at 37 °C before irradiation (BI, black lines) and absorbance at 405 nm irradiation (405_{PSS}, red lines) and absorbance at 405 nm irradiation at time interval of 2 sec after keeping in dark (other lines).

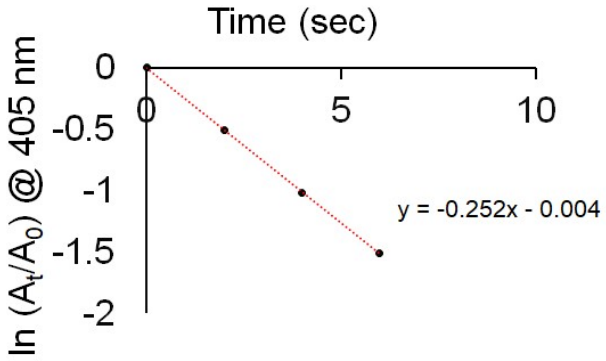

Figure 22. Thermal half-life of **1** in aqueous medium at 37 °C; $t_{1/2}$ = 3 seconds.

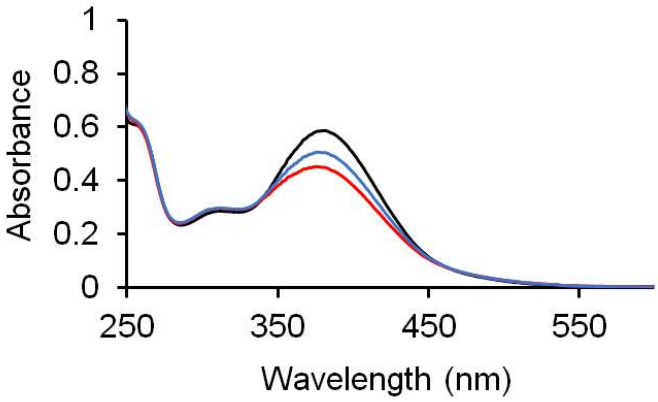

Figure 23. Absorption spectra of **1** in acetonitrile at 25 °C before irradiation (BI, black lines) and the PSS of 450 nm irradiation (450_{PSS}, red lines) and the PSS of 525 nm irradiation (525_{PSS}, blue lines).

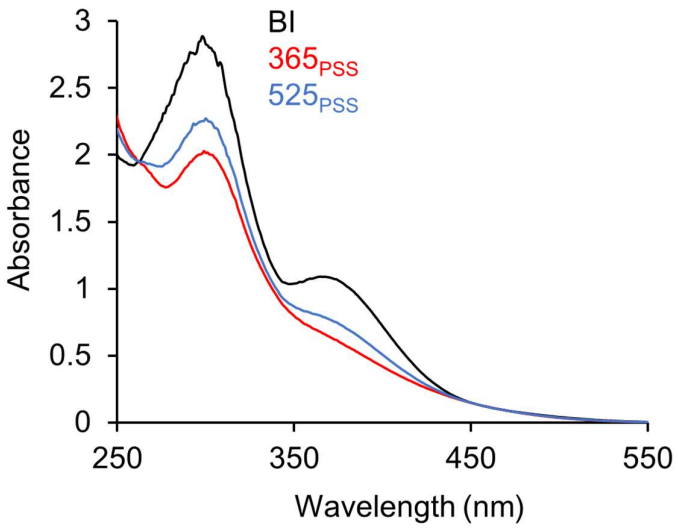

Figure 24. Absorption spectra of **2** in acetonitrile at 25 °C before irradiation (BI, black lines) and the PSS of 365 nm irradiation (365_{PSS}, red lines) and the PSS of 525 nm irradiation (525_{PSS}, blue lines). Calculated (from NMR; Figure S7b) isomer ratios were 49:51 (E: Z) at 365_{PSS} and 73:27 (E: Z) at 525_{PSS}.

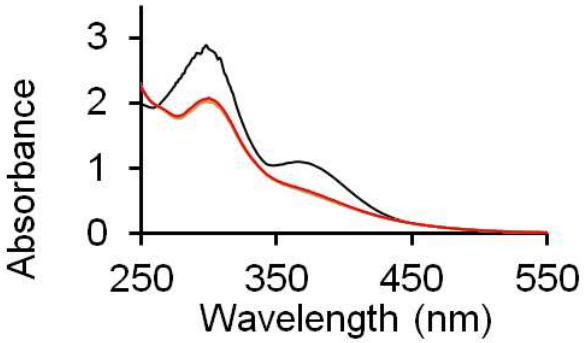

Figure 25. Thermal back isomerization of **2** in acetonitrile at 25 °C before irradiation (BI, black lines) and absorbance at 405 nm irradiation (405_{PSS}, red lines) and absorbance at 405 nm irradiation at time interval of 60 sec after keeping in dark (other lines).

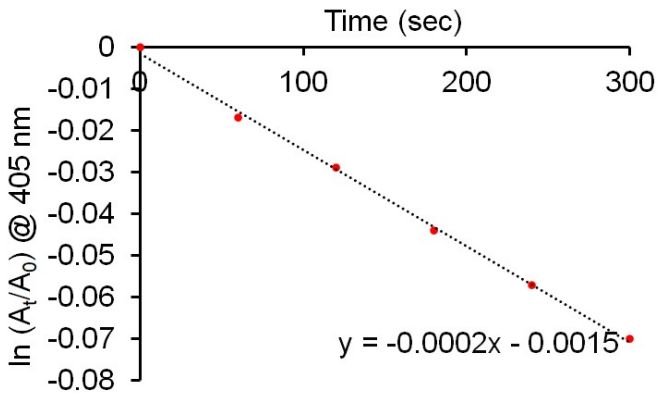

Figure 26. Thermal half-life of **2** in acetonitrile at 25 °C; $t_{1/2}$ = 57.75 min.

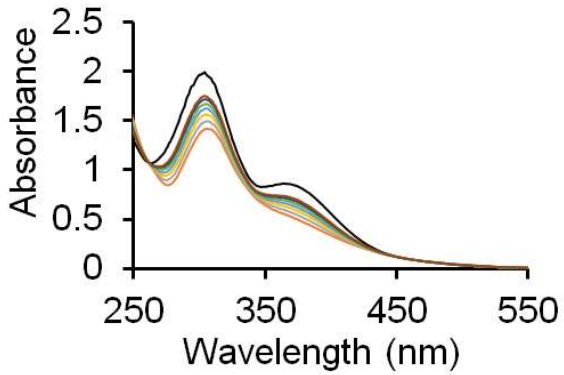

Figure 27. Thermal back isomerization of **2** in water at 25 °C before irradiation (BI, black lines) and absorbance at 405 nm irradiation (405_{PSS}, orange lines) and absorbance at 405 nm irradiation at time interval of 180 sec after keeping in dark (other lines).

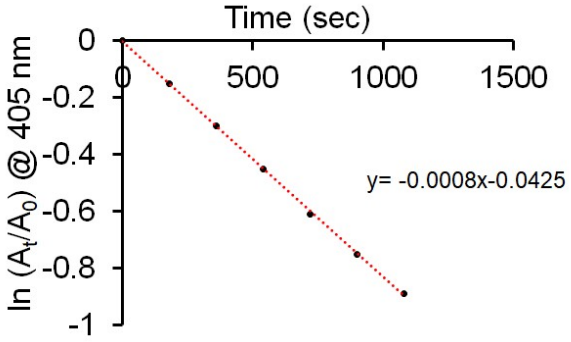

Figure 28. Thermal half-life of **2** in water at 25 °C $t_{1/2}$ = 14 min.

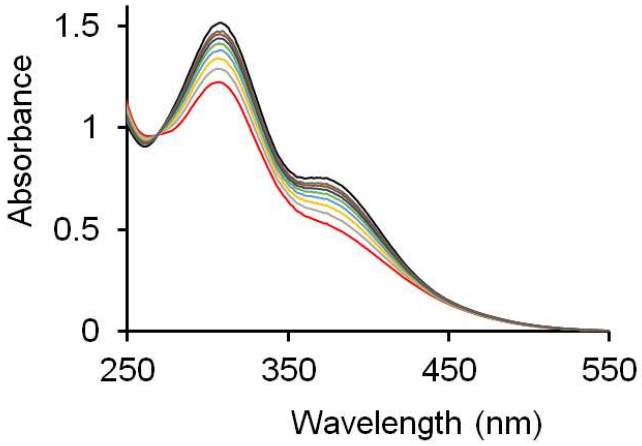

Figure 29. Thermal back isomerization of **2** in aqueous medium at 37°C before irradiation (BI, black lines) and absorbance at 405 nm irradiation (405_{PSS}, red lines) and absorbance at 405 nm irradiation at time interval of 60 sec after keeping in dark (other lines).

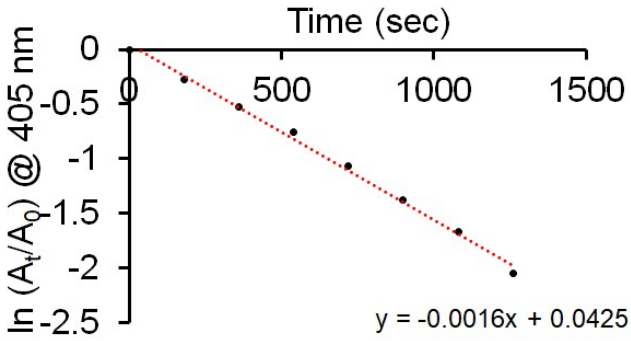

Figure 30. Thermal half-life of **2** in aqueous medium at 37 °C $t_{1/2}$ = 3 min.

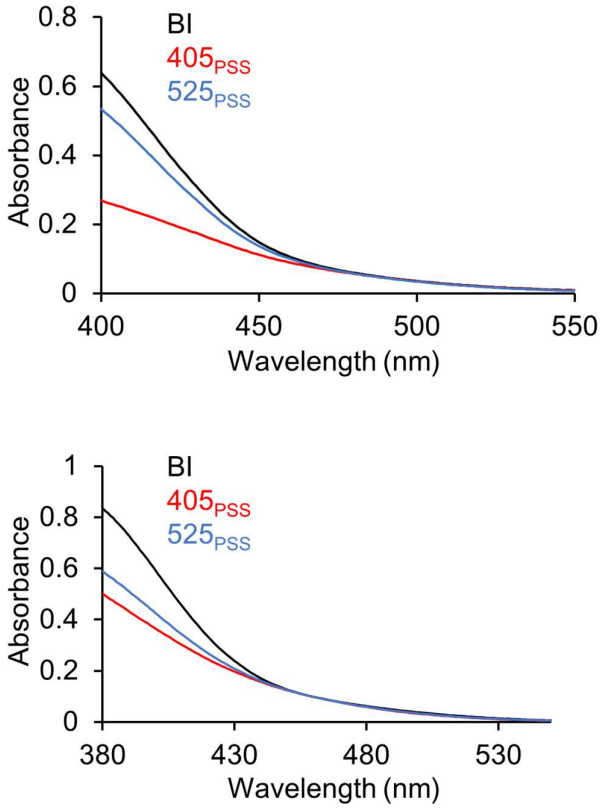

Figure 31. Zoom-in Absorption spectra of **1** and **2** in acetonitrile at 25 °C before irradiation (BI, black lines) and the PSS of 405 nm irradiation (405_{PSS}, red lines) and the PSS of 525 nm irradiation (525_{PSS}, blue lines).

Single crystal X-ray structure analysis.

Cryoloop was used to mount the single crystals. Crystallographic data was collected using a Rigaku XtaLab Synergy diffractometer with a single microfocus Mo Kα X-ray radiation source (PhotonJet-S), equipped with a Hybrid Pixel (HyPix) Array detector (HyPix-6000HE). Data collection, cell refinement, and data reduction were carried out with CrysalisPRO (Rigaku Oxford Diffraction, 2017).

The initial structure was solved by SHELXT [6] and expanded using Fourier techniques and refined on F2 by the full-matrix least-squares method SHELXL2018/3 [7] package compiled into OLEX2 package.[8] All parameters were refined using anisotropic temperature factors, except for hydrogen atoms, which were refined using the riding model, with a fixed C–H bond distance.

CCDC (Compound **1**) 2389890, CCDC (Compound **2**) 2389889 contain the supplementary crystallographic data for this paper.

X-ray crystal structure of BML-284

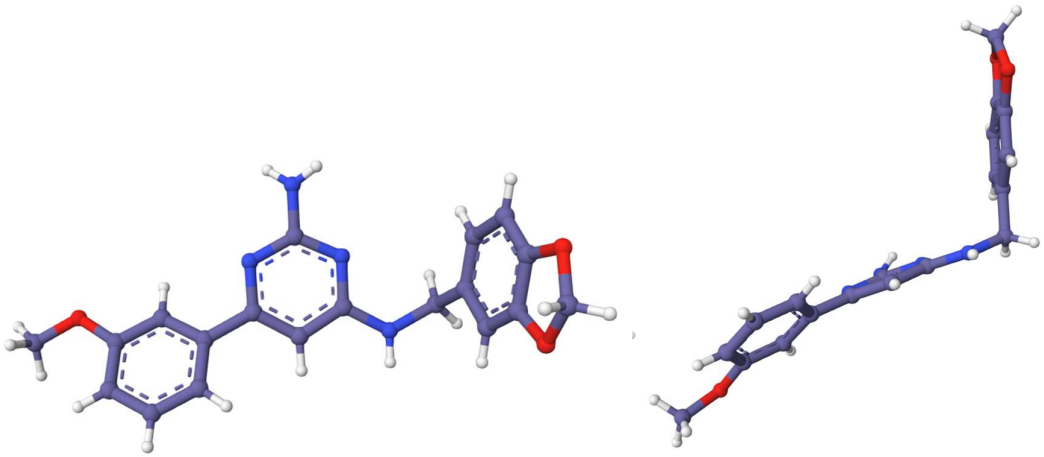

Figure 32. X-ray crystal structure of Wnt agonist BML-284 (two different view angle) taken from the protein data bank (PDB: 7CEK). 1,2 Methylenedioxybenzene motif was nearly perpendicular to the plane of aminopyrimidine motif.

Stability in presence of reductive environment

For biological applications, the photoswitch should be stable in reductive environment such as cell cytoplasm. Reductants like glutathione (GSH) can reduce the azo group (-N=N-) to the corresponding hydrazine (-NH-NH-) derivative which can misestimate the actual potency of each isomer. We tested the stability of **1** and **2** by incubating them separately in a mixture of

acetonitrile and glutathione (2mM) reductant (50/50 v/v). The absorbance spectra were then measured before and after light irradiation (405 nm, 2 h for **2** and 450 nm, 12 h for **1**). The absorbance originating from the azo chromophore remained unchanged, indicating the excellent stability of the *trans* and *cis* isomers of **1** and **2** toward glutathione reductant (Figure 33 and 34).

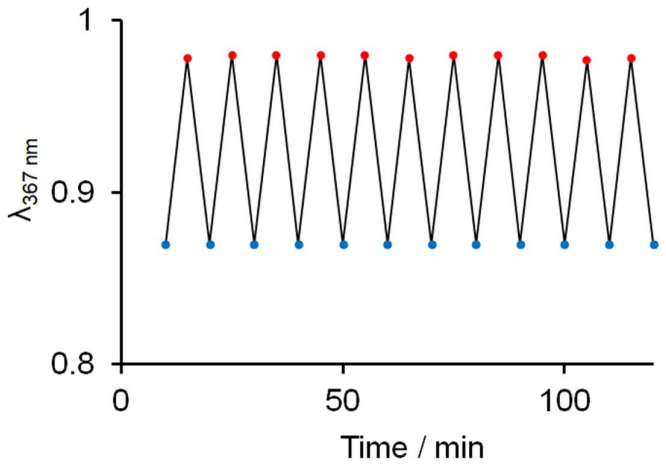

Figure 33. Absorbance changes of **2** at λ_{max} obtained by repeated irradiation with 405 nm (red dots) and 525 nm (blue dots) at the PSS in presence of 2 mM reduced glutathione. No degradation observed for compound 2 by 405 nm (0.05 mW/cm^2) irradiation.

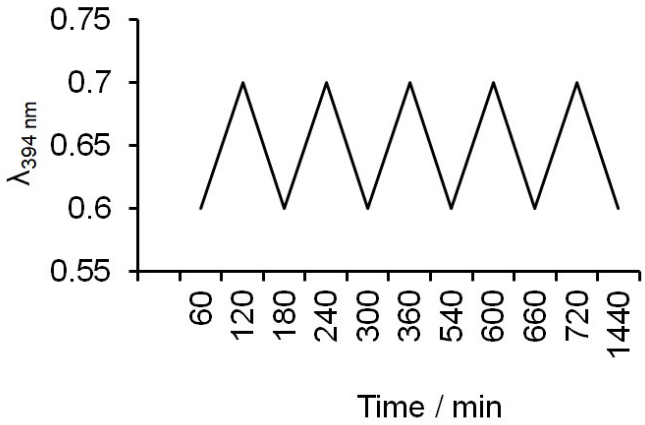

Figure 34. Absorbance changes of **1** at λ_{max} obtained by repeated irradiation with 450 nm and 525 nm at the PSS in presence of 2 mM reduced glutathione. No degradation observed for compound 1 by 450 nm (7.94 mW/cm^2) irradiation.

Photodegradation of Compound 1

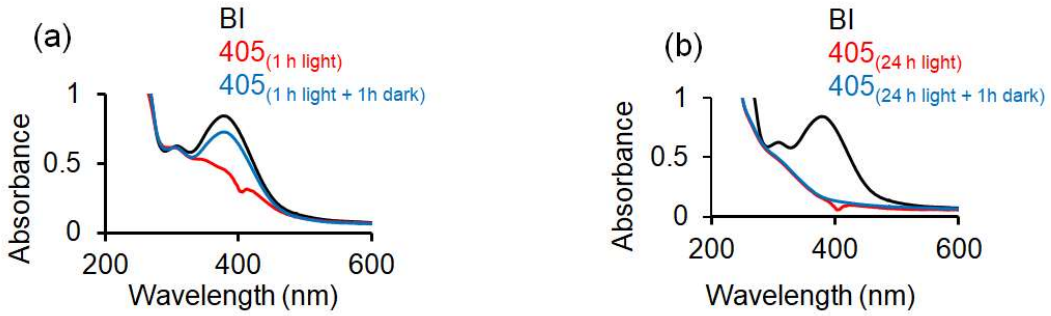

Figure 35. Absorbance spectra of compound **1** in acetonitrile at 25 °C measured before irradiation (BI, black), after specific hours of light irradiation (405 nm, 0.05 mW/cm^2, red), and after 1-hour dark recovery (blue) for 1 h, and 24 hours.

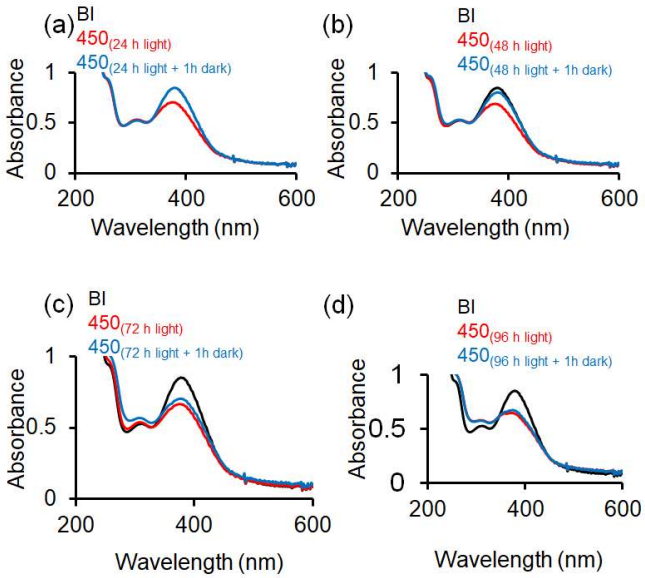

Figure 36. Absorption spectra of compound **1** in acetonitrile at 25°C measured before irradiation (BI, black), after specific hours of light irradiation (450 nm, 7.94 mW/cm^2, red), and after 1-hour dark recovery (blue) for 24, 48, 72, and 96 hours.

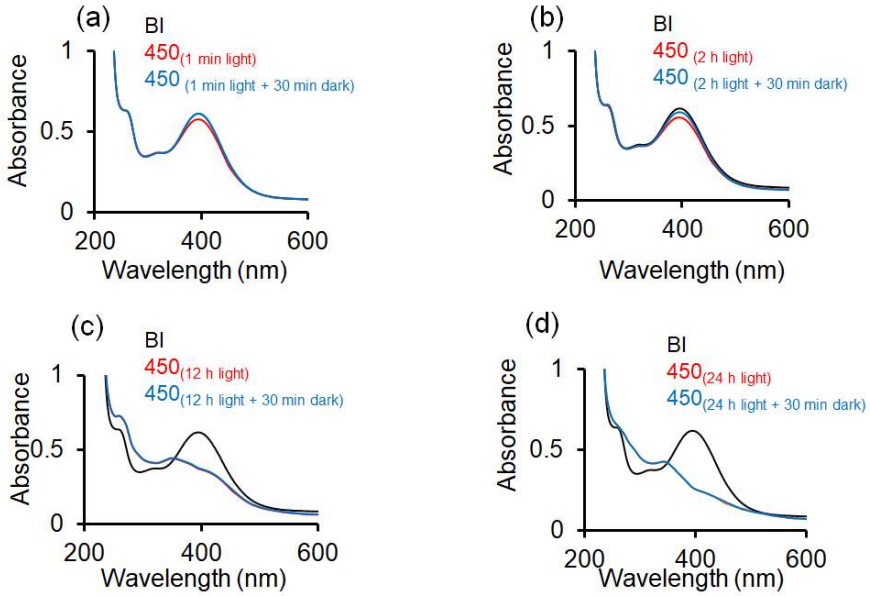

Figure 37. Absorption spectra of compound **1** in aqueous medium at 25°C measured before irradiation (BI, black), after specific hours of light irradiation (450 nm, 7.94 mW/cm^2, red), and after 30-min dark recovery for each (blue).

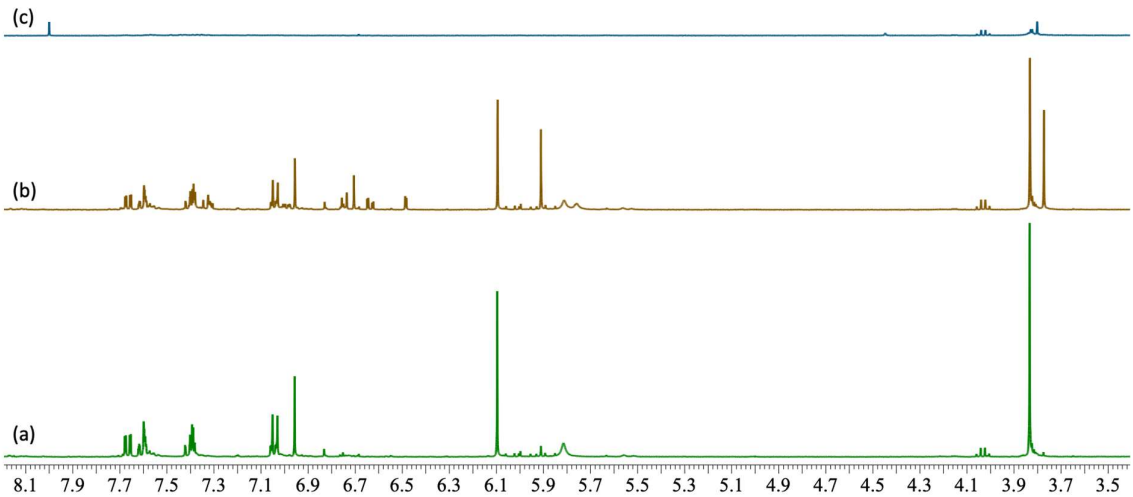

Figure 38. ^{1}H NMR in DMSO-d_6 of compound **1** (a) Before irradiation (b) after 405 nm (15.46 mW/cm^2; Asahi Spectra, CL-1503 LED light source) continuous irradiation for 1 h (c) after 405 nm continuous irradiation for 24 h. Characteristic peaks from the compound were disappeared after 24 h irradiation.

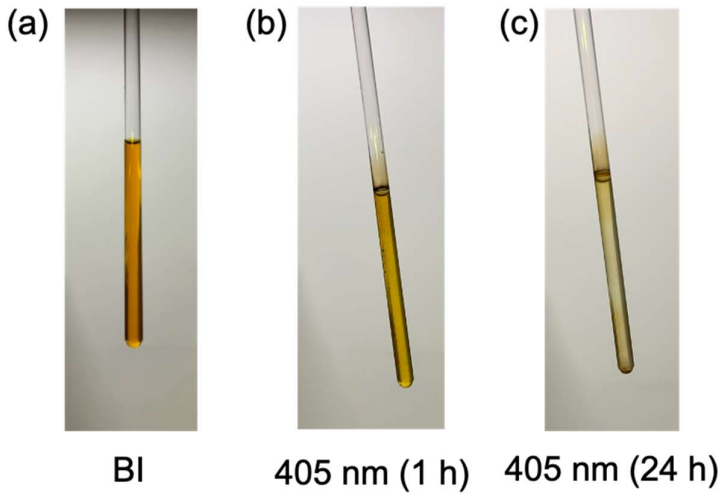

Figure 39. NMR tube images of compound **1** (a) Before irradiation (b) after 405 nm continuous irradiation maximum light intensity; Asahi Spectra, CL-1503 LED light source) for 1 h (c) after 405 nm continuous irradiation for 24 h. Images shows gradual precipitation of **1** (and disappearance of orange color) after 405 nm irradiation at 25 °C in DMSO-d_6.

Biological Studies

Wnt signaling pathway is directly connected to downstream gene expression, so I performed a luminescence-based cellular assay. For the luminescence based cellular assay, cells were pre-treated with a reporter gene, the luciferase gene (Luc gene). A reporter gene is a gene that is linked to the regulatory sequence of another gene of interest in cell cultures, bacteria, animals, or plants. These genes are called "reporters" because the traits they confer on the organisms expressing them can be easily identified and measured, or because they serve as selectable markers. Reporter genes are commonly used to indicate whether a specific gene has been taken up by or expressed in a population of cells or organisms. To introduce a reporter gene into an organism, both the reporter gene and the gene of interest are placed within the same DNA construct, which is then inserted into the cell or organism. It is crucial to select a reporter gene that is not naturally expressed in the cell or organism being studied,

as the expression of the reporter serves as a marker for the successful uptake of the gene of interest. Commonly used reporter genes that create visually identifiable traits often involve fluorescent and luminescent proteins. For example, the gene that encodes jellyfish green fluorescent protein (GFP) causes cells expressing it to glow green under blue or ultraviolet light. [16] Another example is the enzyme luciferase, which catalyzes a reaction with luciferin to produce light.[17]

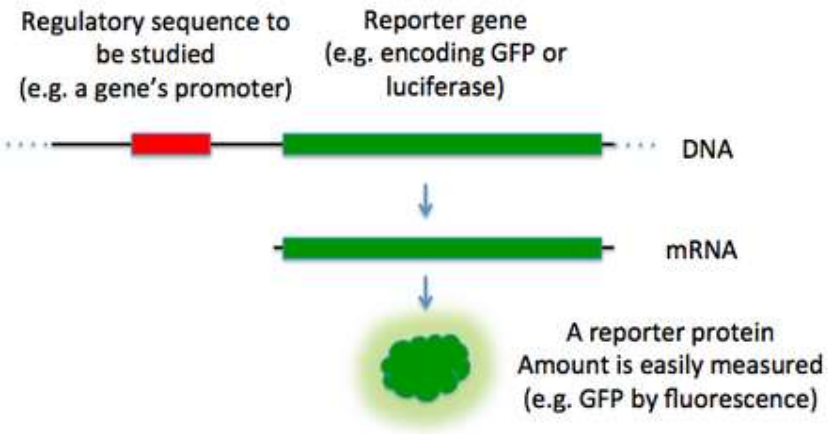

Figure 40. A diagram of how a reporter gene is used to study a regulatory sequence.

For biological studies, we selected HEK293t cells which are a type of human embryonic kidney cell line commonly used in research. They are recognized for their high transfection efficiency, which means they can easily incorporate foreign DNA. This characteristic makes them ideal for gene expression studies and for producing recombinant proteins. The HEK293t cells were cultured in a 24 well plate ($1x10^5$ cells/well). Next day the cells were transfected with a transfection reagent PEI Max (Polyethylenimine MAX) to add Luc gene into the cells. It is a widely used transfection reagent in biology for delivering genetic material into cells. After 24 hours, photoswitchable Wnt agonist **1** or **2** was added, one well plate was kept in dark while the other was kept under 405 nm light irradiation for 24 hours (0.05 mW/cm^2, 24 h at 37 °C and 5% CO_2). Then, the cells were observed under microscope and directly proceeded for the

luciferase assay. Luciferase and Renilla luciferase activity in cell lysates was measured by using the Dual-Glo luciferase assay system in the GloMax Explorer system (Promega). We normalized the relative luciferase activity expressed from the Wnt reporter plasmid to the activity of Renilla luciferase expressed from the pRL-TK plasmid.

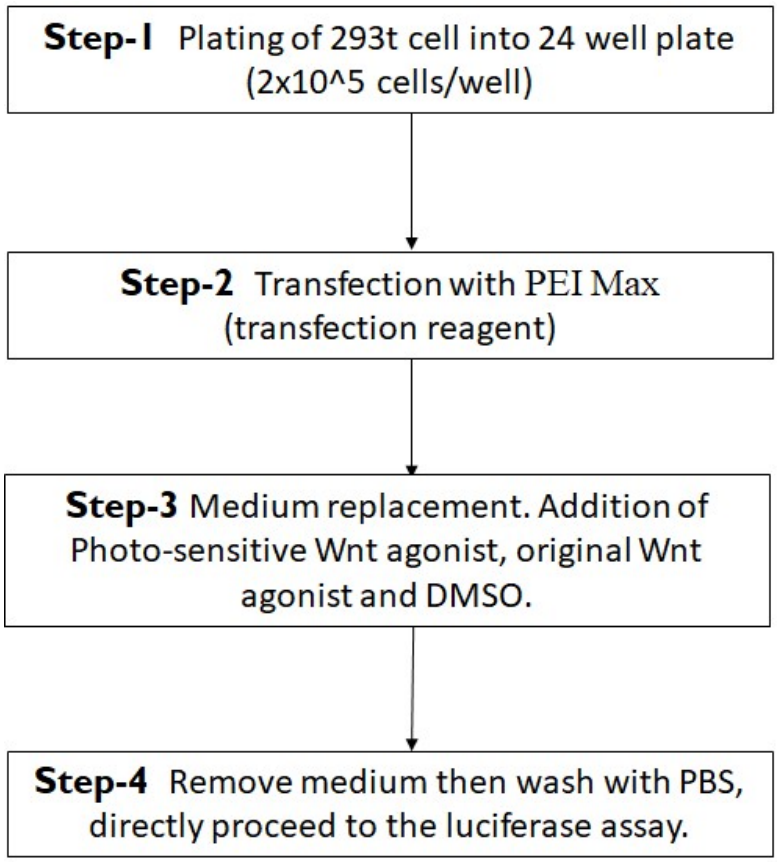

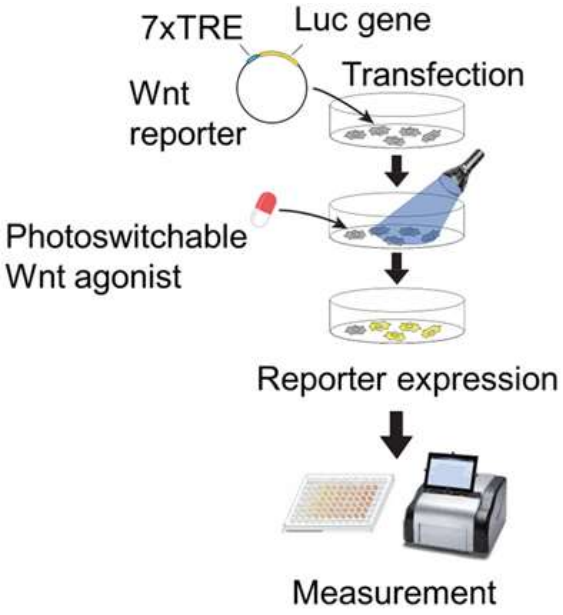

Figure 41. Schematic diagram showing a simplified workflow of luminescence-based cellular assay

Result and discussion

Time-dependent Wnt agonist activity check of BML-284

I optimized the incubation time required for Wnt agonist activity by BML-284 using 293T cells. Following the standard protocol mentioned in experimental section, we incubated 293T cells for 24 hours with 5 μM of BML-284 and the cell samples were collected at 4 hours, 8 hours, 12 hours and 24 hours followed by the measurement of luminescence. The maximum agonist activity was observed after 24 hours incubation as shown in the Figure S37. Accordingly, the cells were incubated for 24 hours after addition of photoswitchable agonists **1** and **2** in all our experiments.

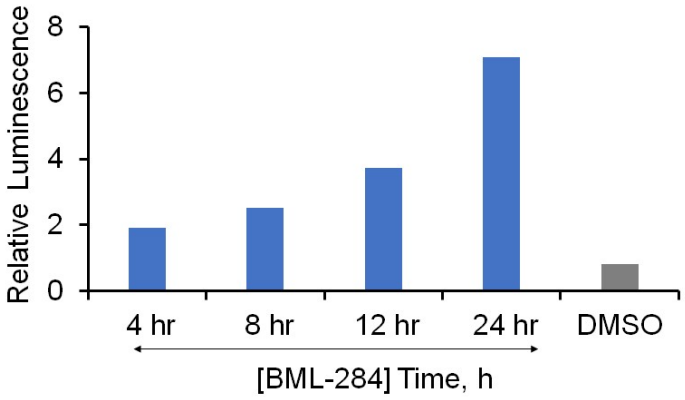

Figure 42. Bar graph representing relative luminescence measured at different time interval after treatment of 293T cells with BML-284 (5 μM) or DMSO.

Microscopy images of 293T cells

I noticed a shape change of 293T cells by microscopy imaging for the experimental sets containing BML284[18] and cis-rich state of **1** and **2** formed after light irradiation, and no shape change for DMSO control or trans-rich state of **1** and **2**. We assume that the observed cell shape change and activation of Wnt signaling pathway are related.

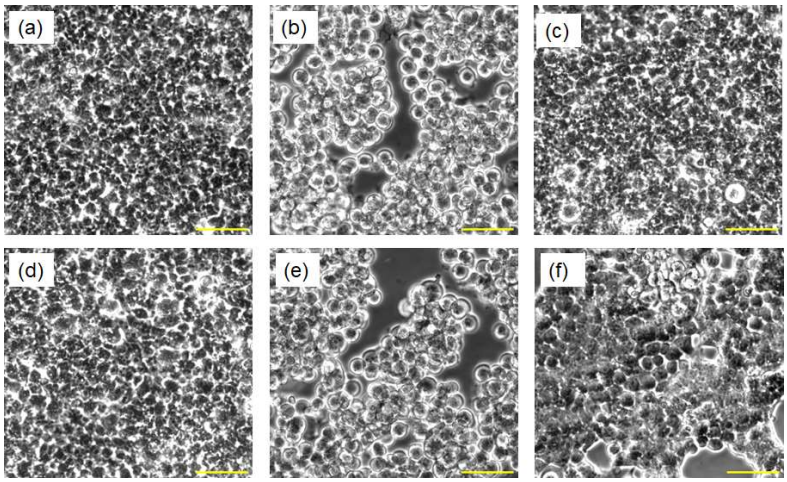

Figure 43. Microscopy images of 293T cells after 24 h-incubation of the cells in culture medium containing DMSO (0.4%) in dark (a), light (d) or BML-284 in dark (b), light (e) or **2** in dark (c) or light (f) (scale bar 200 μm). (405 nm, 0.05 mW/cm^2).

Microscopy images of 293T cells

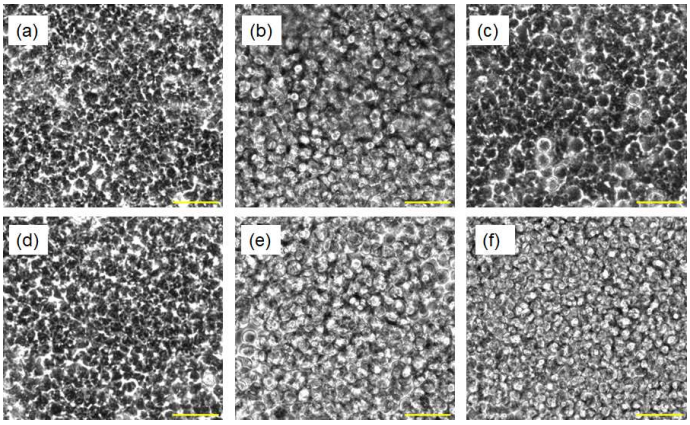

Figure 44. Microscopy images of 293T cells after 24 h-incubation of the cells in culture medium containing DMSO (0.4%) in dark (a), light (d) or BML-284 in dark (b), light (e) or **1** in dark (c) or light (f) (scale bar 200 μm). (450 nm light, 7.94 mW/cm^2).

Luminescence based cellular assay- Luciferase assay

The luciferase reporter assay is a test used to determine whether a protein can activate or repress the expression of a target gene.[19] In this assay, luciferase serves as a reporter protein. When the reporter protein is synthesized and a substrate is added, a chemical reaction occurs that produces bioluminescence, which is the emission of light. The intensity of this bioluminescence directly indicates the effect of the protein on the expression of the target gene.

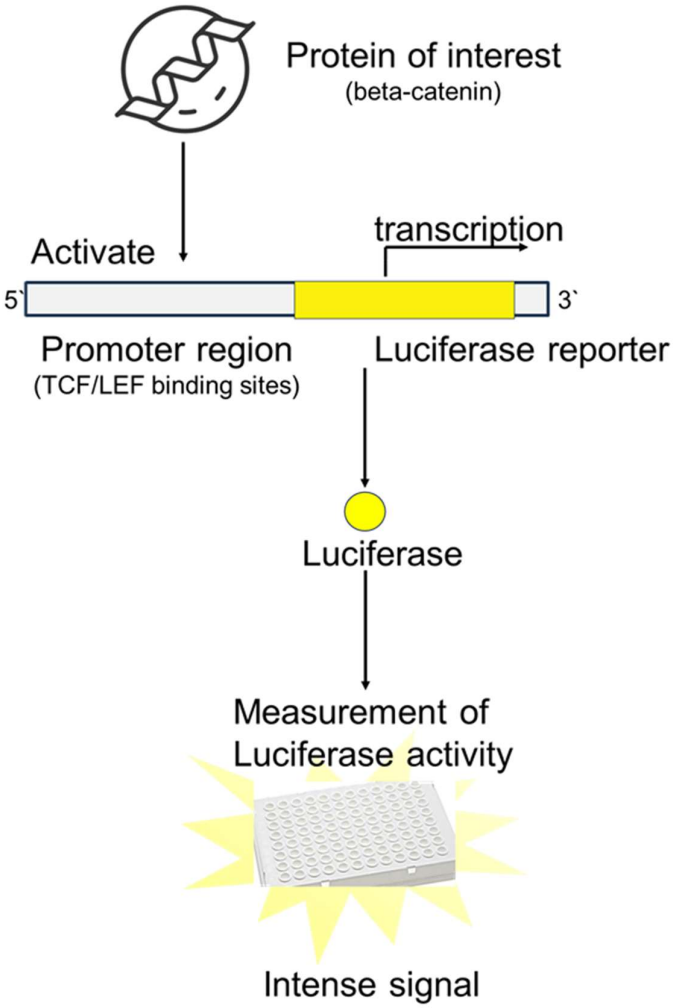

Figure 45. Luminescence based cellular assay- Luciferase assay

When a protein of interest activates transcription, a luminometer detects a bright bioluminescent signal. However, if the protein represses transcription, the luminometer detects no signal.

To conduct a luciferase reporter assay, we need a DNA plasmid that expresses the protein that we hypothesized may influence transcription. We also need to use a different DNA plasmid that contains the regulatory element (or a target promoter region) fused with the DNA coding sequence for a luciferase enzyme. When activated, this system will produce luciferase.

After the cells have been transfected with the luciferase reporter plasmid and allowed to grow for a few days, the next steps are to lyse the cells, add a substrate to the cell lysate, and measure the luciferase activity by assessing the amount of bioluminescent signal produced.

The Wnt signaling activation by agonist allows Luciferase gene expression, which can be measured as luminescence output using a commercial luciferin substrate (as shown in figure 46.). The experiment was conducted in a 24 well culture plate (293t cells) containing DMSO (negative control), **BML-284** (positive control) or photoswitchable agonists in dark or under 405 nm irradiation (0.05 mW/cm^2, 24 h at 37 °C and 5% CO_2). As expected, **BML-284** (5 μM) showed nearly similar relative luminescence both in dark and in the presence of light irradiation (Figure 47. light orange and orange bars). Interestingly, photoswitchable agonists showed a clear difference in relative luminescence in dark and light conditions in a dose-dependent manner (50–200 μM) (Figure 47. light blue and blue bars). These results indicated that the *cis*-rich state of **2** formed after light irradiation behaved as an agonist for the Wnt signaling, which was comparable to that of non-photoswitchable agonist **BML-284**. In contrast, the *trans*-rich state of **2** does not show agonist activity, which was nearly comparable with the DMSO control. The EC_{50} value calculated for **2** in the presence of light was 125 μM (Figure 43). Similar trend in the Wnt agonist activity by *cis*-rich state was also observed for **1** (Figure 49), however with a lesser efficiency than **2**, possibly due to the photodegradation of **1** under long time light exposure.

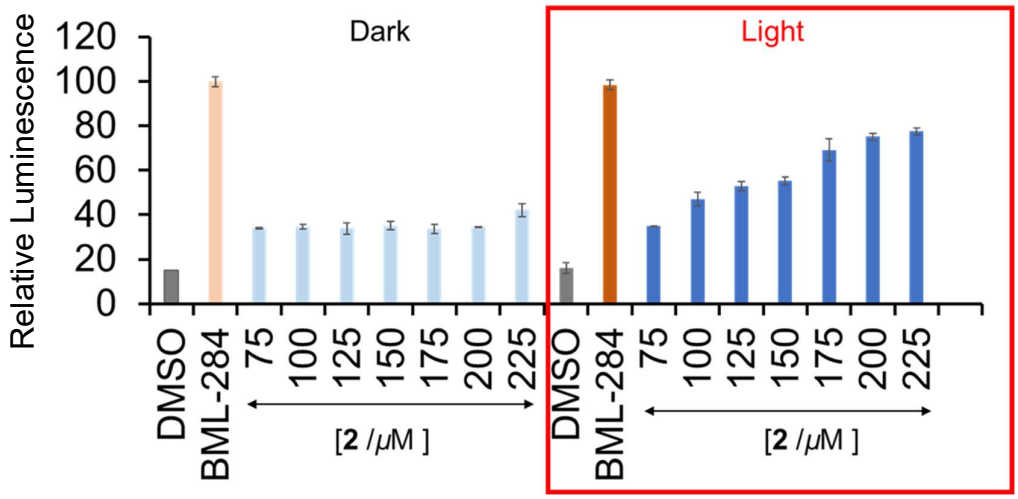

Figure 46. Bar graph of relative luminescence measured after treatment with DMSO, non-photoswitchable agonist BML-284 (5 μM) and photoswitchable agonist **2** in dark or light.

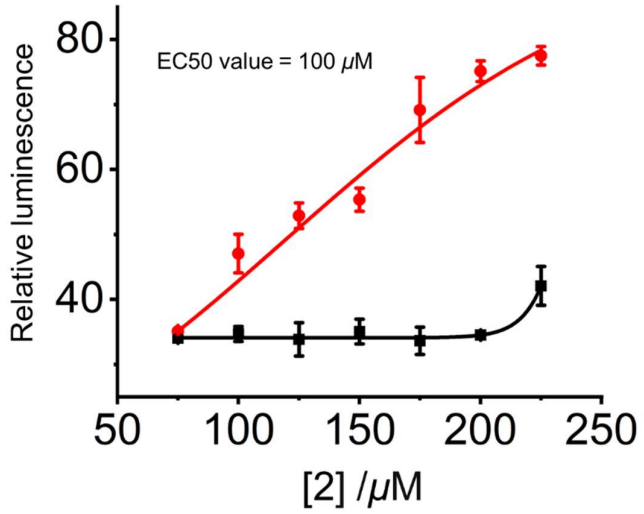

Figure 47. Non-linear fit curve of photoswitchable agonist **2** in dark (black curve) or light (red curve).

Bar graph of relative luminescence of Compound 1

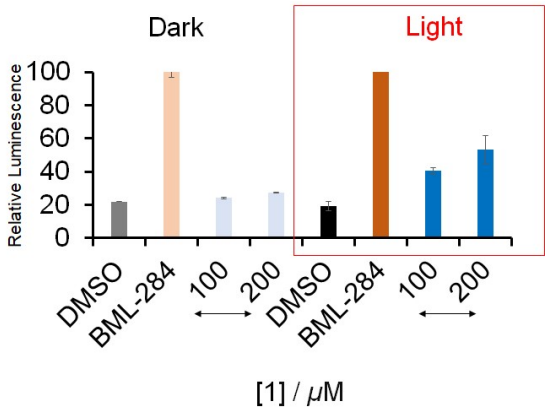

Figure 48. Bar graph of relative luminescence measured after treatment with DMSO (0.4%), non-photoswitchable agonist BML-284 (5 μM) and photoswitchable agonist **1** (100 μM and 200 μM) in dark or light (450 nm, 7.94 mW/cm^2).

Spatio regulation

In signal transduction, the location and duration of protein phosphorylation play a crucial role in effective signaling. Different cellular compartments contain unique proteins, which lead to distinct responses. For instance, phosphorylation at the membrane activates different pathways than phosphorylation in the nucleus. Prolonged phosphorylation results in sustained signaling, while transient phosphorylation leads to short-lived responses. Therefore, the spatiotemporal regulation of the Wnt signaling pathway is very important.

To demonstrate the effectiveness of our photoswitchable Wnt agonist in achieving localized agonist activity at a specific region of interest, we created two regions in a single well (6 well culture plate, well diameter 3.4 cm) treated with compound **2** and exposed one area to visible light irradiation (~0.05 mW/cm^2) from the bottom but not the other (covered with aluminium foil) (Figure 50). After 24 hours, cells were carefully scraped from the irradiated or non-irradiated regions of the well plate followed by the luminescence measurement. As expected, the cells treated solely with DMSO did not exhibit any changes in the relative luminescence at

405 nm light-exposed or covered area. However, cells treated with compound **2** exhibited about 3 times higher luminescence for light-exposed area than that of covered area. These results indicated that the agonist activity of the Wnt signaling pathway by *cis* **2** was selectively activated only at the light irradiated region with at least 10 mm spatial resolution (Figure 49).

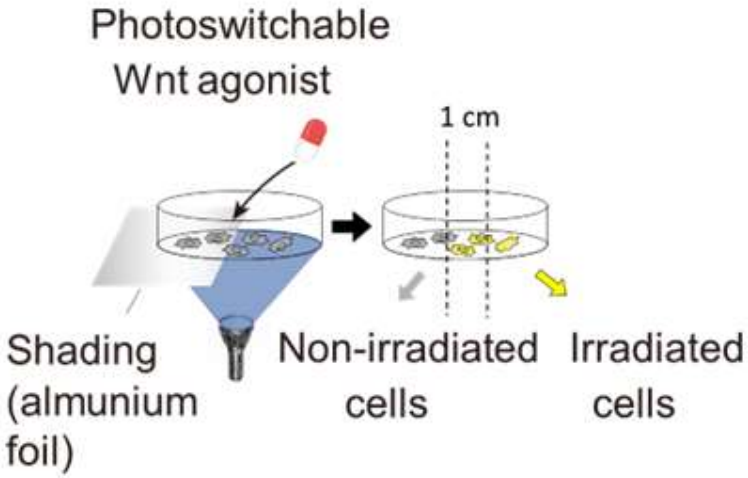

Figure 49. Schematic diagram showing a simplified workflow of selective activation of the Wnt signaling pathway. Irradiated and non-irradiated cells at 1.2 cm from the sides of well were scraped for luminescence measurement.

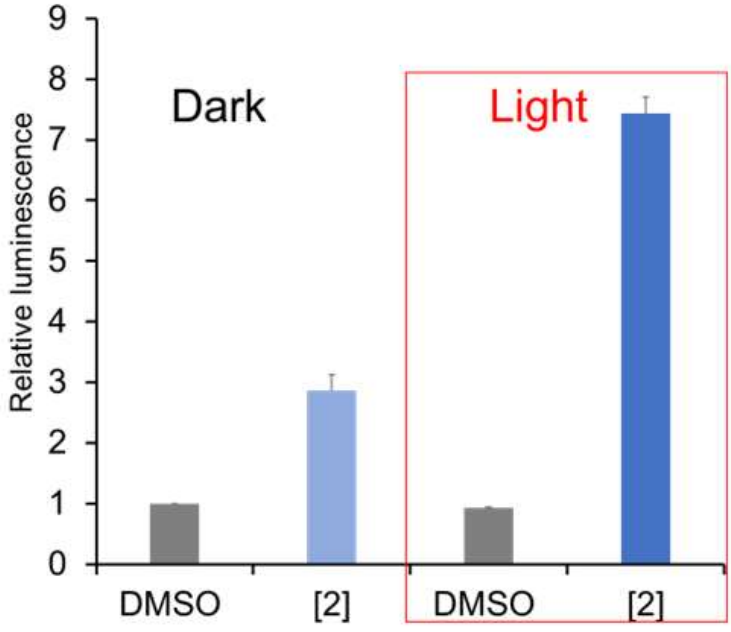

Figure 50. Bar graph of relative luminescence measured after treatment with DMSO and photoswitchable agonist **2** (50–200 μM) in dark or light (b).

Bar graph of relative luminescence of Compound 2 in dominant negative TCF4

The Wnt signal is transduced through its receptor and results in the formation of a heterodimeric complex of beta-catenin and TCF that drives downstream target gene expression. To determine if compound **2** induce reporter gene expression in a TCF-dependent manner, a dominant-negative TCF4 was constructed and transfected into cells. The dominant negative TCF4 contains a DNA-binding domain but lacks the beta-catenin-interaction motif, which leads to the sequestration of TCF-binding sites and subsequent blockage of beta-catenin and TCF-dependent transcriptional activity. As shown in the Figure 52 beta-catenin and TCF-dependent reporter gene expression induced by compound **2** was blocked in the presence of the dominant negative TCF4 in both dark and light conditions thus suggesting that compound **2** functions in the canonical Wnt signaling pathway through the TCFs.

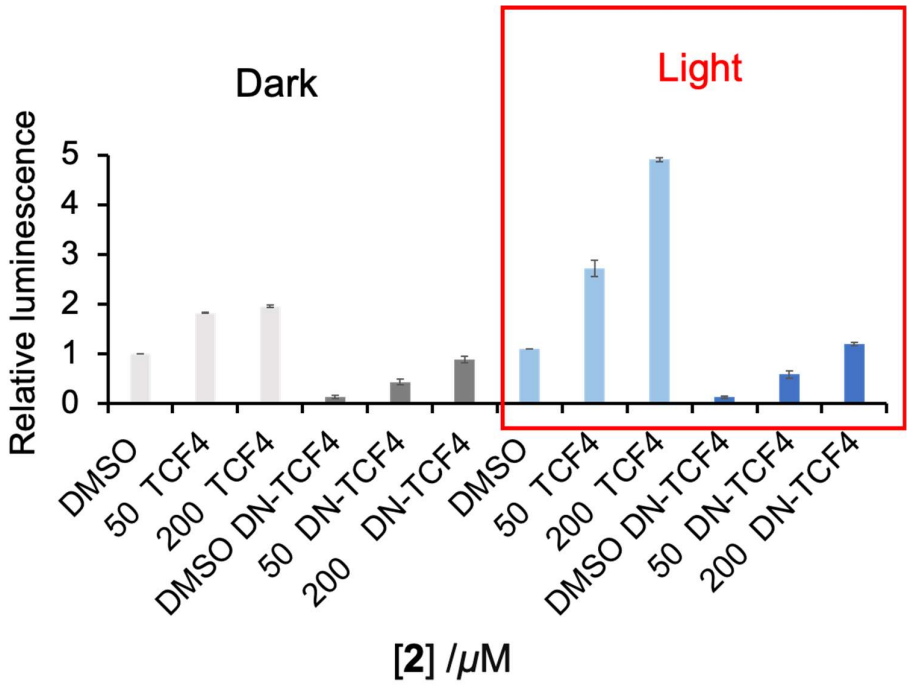

Figure 51. Bar graph of relative luminescence measured after treatment with DMSO (0.4%), photoswitchable agonist **2** (50 μM and 200 μM) in dark or light (405 nm, 0.05 mW/cm^2) in presence (DN-TCF4) and absence (TCF4) of negative TCF4 (n= 2 independent experimental sets).

Cell viability

To assess the cytotoxicity of compounds 1 and 2, I measured the percentage of dead and live 293T cells using Countess II FL (Thermo Fisher Scientific), according to the manufacturer's instructions. Briefly, 293T cells were detached using trypsin and suspended in DMEM containing 10 % FBS. The cell suspension was then mixed with 0.4% trypan blue solution in a 1:1 ratio to label dead cells. The numbers of stained dead cells and non-stained live cells were counted using Countess II FL. As control samples, we prepared 293T cells treated with 20% EtOH for one hour and untreated cells. EtOH treatment resulted in approximately 95% dead cells, while 99% of cells were living in the untreated sample, indicating the successful detection of live and dead cells.

(a)

Entry	Condition	Cell concentration	Cell viability
Cell only	Dark	1.84 x 10^6 / mL	**99%**
Cell + 20% EtOH	Dark	1.58 x 10^6 / mL	**5%**

(b)

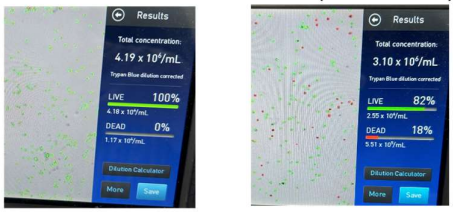

Entry	Condition	Cell concentration	Cell viability
Cell only	Dark	4.19 x 10^6 / mL	**100%**
Cell only	Light (405 nm, 0.38 mW/cm²)	1.58 x 10^6 / mL	**82%**

Figure 52. Cell viability percentage measured by cell counter machine (Countess II FL, ThermoFisher Scientific) in presence of 20% EtOH (a) and high intensity light (b). Images are directly visualized by cell counter and the table shows the cell concentration and viability.

(a)

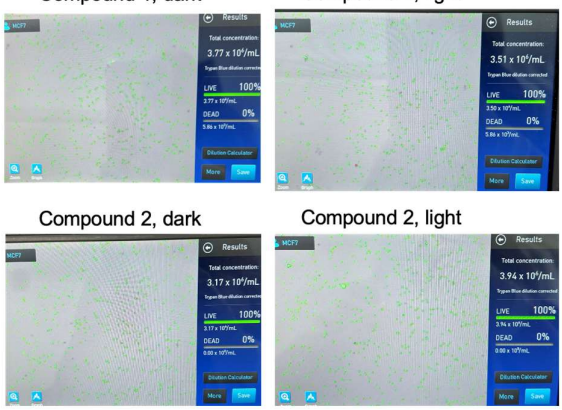

(b)

Compound	Condition	Cell concentration	Cell viability
1	Dark	3.77 x 10^6 / mL	**100%**
1	Light (450 nm, 7.94 mW/cm^2)	3.51 x 10^6 / mL	**100%**
2	Dark	3.17 x 10^6 / mL	**100%**
2	Light (405 nm, 0.05 mW/cm^2)	3.94 x 10^6 / mL	**100%**

Figure 53. Cell viability percentage measured by cell counter machine (Countess II FL, ThermoFisher Scientific) in presence of compound **1** (200 μM) and **2** (200 μM) in dark or light. (a) Images directly visualized by cell counter and (b) the table showing the cell concentration and viability.

Conclusion

In summary, I developed novel photoswitchable agonists **1** and **2** that enable photocontrol of the Wnt signaling pathway. The photoswitchable agonists have *trans* and *cis* isomers, which can be interconverted by visible light irradiations. Due to shape similarity with a known agonist **BML-284**, we found that only *cis* isomer of the agonist activated the Wnt signaling pathway. We found relatively higher agonist activity of *cis*-**2** for Wnt signaling than that of *cis*-**1**, due to an unexpected photodegradation of **1**. I have also shown selective activation of the Wnt signaling pathway with a spatial resolution of 10 mm upon light irradiation of **2** in a model cell culture system. The visible light-dependent control of Wnt signaling by these agonists may pave the way for the selective targeting of Wnt-sensitive cancer cells and the spatiotemporal control of stem cell functions.

References

1. V. Malhotra, M. C. Perry, *Cancer Biol Ther*., 2003, **2**, S2-S4.
2. R. Paus, I. S. Haslam, A. A. Sharov, V. A. Botchkarev, *Lancet Oncol*., 2013,**14**, e50-e59.
3. S. T. Sonis, L. S. Elting, D. Keefe, D. E. Peterson, M. Schubert, M. Hauer-Jensen, B. N. Bekele, J. Raber-Durlacher, J. P. Donnelly, E. B. Rubenstein, Cancer., 2004, **100**, 1995-2025.
4. H. Ludwig, S. Van Belle, P. Barrett-Lee, G. Birgegård, C. Bokemeyer, P. Gascón, P Kosmidis, M. Krzakowski, J. Nortier, P. Olmi, M. Schneider, D. Schrijvers, *Eur J Cancer.,* 2004, **40**, 2293-306.
5. R. Langer, Nature., 1998, **392**, 5-10.
6. N. C. Nicolaides, P. M. Sass, L. Grasso, Expert Opin Drug Discov., 2010, **5**, 1123-40.
7. E. Raschi, V. Vasina, M. G. Ursino, G. Boriani, A. Martoni, F. De Ponti, Pharmacol Ther., 2010, **125**, 196-218.
8. C. L. Sawyers, Nature., 2008, **452**, 548-52.
9. C. Brieke, F. Rohrbach, A. Gottschalk, G. Mayer, A. Heckel, Angew Chem Int Ed Engl., 2012, **51**, 8446-76.
10. G. Mayer, A. Heckel, Angew Chem Int Ed Engl., 2006, **45**, 4900-21.
11. A. A. Beharry, G. A. Woolley, Chem. Soc. Rev., 2011, **40**, 4422-37.
12. W. L. Jorgensen, Acc Chem Res., 2009, **42**, 724-33.
13. D. E. Brash, J. A. Rudolph, J. A. Simon, A. Lin, G. J. McKenna, H. P. Baden, A. J. Halperin, J. Pontén, Proc Natl Acad Sci U S A., 1991, **88**, 10124-8.
14. M. Protic-Sabljic, N. Tuteja, P. Munson, J. Hauser, K. Kraemer, K. Dixon, Mol. Cell. Biol., 1986, **6**, 3349−3356.
15. G. Banerjee, N. Gupta, A. Kapoor, Cancer Lett., 2005, **223**, 275-84.

16. P. Kamarajan, C. Chao, Biosci. Rep., 2000, **20**, 99−108.

17. K. Kalka, H. Merk, H. Mukhtar, J Am Acad Dermatol., 2000, **42**, 389-413.

18. H. R. López-Mirabal, J. R. Winther, Biochim Biophys Acta., 2008,**1783**, 629-40.

19. N. S. Kosower, E. M. Kosower, Int Rev Cytol., 1978, **54**,109-60.

20. K. Hüll, J. Morstein, D. Trauner, *Chem. Rev.*, 2018, **118**, 10710-10747.

21. J. Volarić, W. Szymanski, N. A. Simeth, B. L. Feringa, *Chem. Soc. Rev.*, 2021, **50**, 12377-12449.

22. P. Kobauri, F. J. Dekker, W. Szymanski and B. L. Feringa, *Angew. Chem. Int. Ed.*, 2023, **62**, e202300681.

23. M. Banghart, K. Borges, E. Isacoff, D. Trauner, R. H. Kramer, *Nat. Neurosci.*, 2004, **7**, 1381-1386.

24. J. Levitz, C. Pantoja, B. Gaub, H. Janovjak, A. Reiner, A. Hoagland, D. Schoppik, B. Kane, P. Stawski, A. F. Schier, D. Trauner, E. Y. Isacoff, *Nat. Neurosci.*, 2013, **16**, 507-516.

25. N. Perur, M. Yahara, T. Kamei and N. Tamaoki, *Chem. Commun.*, 2013, **49**, 9935-9937.

26. N. N. Mafy, K. Matsuo, S. Hiruma, R. Uehara and N. Tamaoki, *J. Am. Chem. Soc.*, 2020, **142**, 1763–1767.

27. K. Matsuo, S. Thayyil, M. Kawaguchi, H. Nakagawa and N. Tamaoki, *Chem. Commun.*, 2021, **57**, 12500–12503.

28. S. Sahu, K. Yoshizawa, T. Yamamoto, R. Uehara and N. Tamaoki, *J. Am. Chem. Soc.*, 2024, **146**, 21203–21207.

29. J. A. Frank, M. Moroni, R. Moshourab, M. Sumser, G. R. Lewin, D. Trauner, *Nat. Commun.*, 2015, **6**, 7118.

30. J. Qi, A. S. Amrutha, S. Ishida-Ishihara, H. M. Dokainish, P. K. Hashim, R. Miyazaki, M. Tsuda, S. Tanaka, N. Tamaoki, *J. Am. Chem. Soc.*, 2024, **146**, 18002-18010.
31. R. Hayat, M. Manzoor and A. Hussain, *Cell Biol. Int.*, 2022, **46**, 863-877.
32. Z. Steinhart and S. Angers, *Development*, 2018, **145**, dev146589.
33. X. Xu, M. Zhang, F. Xu and S. Jiang, *Mol. Cancer*, 2020, **19**, 165.

Acknowledgment

First and foremost, I extend my deepest gratitude to Almighty God for granting me the strength, perseverance, and dedication needed to successfully complete this research work. This dissertation has been made possible, first and foremost, through the invaluable guidance, unwavering support, and insightful ideas of my supervisors, Dr. Nobuyuki Tamaoki, Dr. Kuniharu Ijiro and co-supervisor, Dr. P. K. Hashim. Their continuous encouragement and exceptional mentorship not only enriched my academic journey but also provided me with an environment conducive to profound learning and intellectual growth. I am deeply grateful for the invaluable opportunities they have given me—opportunities that have shaped my research skills, broadened my scientific perspectives, and instilled in me a deep appreciation for rigorous inquiry. Their unwavering belief in my abilities fostered confidence and perseverance, allowing me to navigate challenges with determination. Beyond the academic realm, their guidance has left an enduring impact on my professional development, making this research experience one of the most memorable and transformative periods of my life. For their extraordinary support, patience, and dedication, I extend my deepest and most sincere gratitude. I would also like to express my heartfelt gratitude to Dr. Masamichi Imajo for his invaluable guidance and patience in teaching me cell culture techniques. His deep expertise, meticulous approach, and unwavering support have significantly shaped my understanding of this fundamental methodology. I am grateful to our lab member Dr. Saugata Sahu his help in the DFT calculations and insightful scientific discussions.

In my daily work, I have been truly fortunate to be surrounded by a friendly, supportive, and cheerful group of colleagues. I am sincerely grateful to Dr. Amathinadu S. Amrutha, Dr. Nusaiba Madappuram Cheruthu, and all my fellow lab members for their invaluable support and encouragement throughout my research journey. Their kindness, collaboration, and

willingness to share knowledge have made my work environment not only productive but also enjoyable.

I extend my heartfelt gratitude to the organizers of EXEX for their invaluable support in making my Ph.D. journey possible. Their dedication and efforts provided me with the opportunities and resources essential for achieving this milestone.

Lastly, I extend my deepest gratitude to my parents, Dr. Mohammad Ahmad and Atiya Ahmad, whose support and constant prayers have been the cornerstone of my journey. Their love, encouragement, and sacrifices have provided me with strength and resilience, shaping the path toward my aspirations. I am profoundly indebted to them for their guidance and belief in me.

Additionally, I am deeply grateful to my sisters, Sumbul, Ana, and Asra, as well as my dear friends Shanzah, Melda and Faizan, for their invaluable psychological support and encouragement throughout my career. Their presence and motivation have been a source of inspiration, uplifting me during challenges and celebrating my milestones.